The Astrophysical Journal Supplement Series, 259:53 (27pp), 2022 April https://doi.org/10.3847/1538-4365/ac50b7

The First Data Release of CNIa0.02—A Complete Nearby (Redshift <0.02) Sample of Type Ia Supernova Light Curves*

Ping Chen[1,2], Subo Dong[1], C. S. Kochanek[3,4], K. Z. Stanek[3,4], R. S. Post[5], M. D. Stritzinger[6], J. L. Prieto[7,8], Alexei V. Filippenko[9,10], Juna A. Kollmeier[11], N. Elias-Rosa[12,13], Boaz Katz[14], Lina Tomasella[15], S. Bose[3,4], Chris Ashall[16], S. Benetti[15], D. Bersier[17], Joseph Brimacombe[18], Thomas G. Brink[9], P. Brown[19], David A. H. Buckley[20], Enrico Cappellaro[15], Grant W. Christie[21], Morgan Fraser[22], Mariusz Gromadzki[23], Thomas W.-S. Holoien[24,39], Shaoming Hu[25], Erkki Kankare[26], Robert Koff[27], P. Lundqvist[28], S. Mattila[26], P. A. Milne[29], Nidia Morrell[30], J. A. Muñoz[31,32], Robert Mutel[33], Tim Natusch[34], Joel Nicolas[35], A. Pastorello[15], Simon Prentice[36], Tyler Roth[33], B. J. Shappee[16], Geoffrey Stone[37], Todd A. Thompson[3,4], Steven Villanueva[38,40], and WeiKang Zheng[9]

[1] Kavli Institute for Astronomy and Astrophysics, Peking University, Yi He Yuan Road 5, Hai Dian District, Beijing 100871, People's Republic of China dongsubo@pku.edu.cn
[2] Department of Astronomy, School of Physics, Peking University, Yi He Yuan Road 5, Hai Dian District, Beijing 100871, People's Republic of China
[3] Department of Astronomy, The Ohio State University, 140 West 18th Avenue, Columbus, OH 43210, USA
[4] Center for Cosmology and Astroparticle Physics, The Ohio State University, 191 West Woodruff Avenue, Columbus, OH 43210, USA
[5] Post Observatory, Lexington, MA 02421, USA
[6] Department of Physics and Astronomy, Aarhus University, Ny Munkegade 120, DK-8000 Aarhus C, Denmark
[7] Núcleo de Astronomía de la Facultad de Ingeniería y Ciencias, Universidad Diego Portales, Av. Ejército 441, Santiago, Chile
[8] Millennium Institute of Astrophysics, Santiago, Chile
[9] Department of Astronomy, University of California, Berkeley, CA 94720-3411, USA
[10] Miller Senior Fellow, Miller Institute for Basic Research in Science, University of California, Berkeley, CA 94720, USA
[11] Observatories of the Carnegie Institution for Science, 813 Santa Barbara Street, Pasadena, CA 91101, USA
[12] Institute of Space Sciences (ICE, CSIC), Campus UAB, Carrer de Can Magrans s/n, E-08193 Barcelona, Spain
[13] Institut d'Estudis Espacials de Catalunya (IEEC), c/Gran Capitá 2-4, Edif. Nexus 201, E-08034 Barcelona, Spain
[14] Department of Particle Physics and Astrophysics, Weizmann Institute of Science, Rehovot 76100, Israel
[15] INAF—Osservatorio Astronomico di Padova, Vicolo dell'Osservatorio 5, I-35122 Padova, Italy
[16] Institute for Astronomy, University of Hawaii at Manoa, 2680 Woodlawn Drive, Honolulu, HI 96822, USA
[17] Astrophysics Research Institute, Liverpool John Moores University, 146 Brownlow Hill, Liverpool L3 5RF, UK
[18] Coral Towers Observatory, Queensland, Australia
[19] George P. and Cynthia Woods Mitchell Institute for Fundamental Physics & Astronomy, TX, USA
[20] South African Astronomical Observatory, P.O. Box 9, Observatory 7935, Cape Town, South Africa
[21] Auckland Observatory, Auckland, New Zealand
[22] School of Physics, O'Brien Centre for Science North, University College Dublin, Belfield, Dublin 4, Ireland
[23] Astronomical Observatory, University of Warsaw, Al. Ujazdowskie 4, 00-478 Warszawa, Poland
[24] The Observatories of the Carnegie Institution for Science, 813 Santa Barbara Street, Pasadena, CA 91101, USA
[25] Shandong Provincial Key Laboratory of Optical Astronomy and Solar-Terrestrial Environment, Institute of Space Sciences, Shandong University, Weihai 264209, People's Republic of China
[26] Tuorla Observatory, Department of Physics and Astronomy, University of Turku, FI-20014 Turku, Finland
[27] Antelope Hills Observatory, 980 Antelope Drive West, Bennett, CO 80102, USA
[28] The Oskar Klein Centre, Department of Astronomy, Stockholm University, AlbaNova, SE-10691, Stockholm, Sweden
[29] Department of Astronomy/Steward Observatory, 933 North Cherry Avenue, Rm. N204, Tucson, AZ 85721-0065, USA
[30] Las Campanas Observatory, Carnegie Observatories, Casilla 601, La Serena, Chile
[31] Departamento de Astronomía y Astrofísica, Universidad de Valencia, E-46100 Burjassot, Valencia, Spain
[32] Observatorio Astronómico, Universidad de Valencia, E-46980 Paterna, Valencia, Spain
[33] Department of Physics and Astronomy, University of Iowa, Iowa City, IA 52242, USA
[34] Institute for Radio Astronomy and Space Research (IRASR), AUT University, Auckland, New Zealand
[35] Io Variablles-CCD group, 364 chemin de Notre Dame, F-06220 Vallauris, France
[36] School of Physics, Trinity College Dublin, The University of Dublin, Dublin 2, Ireland
[37] CBA Sierras, 44325 Alder Heights Road, Auberry, CA 93602, USA
[38] Massachusetts Institute of Technology, Cambridge, MA 02139 USA
Received 2021 June 29; revised 2021 December 24; accepted 2021 December 27; published 2022 March 30

Abstract

The CNIa0.02 project aims to collect a complete, nearby sample of Type Ia supernovae (SNe Ia) light curves, and the SNe are volume-limited with host-galaxy redshifts $z_{\rm host} < 0.02$. The main scientific goal is to infer the distributions of key properties (e.g., the luminosity function) of local SNe Ia in a complete and unbiased fashion in

* This paper includes data gathered with the 6.5 m Magellan Telescopes located at Las Campanas Observatory, Chile.
[39] NHFP Einstein Fellow.
[40] Pappalardo Fellow.

order to study SN explosion physics. We spectroscopically classify any SN candidate detected by the All-Sky Automated Survey for Supernovae (ASAS-SN) that reaches a peak brightness <16.5 mag. Since ASAS-SN scans the full sky and does not target specific galaxies, our target selection is effectively unbiased by host-galaxy properties. We perform multiband photometric observations starting from the time of discovery. In the first data release (DR1), we present the optical light curves obtained for 247 SNe from our project (including 148 SNe in the complete sample), and we derive parameters such as the peak fluxes, Δm_{15}, and s_{BV}.

Unified Astronomy Thesaurus concepts: Type Ia supernovae (1728)

Supporting material: figure set, machine-readable tables

1. Introduction

The explosion mechanism and progenitors of Type Ia supernovae (SNe Ia) are basic but open questions in astrophysics. There are several proposed channels, but no agreement as to which or even how many of the channels dominate (see, e.g., Maoz et al. 2014). SNe Ia span about an order of magnitude in peak luminosities and in the masses of synthesized ^{56}Ni that power the radiation. It is also debated whether this range in properties represents one continuous population or more than one overlapping but distinct populations. On the one hand, the main properties of SNe Ia appear to be continuous across the whole luminosity range. Phillips (1993) found that the peak luminosity of SNe Ia is tightly correlated with the light-curve shape characterized by the *B*-band post-peak decline rate $\Delta m_{15}(B)$, and this width-luminosity relation (WLR) is the foundation for using SNe Ia as cosmological distance indicators. Many properties of their light curves (see, e.g., Phillips 1993, 2012; Burns et al. 2014; Bulla et al. 2020) and spectra (see, e.g., Nugent et al. 1995; Branch et al. 2009) also appear to be continuous. On the other hand, the possible existence of more than one populations of SNe Ia has long been discussed (e.g., Branch & Miller 1993), including recent claims of bimodality in the luminosity function (via the proxy of $\Delta m_{15}(B)$; see, e.g., Ashall et al. 2016; Hakobyan et al. 2020), existence of two classes of fast-declining SNe Ia (Dhawan et al. 2017), and distinct near-ultraviolet (NUV)-optical (Milne et al. 2013) and early-time optical (Stritzinger et al. 2018) colors.

There have been tremendous efforts to obtain high-quality multiband light curves of large samples of nearby SNe Ia (e.g., Hamuy et al. 1996; Riess et al. 1999; Jha et al. 2006; Hicken et al. 2009; Contreras et al. 2010; Ganeshalingam et al. 2010; Stritzinger et al. 2011; Hicken et al. 2012; Krisciunas et al. 2017; Foley et al. 2018; Stahl et al. 2019). However, collecting a complete and unbiased nearby sample has only been made possible recently, thanks to the advent of wide-field time-domain surveys that do not target specific galaxies, such as the All-Sky Automated Survey for SuperNovae (ASAS-SN; Shappee et al. 2014; Kochanek et al. 2017), the Gaia transient survey (Hodgkin et al. 2021), the Palomar Transient Factory (Law et al. 2009) and its successor the Zwicky Transient Facility (ZTF; Kulkarni 2016; Perley et al. 2020), the Asteroid Terrestrial-impact Last Alert System (ATLAS; Tonry 2011; Tonry et al. 2018a), the Mobile Astronomical System of TElescope Robots (MASTER; Gorbovskoy et al. 2013), OGLE Transients Detection System (OTDS; Wyrzykowski et al. 2014), the Pan-STARRS Survey for Transients (PSST; Huber et al. 2015; Chambers et al. 2016), and the Catalina Real-Time Transient Survey (CRTS; Drake et al. 2009). Compared to other untargeted surveys, ASAS-SN is a dedicated survey with the main goal to search for bright, nearby SNe scanning the entire visible sky at approximately nightly cadence (a cadence of 2–3 nights down to ∼17 mag prior to the expansion in 2017 and a nightly cadence down to ∼18.5 mag after the expansion). The Gaia transient survey has a limiting magnitude down to 20.7 mag, and it is also an all-sky transient survey, but has a very uneven cadence across the sky, which can be up to months. Most other surveys do not have full-sky coverage, while many of them have access to a large fraction of the sky at a typical cadence on the order of days with deeper limiting magnitudes (given in the parentheses following the survey names) compared with ASAS-SN: ZTF (∼20.5 mag), Pan-STARRS (∼21.8 mag), MASTER (∼20 mag), ATLAS (∼20 mag), and CRTS(∼19.5 mag). For most untargeted surveys, there is no attempt to make spectroscopic classifications for all detected candidates selected according to certain criteria to form a complete sample. Furthermore, many time-domain surveys are primarily carried out in single bands, so without additional systematic follow-up efforts, it is not possible to obtain the color information that is critical to derive host-galaxy extinction and constrain SN physics.

We carry out the CNIa0.02 project to collect a complete, nearby, and effectively unbiased sample of Type Ia SNe at host-galaxy redshifts $z_{\rm host} < 0.02$ with well-observed multiband light curves. Our follow-up observations started in 2015 January and ended in 2020 January, and the SNe observed between 2015 September 17 and 2019 January 31 followed the selection criteria of the complete sample discussed below. The main goal for constructing a complete sample that is unbiased toward host-galaxy properties is to enable a reliable statistical inference on the distributions of photometric properties of SNe Ia (e.g., luminosity, color, light-curve shape, and derived physical parameters) in the local universe and also to study their dependence on host-galaxy properties.

To our knowledge, collecting and studying a complete sample in astronomy can be traced back to Schmidt (1968), who studied a complete sample of quasars defined with an observed flux density limit to derive their spatial distribution and luminosity function. Since then, complete samples have been widely applied in many areas of astronomy, and for instance, the LOSS survey produced one of the most influential complete samples of SNe from targeted searches (Leaman et al. 2011; Li et al. 2011a, 2011b). Such a complete sample is defined to include all objects that meet a certain set of well-defined selection criteria on observables, making it possible to derive quantitative completeness corrections to infer the statistical distribution of intrinsic properties such as the luminosity function. For the complete sample of CNIa0.02, we adopt the following observational selection criteria: (a) host-galaxy redshifts $z < 0.02$, (b) peak brightness $V_{\rm peak} < 16.5$ mag, and (c) detection by the ASAS-SN survey, that is, we not only include SNe discovered by ASAS-SN, but also SNe that were discovered first by others and were later detected by ASAS-SN. The ASAS-SN detections are nearly 100% complete for SNe with peak brightness <16.5 mag (see

Appendix C), and the ASAS-SN sample also has minimal bias in host-galaxy properties or SN locations inside the hosts (Holoien et al. 2017a, 2017b, 2017c, 2019). All of the SNe in DR1 have been spectroscopically classified by ASAS-SN or other groups. The complete sample includes all spectroscopic subclasses that are known to follow the WLR of the SNe Ia population. These include Ia-91bg and Ia-91T subtypes, but exclude SNe Iax and other peculiar SNe Ia-like objects that deviate from the WLR of SNe Ia (see Appendix D for a detailed discussion). The redshifts derived from SN classification spectra generally have too large uncertainties for our purpose, so we adopt host-galaxy spectroscopic redshifts for our complete sample selection. Where host-galaxy redshifts were unavailable in the NASA/IPAC Extragalactic Database[41] (NED), we have also measured the host-galaxy redshifts directly to determine whether the SNe Ia belong to the complete sample. We do not exclude SN candidates without apparent hosts from our selection (i.e., the "hostless" SN). In our project, ASASSN-18nt is the only hostless SN, which is an intracluster SN Ia located in the galaxy cluster Abell 0194 ($z = 0.018$), and its peak brightness (16.66 ± 0.02) does not meet our selection criterion for the complete sample. All of the SNe were followed photometrically, mainly in the optical bands (primarily *BVri*), but with near-infrared (IR) and Swift NUV observations of some objects as well. In this first data release (DR1) of CNIa0.02, we present optical light curves for 247 SNe Ia observed between 2015 and 2020. CNIa0.02 DR1 includes some SNe Ia that are not in the complete sample, and the complete sample has 148 SNe in total. We describe the overall project and the sample in Section 2, the data processing in Section 3, and the resulting light curves in Section 4. Our present results are summarized in Section 5.

2. Program Description and the Sample

We select our targets primarily based on ASAS-SN detections, and the complete sample was collected between 2015 September 17 and 2019 January 31. We have also observed a few SNe Ia before (since 2015 January) and after this period (until 2020 January), and they are included in DR1, but are not part of the complete sample. In the early phase of the complete sample collection, we attempted to observe all SNe Ia with $z < 0.034$ and a peak magnitude of $V_{\rm peak} < 17$. Between 2016 October and 2019 January, we restricted the complete sample to focus on SNe Ia with $z < 0.02$ and a peak magnitude of $V_{\rm peak} < 16.5$, as shown in Figure 4 and discussed in Appendix A. The detection efficiency of the ASAS-SN survey has been evolving mainly owing to upgrades in hardware, and since 2015, the detection efficiency has been almost 100% complete to <16.5 mag (see Appendix C for a detailed discussion of the sample completeness).

In Table 1 we give the general information (names given by the survey groups, IAU names, equatorial coordinates, discovery dates, host-galaxy names, and heliocentric host redshifts) for all objects in the CNIa0.02 DR1, which includes objects that have follow-up data (regardless of whether they belong to the complete sample) or have been considered for follow-up observations (regardless of whether such data are obtained). The host-galaxy redshifts are either from NED or are new measurements presented in Table 2. There are four SNe whose host-galaxy spectroscopic redshifts are not yet available, and for them, the redshifts determined from the SN spectra are given in Table 1 and are indicated with asterisks. Note that for all those four SNe, their peak magnitudes are fainter than 16.5, so they do not belong to the complete sample. We also provide additional information of *V*-band peak magnitudes (see Section 4.2 for how they are measured) and whether they were detected by ASAS-SN in Table 1. The complete sample includes 148 SNe. Figure 1 shows the cumulative distribution of host-galaxy redshifts of all SNe and those in the complete sample as blue and black histograms, respectively, and the latter roughly follows the expectation for a volume-limited complete sample (shown with the red line) when the peculiar velocity is negligible compared to the Hubble expansion velocity (at $z \gtrsim 0.01$). Note that our complete sample includes all SNe Ia selected by the observational criteria of $V_{\rm peak} < 16.5$ and $z < 0.02$. It does not include all SNe Ia at the dim end of the luminosity function ($\gtrsim -18.2$) near $z = 0.02$, therefore it is not expected to exactly follow the distribution of a volume-limited complete sample covering the full luminosity range.

CNIa0.02 DR1 includes *V*-band and *g*-band photometry from the 14 cm telescopes used to conduct the ASAS-SN survey. Immediately after the discovery of an SN candidate that met our magnitude criteria, we started multiband photometric observations, regardless of whether a spectroscopic classification was available then. For most objects, this data release contains follow-up photometry ending around 40–60 days after the optical peak. For objects with bright galaxy backgrounds that require image subtractions, we took template images at least 300 days after *B*-band peak, when the SN is typically more than $\gtrsim$7 mag below the peak. We have performed photometric follow-up observations using a number of telescopes ranging from ∼0.3 m to ∼2 m. In this data release, most data are in *BVri* bands observed by 1 m telescopes of the Las Cumbres Observatory Global Telescope network (LCOGT; Brown et al. 2013) distributed over four sites covering both hemispheres, two 0.6 m telescopes in Sierra Remote Observatories (CA, USA) and Mayhill (NM, USA) of the Post Observatory (PO), and the 1.3 m telescope of Small & Moderate Aperture Research Telescope System (SMARTS; Subasavage et al. 2010). For SNe found between 2016 October and 2018 March, we carried out a follow-up program using the Ultra-Violet/Optical Telescope (UVOT; Roming et al. 2005) on the Neil Gehrels Swift Observatory (Swift; Gehrels et al. 2004), and the UVOT *bv*-band data from that program are included in DR1. We also include some photometric data obtained from the 2 m Liverpool Telescope (LT), 0.5 m DEdicated MONitor of EXotransits and Transients (DEMONEXT; Villanueva et al. 2018), the 1 m telescope at WeiHai observatory of Shandong University (WHO; Hu et al. 2014), a 0.41 m telescope at A77 observatory, the Ohio State Multi-Object Spectrograph (OSMOS) on the 2.4 m Hiltner Telescope at the MDM observatory, the Wide Field reimaging CCD (WFCCD) camera and direct-imaging CCD camera SITe2K on the 2.5 m du Pont telescope, and Alhambra Faint Object Spectrograph and Camera (ALFOSC) on the 2.56 m Nordic Optical Telescope (NOT). The instrument specifications for the above facilities are described in Appendix B. We plan to make other follow-up data collected by our project available in the future.

3. Data Processing

This data release contains the results of processing over 20,000 images from ground-based observations and also Swift-UVOT images. For ground-based data, we developed the

[41] https://ned.ipac.caltech.edu

Table 1
General Properties of SNe Ia in CNIa0.02 DR1

Survey Name	IAU Name	R.A. (J2000)	Decl. (J2000)	Discovery Date	Host Galaxy	z_{host}[b]	V_{peak}[c]	ASAS-SN?[d]	Complete?[e]
ASASSN-15aj		10:52:53.261	−32:55:34.86	2015-01-08	NGC 3449	0.010921	14.77 ± 0.02	Y	N
ASASSN-15ak		00:12:01.546	+26:23:37.284	2015-01-09	UGC 00110	0.015034	14.70 ± 0.01	Y	N
ASASSN-15db		15:46:58.69	+17:53:02.22	2015-02-15	NGC 5996	0.010998	14.55 ± 0.03	Y	N
ASASSN-15eb		08:06:07.399	−22:33:48.852	2015-02-26	ESO 561-G 012	0.016481	15.82 ± 0.05	Y	N
J073615[a]	2015F	07:36:15.76	−69:30:23.0	2015-03-09	NGC2442	0.00489	13.31 ± 0.02	Y	N
J150530[a]	2015bp	15:05:30.09	+01:38:02.2	2015-03-16	NGC 5839	0.004069	13.90 ± 0.01	Y	N
ASASSN-15ga		12:59:27.293	+14:10:15.78	2015-03-30	NGC 4866	0.006631	15.08 ± 0.03	Y	N
ASASSN-15go		06:11:30.401	−16:29:04.596	2015-04-06	WISEA J061130.50-162908.3	0.018923	16.04 ± 0.09	Y	N
ASASSN-15hf		10:29:30.835	−35:15:34.812	2015-04-17	ESO 375-G 04	0.006178	14.27 ± 0.02	Y	N
ASASSN-15hx		13:43:16.69	−31:33:21.5	2015-04-26	uncataloged	0.00812	13.37 ± 0.01	Y	N
ASASSN-15jo		14:06:44.73	−34:27:18.0	2015-05-20	6dF J1406512-342931	0.015584	15.30 ± 0.02	Y	N
ASASSN-15kg		08:40:12.11	−04:35:29.0	2015-05-27	6dF J0840116-043537	0.014257	15.16 ± 0.05	Y	N
ASASSN-15kp		12:58:41.7	−32:07:28.7	2015-06-07	AM 1255-315	0.017402	15.48 ± 0.01	Y	N
ASASSN-15kx		22:16:11.810	+37:28:26.112	2015-06-10	MCG +06-49-001	0.018019	16.14 ± 0.06	Y	N
ASASSN-15lp		01:49:10.32	+05:38:23.316	2015-06-20	MRK 0576	0.017686	15.01 ± 0.14	Y	N
J114925[a]		11:49:25.48	−05:07:13.8	2015-06-29	NGC 3915	0.005573	13.26 ± 0.01	Y	N
ASASSN-15mc		02:48:59.570	+03:10:10.488	2015-07-05	UGC 02295	0.013916	15.10 ± 0.02	Y	N
J020622[a]	2015aw	02:06:22.53	−52:01:26.69	2015-07-12	ESO 197-G 024	0.01962	15.57 ± 0.04	Y	N
ASASSN-15ml		20:03:01.670	−21:54:48.24	2015-07-12	2MASX J20030163-2154516	0.018623	16.83 ± 0.17	Y	N
ASASSN-15od		02:23:13.210	−04:31:02.064	2015-08-10	MCG -01-07-004	0.017989	15.45 ± 0.03	Y	N
ASASSN-15oh		22:30:41.976	+39:17:35.232	2015-08-14	MCG +06-49-027	0.016835	16.15 ± 0.06	Y	N
ASASSN-15ol		01:54:06.041	−56:41:42.504	2015-08-15	NGC 0745 NED01	0.019777	15.77 ± 0.05	Y	N
ASASSN-15pl		02:30:23.24	−20:41:00.0	2015-09-11	ESO 545-G 025	0.016165	15.17 ± 0.04	Y	N
ASASSN-15pz		03:08:48.45	−35:13:51.0	2015-09-27	ESO 357-G 005	0.014903	14.25 ± 0.01	Y	N
ASASSN-15qc		00:39:17.94	+03:57:00.612	2015-10-01	UGC 00402	0.017649	15.56 ± 0.01	Y	Y
J015053[a]	2015ao	1:50:53.56	−36:00:30.8	2015-10-06	ESO 354-G 003	0.019133	16.90 ± 0.02	Y	N
J103747[a]	2015dc	10:37:47.94	−27:05:07.2	2015-10-20	IC 2597	0.007562	15.30 ± 0.24	N	N
ASASSN-15rq		00:08:03.09	−36:33:51.7	2015-10-21	MRSS 349-038278	0.02307	15.47 ± 0.01	Y	N
ASASSN-15rw		2:15:58.45	+12:14:13.812	2015-10-24	WISEA J021558.50+121414.4	0.01884	15.54 ± 0.03	Y	Y
J213123[a]		21:31:23.75	+43:36:31.2	2015-11-07	WISEA J213123.03+433618.0	0.018413	16.80 ± 0.08	Y	N
ASASSN-15so		11:14:11.213	+48:19:07.572	2015-11-08	NGC 3583	0.007125	13.86 ± 0.02	Y	Y
J010720[a]	2015ar	01:07:20.31	+32:23:59.0	2015-11-11	NGC 0383	0.017442	15.26 ± 0.01	Y	Y
J215050[a]		21:50:50.94	−70:20:28.9	2015-11-27	NGC 7123	0.012335	15.14 ± 0.01	Y	Y
ASASSN-15ti		3:05:08.06	+37:53:59.82	2015-12-01	WISEA J030510.59+375359.9	0.01732	16.07 ± 0.02	Y	Y
J112345[a]	2015bd	11:23:45.88	−01:06:21.2	2015-12-07	NGC 3662	0.018606	15.19 ± 0.02	Y	Y
ASASSN-15uh		09:30:13.78	+69:07:02.5	2015-12-18	KUG 0925+693	0.01489	15.30 ± 0.03	Y	Y
ASASSN-15us		22:09:09.55	−47:08:00.8	2015-12-29	NGC 7213	0.005839	$\leqslant$ 14.00	Y	N
ASASSN-15ut		0:21:21.09	−48:38:30.336	2015-12-30	NGC 0088	0.011471	16.37 ± 0.04	Y	N
ASASSN-16aa	2016A	08:09:14.48	+00:16:51.2	2016-01-02	UGC 04251	0.017373	16.83 ± 0.04	Y	N
ASASSN-16ad	2016F	01:39:32.06	+33:49:36.0	2016-01-09	KUG 0136+335	0.016138	15.26 ± 0.03	Y	Y
ATLAS16aab	2016adp	03:21:42.43	+42:05:49.4	2016-01-21	2MASX J03214217+4205549	0.018466	17.03 ± 0.08	Y	N
	2016W	02:30:39.67	+42:14:09.2	2016-01-25	NGC 0946	0.019253	16.01 ± 0.03	Y	Y
ASASSN-16ax	2016ag	01:31:23.16	+60:19:15.2	2016-01-26	WISEA J013123.32+601912.5	0.01461	$\leqslant$ 15.96	Y	Y
	2016adi	13:47:43.24	−30:55:55.57	2016-02-03	NGC 5292	0.014897	15.35 ± 0.05	Y	Y
ASASSN-16bn	2016adn	03:10:34.54	+04:16:10.8	2016-02-09	LEDA 3092121	0.023166	16.12 ± 0.05	Y	N
ASASSN-16ci	2016arc	03:19:21.27	+41:29:24.8	2016-02-26	NGC 1272	0.012725	$\leqslant$ 16.38	Y	Y
ASASSN-16cs	2016asf	06:50:36.72	+31:06:45.3	2016-03-06	KUG 0647+311	0.018019	15.72 ± 0.02	Y	Y
ASASSN-16cu	2016aue	18:35:56.53	−63:22:25.6	2016-03-06	IC 4723	0.011128	14.80 ± 0.13	Y	Y

Table 1
(Continued)

Survey Name	IAU Name	R.A. (J2000)	Decl. (J2000)	Discovery Date	Host Galaxy	z_{host}[b]	V_{peak}[c]	ASAS-SN?[d]	Complete?[e]
	2016bfu	05:51:15.52	−38:19:03.2	2016-03-23	IC 2150	0.010404	15.60 ± 0.01	Y	Y
ASASSN-16dn	2016blc	10:48:49.34	−20:15:50.3	2016-03-30	WISEA J104848.74-201547.4	0.01285	14.74 ± 0.01	Y	Y
iPTF16abc	2016bln	13:34:45.49	+13:51:14.7	2016-04-11	NGC 5221	0.023279	16.01 ± 0.04	Y	N
	2016brx	22:50:34.03	−01:32:32.5	2016-04-19	NGC 7391	0.010167	⩽ 16.80	Y	Y
	2016bry	20:43:22.40	+80:09:14.6	2016-04-19	UGC 11635	0.016024	15.77 ± 0.02	Y	Y
ASASSN-16eq	2016bsa	22:04:35.56	+42:19:32.6	2016-04-22	UGC 11898	0.01431	15.99 ± 0.06	Y	Y
Gaia16alq	2016dxv	18:12:29.36	+31:16:49.32	2016-04-26	uncataloged	0.02431	16.17 ± 0.03	Y	N
ASASSN-16es	2016cbx	11:50:54.53	+02:18:21.5	2016-04-27	WISEA J115054.33+021827.0	0.0285	16.54 ± 0.03	Y	N
iPTF16auf	2016ccz	14:31:09.26	+27:14:09.8	2016-05-13	MRK 0685	0.01489	15.43 ± 0.02	Y	Y
ASASSN-16fd	2016cdb	22:21:29.39	−22:15:46.6	2016-05-15	2dFGRS S006Z125	0.023906	…	Y	N
ASASSN-16fj	2016cmn	18:30:02.41	+39:57:55.8	2016-05-20	IC 1289	0.018313	16.02 ± 0.05	Y	Y
KAIT-16X	2016coj	12:08:06.80	+65:10:38.2	2016-05-28	NGC 4125	0.004483	13.01 ± 0.01	Y	Y
ASASSN-16fv	2016cqz	18:28:10.44	−71:41:38.8	2016-06-06	IC 4705	0.011972	14.91 ± 0.03	Y	Y
ATLAS16bdg	2016cvn	12:49:41.36	−11:05:33.5	2016-06-21	NGC 4708	0.013896	16.38 ± 0.09	Y	Y
ASASSN-16gp	2016cyl	13:16:42.77	−55:17:59.9	2016-06-27	WKK 2066	0.01646	16.53 ± 0.16	Y	N
	2016dag	08:19:07.45	−78:41:54.00	2016-07-09	ESO 018-G 002	0.01928	…	N	N
ASASSN-16hh	2016daj	02:04:37.50	+21:35:08.45	2016-07-17	MCG +03-06-031	0.03026	16.52 ± 0.02	Y	N
ASASSN-16hp	2016eiy	13:34:38.64	−23:40:53.15	2016-07-26	ESO 509-IG 064	0.008663	14.23 ± 0.02	Y	Y
	2016ekg	22:00:03.67	−30:11:02.86	2016-07-27	ESO 466-G 032	0.0171	15.07 ± 0.01	Y	Y
ASASSN-16hw	2016ekt	21:53:27.88	−34:24:20.95	2016-07-29	WISEA J215327.93-342421.2	0.01431	14.71 ± 0.01	Y	Y
	2016eqa	03:20:31.42	+41:30:40.90	2016-08-05	WISEA J032030.90+413032.3	0.014957	…	N	N
ASASSN-16ip	2016euj	02:27:21.70	−23:55:45.30	2016-08-09	ESO 479-G 007	0.017008	15.36 ± 0.01	Y	Y
ATLAS16cpu	2016ffh	15:11:49.48	+46:15:03.22	2016-08-20	CGCG 249-011	0.018204	⩽ 16.16	Y	Y
ASASSN-16jc	2016fej	20:40:39.93	−54:18:38.77	2016-08-22	NGC 6942	0.010914	13.91 ± 0.01	Y	Y
ASASSN-16jf	2016fff	22:36:59.21	−25:13:55.08	2016-08-23	UGCA 430	0.011441	14.93 ± 0.01	Y	Y
	2016fnr	16:37:38.80	+72:22:24.60	2016-08-29	UGC 10502	0.014367	15.03 ± 0.04	Y	Y
ASASSN-16jq	2016fob	08:05:09.20	−22:35:59.39	2016-08-30	CGMW 2-2125	0.0187	16.10 ± 0.02	Y	Y
	2016gfk	01:14:06.47	−32:39:25.80	2016-09-11	IC 1657	0.011952	16.78 ± 0.02	Y	N
	2016gfr	18:19:35.57	+23:47:09.20	2016-09-12	WISEA J181935.67+234714.0	0.01671	15.28 ± 0.03	Y	Y
OGLE16dha	2016hsc	06:32:25.13	−71:34:05.05	2016-09-19	LEDA 179577	0.0145	15.06 ± 0.02	Y	Y
ATLAS16cxr	2016gou	18:08:06.50	+25:24:31.3	2016-09-22	WISEA J180806.45+252431.8	0.0155	15.84 ± 0.05	Y	Y
ASASSN-16kz	2016gsb	06:04:28.21	−20:20:24.60	2016-09-29	ESO 555-G 029	0.00965	14.42 ± 0.01	Y	Y
ASASSN-16la	2016gsn	02:29:17.48	+18:05:16.33	2016-09-29	WISEA J022917.19+180516.3	0.01505	15.09 ± 0.01	Y	Y
ASASSN-16lc	2016gtr	19:29:00.48	−51:58:15.57	2016-09-30	WISEA J192901.71-515812.6	0.02033	15.59 ± 0.01	Y	N
Gaia16bkz	2016gwl	09:23:28.02	−23:10:10.74	2016-10-02	NGC 2865	0.008763	14.23 ± 0.02	Y	Y
	2016gxp	00:14:34.58	+48:15:08.03	2016-10-05	NGC 0051	0.017849	14.85 ± 0.01	Y	N
ASASSN-16lx	2016hht	10:24:05.32	+16:44:28.25	2016-10-19	IC 0607	0.018596	15.59 ± 0.04	Y	Y
J033333[a]	2016iil	03:33:33.26	−62:33:14.70	2016-10-19	WISEA J033334.19-623303.4	0.0289	16.62 ± 0.05	Y	N
ASASSN-16mc	2016hmo	19:58:41.31	−52:21:22.45	2016-10-21	ESO 233-IG 014	0.018913	16.85 ± 0.03	Y	N
ATLAS16dod	2016hli	03:43:38.45	+46:09:32.77	2016-10-25	MCG +08-07-008	0.016752	16.78 ± 0.01	Y	N
ATLAS16dpc	2016hnk	02:13:16.63	−07:39:40.80	2016-10-27	KUG 0210-078	0.016011	17.55 ± 0.03	N	N
ATLAS16dqf	2016hpw	21:09:07.88	−18:06:14.21	2016-10-30	WISEA J210907.40-180607.8	0.02102	15.96 ± 0.01	Y	N
ATLAS16dtf	2016hvl	06:44:02.16	+12:23:47.84	2016-11-04	UGC 03524	0.013092	15.45 ± 0.02	Y	Y
ASASSN-16mv	2016huh	08:57:05.24	−20:02:05.81	2016-11-04	ESO 563-G 035	0.018556	16.82 ± 0.01	Y	N
J110533[a]		11:05:33.80	+19:41:18.70	2016-11-15	LEDA 1602017	0.031599	…	N	N
PS16fdp	2016igr	01:03:26.69	−04:52:39.43	2016-11-23	MCG -01-03-082	0.017732	15.30 ± 0.02	Y	Y
ASASSN-16no	2016ins	08:07:27.42	+25:07:44.94	2016-11-26	IC 0493	0.020708	16.58 ± 0.02	Y	N

Table 1
(Continued)

Survey Name	IAU Name	R.A. (J2000)	Decl. (J2000)	Discovery Date	Host Galaxy	z_{host}[b]	V_{peak}[c]	ASAS-SN?[d]	Complete?[e]
ATLAS16dyo	2016ipf	08:07:13.15	05:40:59.69	2016-11-28	CGCG 031-049	0.021*	16.70 ± 0.02	Y	N
Gaia16caa	2016itd	14:18:47.74	+24:56:27.02	2016-12-02	UGC 09165	0.017542	15.42 ± 0.08	Y	Y
ASASSN-16oq	2016ito	12:31:09.00	−35:55:49.76	2016-12-08	6dF J1231098-355547	0.01992	15.64 ± 0.02	Y	Y
Gaia16cbd	2016iuh	12:19:31.44	+49:49:04.26	2016-12-09	UGC 07367	0.013696	15.40 ± 0.04	Y	Y
ATLAS16eay	2016jae	09:42:34.51	+10:59:35.38	2016-12-22	uncataloged	0.021*	16.79 ± 0.01	Y	N
ASASSN-16pd	2016jab	07:05:26.33	−76:00:34.48	2016-12-23	uncataloged	0.0216	15.95 ± 0.01	Y	N
PS17hj	2017jd	23:34:36.47	−04:32:04.32	2017-01-09	IC 5334	0.007368	⋯	N	N
ATLAS17abh	2017ae	02:05:50.62	18:22:30.23	2017-01-10	uncataloged	0.0275	16.41 ± 0.05	Y	N
ATLAS17air	2017jl	00:57:31.90	+30:11:06.83	2017-01-16	WISEA J005731.53+301109.4	0.016331	14.94 ± 0.01	Y	Y
iPTF17lf	2017lf	03:12:33.60	+39:19:15.30	2017-01-22	NGC 1233	0.01464	⋯	N	N
ASASSN-17bu	2017yv	10:23:40.49	−35:49:31.21	2017-01-31	ESO 375-G 018	0.015584	15.59 ± 0.02	Y	Y
ATLAS17ayw	2017atv	03:23:59.47	+37:45:30.65	2017-02-14	UGC 02710	0.018479	16.59 ± 0.03	Y	N
ASASSN-17cm	2017aut	05:47:42.41	−79:12:51.44	2017-02-14	WISEA J054743.06-791252.1	0.017233	17.10 ± 0.05	Y	N
ASASSN-17co	2017awk	18:09:20.745	+18:17:54.15	2017-02-16	UGC 11128	0.018056	15.74 ± 0.01	Y	Y
ASASSN-17cs	2017azw	04:22:50.06	−82:04:11.02	2017-02-21	ESO 015-G 010	0.01616	14.98 ± 0.01	Y	Y
ASASSN-17cz	2017bkc	17:50:30.11	−01:48:07.52	2017-02-23	LEDA 166870	0.017382	16.62 ± 0.02	Y	N
ASASSN-17dj	2017cav	18:06:43.92	06:50:19.64	2017-03-06	uncataloged	0.02096	16.31 ± 0.01	Y	N
	2017bzc	23:16:14.69	−42:34:10.90	2017-03-07	NGC 7552	0.005365	12.29 ± 0.01	Y	Y
PS17bwe	2017cbr	11:58:46.78	+15:43:08.87	2017-03-08	CGCG 098-015	0.017271	15.75 ± 0.01	Y	Y
DLT17u	2017cbv	14:32:34.42	−44:08:02.74	2017-03-10	NGC 5643	0.00399	11.70 ± 0.01	Y	Y
kait-17I	2017cfd	08:40:49.10	+73:29:15.10	2017-03-16	IC 0511	0.012085	14.78 ± 0.01	Y	Y
ATLAS17dcl	2017cjt	03:42:50.76	−01:52:28.98	2017-03-20	GALEX 2692072904051396069	0.009376	⋯	N	N
ATLAS17dfo	2017ckq	10:44:25.39	−32:12:32.83	2017-03-23	ESO 437-G 056	0.009893	14.33 ± 0.01	Y	Y
ASASSN-17ea	2017cjr	12:42:50.77	−30:24:43.65	2017-03-24	ESO 442-G 015	0.01444	15.06 ± 0.01	Y	Y
ASASSN-17em	2017cts	17:03:11.76	+61:27:26.06	2017-04-02	CGCG 299-048 NED01	0.01976	15.72 ± 0.01	Y	Y
J141551[a]	2017kdz	14:15:51.21	−48:08:02.60	2017-04-09	NGC 5516	0.013753	16.49 ± 0.06	Y	Y
ASASSN-17er	2017cze	11:09:46.82	−13:22:50.66	2017-04-11	NGC 3546	0.01486	15.77 ± 0.02	Y	Y
DLT17ar	2017cyy	09:36:36.30	−63:56:54.68	2017-04-12	ESO 091-G 015	0.009777	14.74 ± 0.01	Y	Y
ASASSN-17ez	2017daf	14:34:52.70	+40:44:52.87	2017-04-15	UGC 09386	0.019001	15.79 ± 0.02	Y	Y
Gaia17bat	2017dei	20:49:48.85	−25:42:02.56	2017-04-17	ESO 529-G 005	0.019804	16.38 ± 0.02	Y	Y
ASASSN-17fk	2017dhr	05:46:47.27	−16:47:00.30	2017-04-20	NGC 2076	0.007145	16.20 ± 0.03	Y	Y
Gaia17bci	2017dit	15:27:58.92	+42:50:48.70	2017-04-24	WISEA J152759.46+425058.9	0.01859	15.85 ± 0.02	Y	Y
ASASSN-17fr	2017dps	13:36:40.04	−33:58:01.29	2017-05-01	IC 4296	0.012465	14.77 ± 0.01	Y	Y
DLT17aw	2017drh	17:32:26.05	+07:03:47.52	2017-05-03	NGC 6384	0.005554	15.71 ± 0.02	Y	Y
	2017dzs	23:32:28.90	+23:56:11.20	2017-05-11	UGC 12655	0.017269	15.33 ± 0.18	N	N
ATLAS17fll	2017eck	18:00:31.28	02:25:54.55	2017-05-11	uncataloged	0.0233	16.20 ± 0.01	Y	N
ATLAS17fgh	2017ebm	13:23:19.12	−19:37:17.47	2017-05-13	ESO 576-G 044	0.016732	17.42 ± 0.10	N	N
J122100[a]	2017edu	12:21:00.78	−53:31:49.76	2017-05-16	WKK 0919	0.02*	16.87 ± 0.18	Y	N
ASASSN-17gr	2017egb	16:08:39.41	+12:00:40.21	2017-05-24	CGCG 079-058	0.016151	15.68 ± 0.01	Y	Y
DLT17bk	2017ejb	12:48:36.01	−41:19:33.53	2017-05-28	NGC 4696	0.009867	15.37 ± 0.01	Y	Y
ASASSN-17hb	2017ejw	01:12:34.16	+00:17:29.41	2017-05-31	UGC 00757	0.019117	15.53 ± 0.01	Y	Y
ATLAS17glh	2017ekr	23:02:32.19	+32:35:13.18	2017-06-01	UGC 12323	0.019914	15.95 ± 0.02	Y	Y
PS17dfh	2017emq	10:00:18.57	+54:32:23.07	2017-06-03	UGC 05369	0.005247	14.13 ± 0.01	N	N
ASASSN-17hk	2017enx	10:10:52.36	−66:38:50.63	2017-06-06	ESO 092-G 014	0.006398	13.82 ± 0.02	Y	Y
ASASSN-17ho	2017erv	19:18:47.01	−84:41:49.77	2017-06-13	AM 1904-844	0.017035	15.69 ± 0.02	Y	Y
J150915[a]	2017erp	15:09:14.81	−11:20:03.20	2017-06-13	NGC 5861	0.006174	13.49 ± 0.01	Y	Y
	2017ezd	19:56:38.66	−38:36:27.80	2017-06-17	ESO 339-G 009	0.018076	15.73 ± 0.02	Y	Y
ASASSN-17hz	2017evn	11:47:23.27	+23:21:53.57	2017-06-20	SDSS J114723.29+232157.5	0.017159	15.34 ± 0.02	Y	Y

Table 1
(Continued)

Survey Name	IAU Name	R.A. (J2000)	Decl. (J2000)	Discovery Date	Host Galaxy	z_{host}[b]	V_{peak}[c]	ASAS-SN?[d]	Complete?[e]
ASASSN-17ie	2017exo	18:31:41.79	+16:39:05.40	2017-06-24	IRAS 18294+1636	0.016288	16.25 ± 0.01	Y	Y
ASASSN-17ip	2017fbj	08:58:20.56	−65:21:49.75	2017-06-29	ESO 090-G 011	0.018422	15.92 ± 0.03	Y	Y
ATLAS17iky	2017ffv	13:57:21.74	−34:46:24.46	2017-07-10	ESO 384-G 018	0.01401	15.23 ± 0.02	Y	Y
DLT17bx	2017fgc	01:20:14.44	+03:24:09.96	2017-07-11	NGC 0474	0.007722	13.57 ± 0.01	Y	Y
ASASSN-17kf	2017fvl	02:55:42.59	+75:09:13.72	2017-08-01	UGC 02358	0.014343	15.99 ± 0.04	Y	Y
Gaia17bzv	2017fzy	05:21:58.87	+03:29:05.71	2017-08-05	IC 0413	0.014453	15.89 ± 0.01	Y	Y
Gaia17car	2017gbb	05:53:04.81	−17:52:03.50	2017-08-09	IC 0438	0.010422	⩽ 16.37	Y	N
DLT17cd	2017fzw	06:21:34.77	−27:12:53.51	2017-08-09	NGC 2217	0.005400	13.78 ± 0.01	Y	Y
ATLAS17jiv	2017gah	22:02:42.43	−32:47:33.50	2017-08-10	NGC 7187	0.008906	14.56 ± 0.01	Y	Y
	2017ghu	05:36:31.68	+16:38:32.60	2017-08-26	UGC 03329	0.017522	16.99 ± 0.05	Y	N
PSP17A	2017gjn	02:43:48.41	+32:31:33.70	2017-08-29	NGC 1067	0.01512	15.05 ± 0.01	Y	Y
	2017glq	02:08:27.95	+06:23:16.60	2017-09-03	IC 0208	0.011755	14.25 ± 0.01	Y	Y
PSP17B	2017glx	19:43:40.29	+56:06:36.30	2017-09-03	NGC 6824	0.011294	14.51 ± 0.01	Y	Y
ASASSN-17lz	2017grw	15:57:29.70	+15:52:21.94	2017-09-11	NGC 6018	0.017405	15.46 ± 0.01	Y	Y
ATLAS17lcr	2017guu	04:23:22.34	25:24:40.78	2017-09-13	2MFGC 03562	0.021*	16.60 ± 0.03	Y	N
Gaia17cin	2017gxq	13:05:24.01	+56:19:27.05	2017-09-17	NGC 4964	0.008406	14.05 ± 0.04	Y	Y
ATLAS17lbl	2017gup	03:29:34.25	+10:58:23.20	2017-09-17	WISEA J032934.19+105825.5	0.02316	16.86 ± 0.07	Y	N
ASASSN-17mh	2017guh	05:03:13.14	−22:49:59.16	2017-09-18	ESO 486-G 019	0.015427	15.12 ± 0.02	Y	Y
ASASSN-17mz	2017haf	23:56:21.92	+32:27:24.14	2017-09-30	KUG 2353+321	0.0161	15.34 ± 0.01	Y	Y
ASASSN-17ng	2017hgz	21:48:20.08	−34:57:10.62	2017-10-10	NGC 7130	0.016151	15.13 ± 0.01	Y	Y
ATLAS17mgh	2017hjw	05:08:43.83	+70:28:32.52	2017-10-14	UGC 03245	0.016161	15.90 ± 0.01	Y	Y
ATLAS17mgt	2017hjy	02:36:02.56	43:28:19.51	2017-10-14	WISEA J023602.13+432817.6	0.0177	15.40 ± 0.01	Y	Y
PSP17E	2017hle	01:07:33.06	+32:24:30.00	2017-10-18	NGC 0383	0.017005	16.97 ± 0.02	Y	N
ATLAS17msi	2017hoq	05:19:20.29	−17:36:42.10	2017-10-21	WISEA J051920.10-173647.6	0.02341	15.93 ± 0.01	Y	N
	2017hou	04:09:02.16	−01:09:36.07	2017-10-24	UGC 02969	0.016738	17.46 ± 0.01	Y	N
	2017hpa	04:39:50.75	+07:03:54.90	2017-10-25	UGC 03122	0.015654	15.37 ± 0.01	Y	Y
ASASSN-17pg	2017igf	11:42:49.85	+77:22:12.94	2017-11-18	NGC 3901	0.005624	14.59 ± 0.01	Y	Y
ASASSN-17pk	2017iji	12:12:26.87	+29:08:57.28	2017-11-20	NGC 4174	0.013493	14.93 ± 0.02	Y	Y
ASASSN-17qg	2017isj	11:10:44.56	+04:50:51.11	2017-12-02	UGC 06216	0.01933	15.63 ± 0.01	Y	Y
ATLAS17nmh	2017isq	13:13:12.18	−19:31:15.08	2017-12-04	NGC 5018	0.009393	13.75 ± 0.03	Y	Y
Gaia17dhq	2017izu	13:58:26.26	−34:30:57.92	2017-12-14	IC 4352	0.016915	14.84 ± 0.05	Y	Y
ATLAS17nse	2017iyb	06:08:56.81	−27:47:45.10	2017-12-16	ESO 425-G 010	0.010108	14.77 ± 0.01	Y	Y
ASASSN-17qz	2017iyw	08:13:30.63	71:25:45.12	2017-12-18	VII Zw 218	0.0174	15.60 ± 0.01	Y	Y
Gaia18ali	2017jav	07:02:55.50	62:46:21.00	2017-12-19	CGCG 285-013	0.01517	15.80 ± 0.01	Y	Y
ASASSN-17ri	2017jdx	00:47:56.19	22:22:26.26	2017-12-20	IC 1586	0.019417	15.81 ± 0.01	Y	Y
Gaia17dkm	2017jfw	13:27:53.77	−29:37:06.74	2017-12-26	NGC 5153	0.014413	⋯	N	N
	2018bi	02:19:53.38	+29:02:02.30	2018-01-07	UGC 01792	0.016635	⋯	N	N
ASASSN-18an	2018gl	09:58:06.25	+10:21:33.84	2018-01-13	NGC 3070	0.017906	16.14 ± 0.00	Y	Y
	2018gv	08:05:34.58	−11:26:16.87	2018-01-15	NGC 2525	0.005274	12.89 ± 0.01	Y	Y
SNhunt343	2018kp	10:46:33.06	+13:44:31.00	2018-01-24	NGC 3367	0.010142	16.05 ± 0.01	Y	Y
	2018pv	11:52:55.75	+36:59:10.30	2018-02-03	NGC 3941	0.003102	12.65 ± 0.02	Y	Y
PS18hq	2018pc	09:28:55.17	49:14:17.30	2018-02-03	UGC 05049	0.009083	15.05 ± 0.01	Y	Y
ASASSN-18bt	2018oh	09:06:39.54	19:20:17.77	2018-02-04	UGC 04780	0.010981	14.31 ± 0.01	Y	Y
ASASSN-18da	2018vw	03:29:16.65	−23:58:43.11	2018-02-17	MRSS 481-014096	0.0220	15.42 ± 0.01	Y	N
DLT18h	2018xx	12:53:48.25	−39:41:49.09	2018-02-21	NGC 4767	0.00999	14.43 ± 0.02	Y	Y
DLT18i	2018yu	05:22:32.36	−11:29:13.87	2018-03-01	NGC 1888	0.008112	13.95 ± 0.01	Y	Y
ASASSN-18en	2018zz	14:03:39.06	−33:58:42.60	2018-03-03	NGC 5419	0.013763	14.95 ± 0.01	Y	Y

Table 1
(Continued)

Survey Name	IAU Name	R.A. (J2000)	Decl. (J2000)	Discovery Date	Host Galaxy	z_{host}[b]	V_{peak}[c]	ASAS-SN?[d]	Complete?[e]
ASASSN-18gt	2018apo	12:45:05.30	−44:00:23.10	2018-04-02	ESO 268-G 037	0.016254	15.27 ± 0.03	Y	Y
DLT18q	2018aoz	11:51:01.83	−28:44:38.63	2018-04-02	NGC 3923	0.005801	12.87 ± 0.01	Y	Y
ASASSN-18hb	2018aqi	10:48:25.44	−25:09:35.82	2018-04-06	NGC 3393	0.012509	15.53 ± 0.02	Y	Y
	2018ast	11:41:07.96	+24:49:10.60	2018-04-08	NGC 3812	0.012012	16.33 ± 0.06	Y	Y
ASASSN-18iu	2018aye	17:57:40.36	+50:02:19.72	2018-04-21	SDSS J175740.70+500154.1	0.0223	15.72 ± 0.01	Y	N
ATLAS18ofk	2018big	17:25:39.14	+59:26:48.29	2018-05-10	UGC 10858	0.01815	15.79 ± 0.01	Y	Y
ASASSN-18kd	2018brz	08:33:22.28	−76:37:39.86	2018-05-15	WISEA J083322.17-763736.1	0.0193	16.14 ± 0.07	Y	Y
	2018bta	16:57:58.75	−62:43:53.70	2018-05-17	ESO 101-G 020	0.019497	15.43 ± 0.02	Y	Y
ATLAS18qpu	2018cnj	22:05:37.34	44:50:15.74	2018-05-28	UGC 11906	0.017529	17.16 ± 0.05	Y	N
Gaia18blb	2018chl	12:03:32.39	−43:39:17.32	2018-05-30	ESO 267-G 011	0.015347	17.06 ± 0.09	Y	N
ATLAS18qtd	2018cqj	09:40:21.46	−06:59:19.76	2018-06-13	IC 0550	0.016455	16.16 ± 0.05	Y	Y
ZTF18abgmcmv	2018cqw	18:17:32.21	19:26:40.49	2018-06-18	CGCG 113-034	0.009843	14.40 ± 0.01	Y	Y
ASASSN-18nt	2018ctv	01:25:52.03	−01:22:01.65	2018-06-21	ABELL 0194	0.018	16.67 ± 0.02	Y	N
ATLAS18rng	2018cuh	14:34:18.28	−37:28:44.74	2018-06-22	ESO 385-G 045	0.01411	15.03 ± 0.01	Y	Y
ATLAS18rqk	2018cuw	18:46:14.38	35:58:07.27	2018-06-24	WISEA J184614.46+355820.2	0.02682	16.55 ± 0.06	Y	N
ASASSN-18od	2018dda	22:08:14.15	−25:03:41.58	2018-07-04	ESO 532-G 021	0.018229	15.22 ± 0.02	Y	Y
ZTF18abgmcmv	2018eay	18:16:13.08	55:35:27.20	2018-07-15	IC 1286	0.018523	16.67 ± 0.01	Y	N
ATLAS18skj	2018ebk	20:28:35.54	25:44:08.32	2018-07-16	MCG +04-48-002	0.0139	16.26 ± 0.01	Y	Y
ATLAS18swa	2018enc	15:19:28.63	−09:52:50.03	2018-08-02	uncataloged	0.02389	15.95 ± 0.02	Y	N
Gaia18bzh	2018eov	16:15:17.42	−61:07:53.54	2018-08-02	2MFGC 13057	0.016371	15.42 ± 0.02	Y	Y
Gaia18bzv	2018eqq	03:06:55.16	41:30:32.90	2018-08-03	UGC 02536	0.015984	15.30 ± 0.01	Y	Y
ZTF18abmxahs	2018feb	17:10:11.16	+21:38:56.53	2018-08-16	CGCG 139-041	0.014757	15.21 ± 0.00	Y	Y
ASASSN-18tb	2018fhw	04:18:06.174	−63:36:56.59	2018-08-21	LEDA 330802	0.0170	16.36 ± 0.01	Y	Y
PS18blk	2018fop	01:15:18.11	−06:51:32.54	2018-08-21	uncataloged	0.02121	15.54 ± 0.02	Y	N
ASASSN-18to	2018fpm	22:24:21.83	−33:41:32.87	2018-08-31	NGC 7267	0.011191	16.40 ± 0.05	Y	Y
ASASSN-18ti	2018fnq	20:12:30.00	−44:06:35.14	2018-08-31	WISEA J201229.79-440631.4	0.01906	15.68 ± 0.02	Y	Y
ASASSN-18ud	2018fuk	05:45:08.16	−79:23:47.52	2018-09-05	ESO 016-G 011	0.017582	15.71 ± 0.01	Y	Y
ASASSN-18vm	2018ghb	06:58:27.60	−28:45:49.18	2018-09-14	ESO 427-G 022	0.007595	14.44 ± 0.02	Y	Y
ZTF18acarupz	2018htw	22:08:49.702	+38:09:04.93	2018-10-09	uncataloged	0.0206	15.85 ± 0.04	Y	N
Gaia18czg	2018hib	02:56:21.27	−32:11:08.77	2018-10-10	ESO 417-G 006	0.016291	15.19 ± 0.01	Y	Y
ASASSN-18ya	2018hkq	10:05:47.84	−17:26:03.12	2018-10-15	IC 2541	0.016598	15.36 ± 0.06	Y	Y
ASASSN-18yf	2018hme	09:35:39.43	−17:23:10.90	2018-10-20	MCG -03-25-010	0.014123	15.52 ± 0.05	Y	Y
ZTF18acbvgqw	2018htt	03:06:02.90	−15:36:41.69	2018-10-31	NGC 1209	0.008673	13.96 ± 0.02	Y	Y
ZTF18acbujhw	2018hrt	02:38:27.85	+29:45:32.44	2018-10-31	UGC 02122	0.016945	17.28 ± 0.02	Y	N
ASASSN-18yq	2018hsa	21:15:01.03	−47:12:37.40	2018-11-01	NGC 7038	0.016471	15.60 ± 0.01	Y	Y
ATLAS18zek	2018ilu	23:33:20.98	04:48:34.66	2018-11-12	uncataloged	0.01807	15.35 ± 0.01	Y	Y
	2018imd	12:48:24.95	−05:47:39.20	2018-11-14	NGC 4697	0.00414	13.91 ± 0.05	Y	Y
	2018isq	03:16:50.60	+80:47:04.50	2018-11-20	NGC 1184	0.007599	15.94 ± 0.01	Y	Y
ZTF18acqqyah	2018iuu	11:27:21.22	+59:37:48.26	2018-11-21	UGC 06452	0.017051	15.39 ± 0.01	Y	Y
ZTF18acrdlrp	2018jaj	10:29:52.36	+20:40:09.71	2018-11-25	SDSS J102952.29+204009.3	0.019411	15.44 ± 0.01	Y	Y
ASASSN-18aai	2018jeo	09:04:36.840	−19:47:08.30	2018-11-28	ESO 564-G 014	0.018653	15.91 ± 0.01	Y	Y
Gaia18drb	2018jjd	04:24:20.050	−31:59:14.78	2018-12-03	MRSS 420-017372	0.0256	15.84 ± 0.02	Y	N
ASASSN-18aay	2018jky	03:26:01.930	−17:33:48.02	2018-12-05	NGC 1329	0.01458	15.33 ± 0.01	Y	Y
PS18bzo	2018jmo	06:51:20.470	45:38:41.10	2018-12-06	2MASX J06512361+4538445	0.0209	16.51 ± 0.02	Y	N
ATLAS18bbdt	2018jov	08:00:07.140	58:42:34.95	2018-12-08	SBS 0755+588	0.019213	16.06 ± 0.01	Y	Y
ASASSN-18abr	2018jwi	06:18:39.283	−54:28:14.84	2018-12-14	WISEA J061839.31-542813.9	0.015457	15.02 ± 0.01	Y	Y
ZTF18aczeesl	2018kmu	14:41:32.924	+48:12:14.42	2018-12-20	SDSS J144132.85+481214.9	0.0297	16.34 ± 0.02	Y	N

Table 1
(Continued)

Survey Name	IAU Name	R.A. (J2000)	Decl. (J2000)	Discovery Date	Host Galaxy	$z_{\rm host}$[b]	$V_{\rm peak}$[c]	ASAS-SN?[d]	Complete?[e]
	2019np	10:29:21.960	+29:30:38.40	2019-01-09	NGC 3254	0.00452	13.38 ± 0.01	Y	Y
ATLAS19bfk	2019so	12:42:36.430	−40:44:47.06	2019-01-14	NGC 4622	0.014567	16.66 ± 0.01	Y	N
J140216[a]		14:02:16.0	−53:32:28.8	2019-01-21	ESO 174-G 005	0.01257	16.23 ± 0.01	Y	Y
ATLAS19ltg	2019gbx	12:50:02.804	−14:46:00.23	2019-05-29	MCG -02-33-017	0.013059	14.82 ± 0.01	Y	N
ATLAS19nkr	2019hxc	11:35:22.843	−21:42:54.91	2019-06-21	ESO 571-G 006	0.012158	16.44 ± 0.03	Y	N
ASASSN-19qw	2019knt	10:35:50.419	−34:16:22.04	2019-07-03	ESO 375-G 070	0.012826	14.87 ± 0.02	Y	N
ASASSN-19qr	2019khf	11:41:27.641	−38:38:03.62	2019-07-03	TOLOLO 00091	0.013756	15.15 ± 0.02	Y	N
Gaia19ded	2019ltt	07:15:43.300	−71:55:10.02	2019-07-24	6dF J0715407-715525	0.017779	15.66 ± 0.01	N	N
DLT19n	2019swh	07:22:09.108	−29:13:35.44	2019-10-06	ESO 428-G 023	0.010124	14.86 ± 0.04	Y	N
	2020ue	12:42:46.780	02:39:34.20	2020-01-12	NGC 4636	0.003129	12.18 ± 0.01	Y	N

Notes. J020622: PSN J02062253-5201267, J122100: PSN J122100.9-533150.1, J015053: PSN J01505356-3600308, J103747: MASTER OT J103747.94-270507.2, J010720: PSN J01072038+3223598, J215050: PSN J21505094-7020289, J150530: PSN J15053007+0138024, J110533: PSN J110533.80+194118.7, J150915: CSS170619:150915-112003, J140216: PSN J140216.0-533228.8, J141551: MASTER OT J141551.21-480802.6, J213123: PSN J21312375+4336312, J033333: MASTER OT J033333.26-623314.7, J114925: PSN J11492548-0507138, J073615: PSN J07361576-6930230, J112345: PSN J11234588-0106212.

[a] These names are used for brevity, and their corresponding full names are listed below.

[b] Host-galaxy heliocentric spectroscopic redshifts taken from the NASA/IPAC Extragalactic Database (NED) or from new spectroscopic measurements in Table 2. If the host-galaxy spectroscopic redshift is not available, then the SN spectroscopic redshift is displayed here instead and is indicated with an asterisk. ASASSN-18nt (2018ctv) was discovered in the galaxy cluster Abell 0194 (Chen et al. 2018), which was found to be not associated with any obvious galaxy in the cluster, but is located in the intracluster light appearing to bridge between the galaxy pair NGC545+547 and NGC541 (Moral-Pombo et al. 2018). Here we adopt the redshift of the galaxy cluster for ASASSN-18nt (Struble & Rood 1999).

[c] Peak magnitudes in V band obtained from a template fitting with *max_model* in SNooPy. For targets without successful template fitting results, if they are detected in ASAS-SN data and with redshift $z < 0.02$, the upper limits for the peak magnitudes derived from available data are reported here. Dong et al. (2018) estimated $V_{\rm max} \sim 15.7$ for 2016brx by matching its data to the light curves of SN 1991bg.

[d] Whether the SN was detected by the ASAS-SN survey.

[e] Whether the SN belongs to our complete sample.

(This table is available in machine-readable form.)

Table 2
Host Spectroscopic Redshifts without Available NED Information

SN[a]	z_{SN}	Host Galaxy	z_{host}	Telescope/Instrument
ASASSN-15hx	N/A	uncataloged	0.00812	Magellan/IMACS
ASASSN-15rq	0.025	MRSS 349-038278	0.02307	Magellan/LDSS3
ASASSN-15rw	0.02	WISEA J021558.50+121414.4	0.01884	F18[b]
ASASSN-15ti	0.016	WISEA J030510.59+375359.9	0.01732	F18[b]
ASASSN-15uh	0.0135	KUG 0925+693	0.01489	LBT/MODS
2016ag	0.0187	WISEA J013123.32+601912.5	0.01461	Shane/KAST
2016asf	0.021	KUG 0647+311	0.018019	F18[b]
2016blc	0.012	WISEA J104848.74-201547.4	0.01285	F18[b]
2016dxv	0.02	uncataloged	0.02431	P200/DBSP
2016cbx	0.015	WISEA J115054.33+021827.0	0.0285	Magellan/LDSS3
2016cyl	0.016	WKK 2066	0.01646	Magellan/LDSS3
2016daj	0.032	MCG +03-06-031	0.03026	P200/DBSP
2016ekt	0.017	WISEA J215327.93-342421.2	0.01431	Magellan/LDSS3
2016fob	0.024	CGMW 2-2125	0.0187	Magellan/LDSS3
2016gfr	0.014	WISEA J181935.67+234714.0	0.01671	P200/DBSP
2016hsc	0.007	LEDA 179577	0.0145	Magellan/IMACS
2016gou	0.016	WISEA J180806.45+252431.8	0.0155	P200/DBSP
2016gsn	0.018	WISEA J022917.19+180516.3	0.01505	P200/DBSP
2016gtr	0.014	WISEA J181935.67+234714.0	0.02033	Magellan/IMACS
2016iil	0.024	WISEA J033334.19-623303.4	0.0289	Magellan/IMACS
2016hpw	0.02	WISEA J210907.40-180607.8	0.02102	P200/DBSP
2016jab	0.021	uncataloged	0.0216	Magellan/IMACS
2017ae	0.022	uncataloged	0.0275	Shane/KAST
2017azw	0.02	ESO 015-G 010	0.01616	Magellan/LDSS3
2017cav	0.025	uncataloged	0.02096	GTC/OSIRIS
2017eck	0.025	uncataloged	0.0233	GTC/OSIRIS
2017gup	0.016	WISEA J032934.19+105825.5	0.02316	P200/DBSP
2017hjy	0.007	WISEA J023602.13+432817.6	0.0177	Hiltner/OSMOS
2017hoq	0.02	WISEA J051920.10-173647.6	0.02341	Hiltner/OSMOS
2017iyw	0.0215	VII Zw 218	0.0174	Hiltner/OSMOS
2018vw	0.02	MRSS 481-014096	0.0220	VLT/FORS2
2018aye	0.017	SDSS J175740.70+500154.1	0.0223	P200/DBSP
2018brz	0.019	WISEA J083322.17-763736.1	0.0193	Magellan/LDSS3
2018cuh	0.012	ESO 385-G 045	0.01411	Magellan/LDSS3
2018cuw	0.024	WISEA J184614.46+355820.2	0.02682	Shane/KAST
2018enc	0.017	uncataloged	0.02389	Magellan/LDSS3
2018fop	0.02	uncataloged	0.02121	Magellan/LDSS3
2018fhw	N/A	LEDA 330802	0.0170	ATEL 11980[c]
2018fnq	0.019	WISEA J201229.79-440631.4	0.01906	Magellan/LDSS3
2018htw	0.02	uncataloged	0.0206	Shane/KAST
2018ilu	0.007	uncataloged	0.01807	GTC/OSIRIS
2018jjd	0.023	MRSS 420-017372	0.0256	du Pont/WFCCD
2018jmo	0.02	2MASX J06512361+4538445	0.0209	Shane/KAST
2018kmu	0.02	SDSS J144132.85+481214.9	0.0297	Shane/KAST

Notes.
[a] The SN name adopts the IAU name when available or otherwise the survey name. All the IAU and survey names are available in Table 1.
[b] Host redshifts are obtained from the Foundation Supernova Survey (Foley et al. 2018).
[c] Host redshift of 2018fhw was first reported in Eweis et al. (2018).

photometric pipeline *PmPyeasy* to automatically process the images and obtain the photometry. The pipeline uses several external software packages that are all wrapped in a Python interface. The pipeline runs automatically by default, but allows manual operations at any point when necessary. The pipeline uses *pyds9*[42] to facilitate human inspections through XPA messaging to SAOImageDS9.[43] It takes images that have already been preprocessed, including bias removal and flat-fielding. Below we outline our procedures, and at the end of the section, we summarize our reduction of the UVOT data.

3.1. Image Registration and Source Detection

The pipeline distributes all the images to object-specific folders and adds information such as the filter, exposure time, and epoch to a database. Next, it removes cosmic rays using an implementation of the L.A.Cosmic algorithm (van Dokkum 2001), measures the FWHM of the stellar profiles, and estimates the background value for each image. It then employs *PyRAF daofind* to generate a source catalog for each image.

[42] http://hea-www.harvard.edu/RD/pyds9/
[43] https://sites.google.com/cfa.harvard.edu/saoimageds9

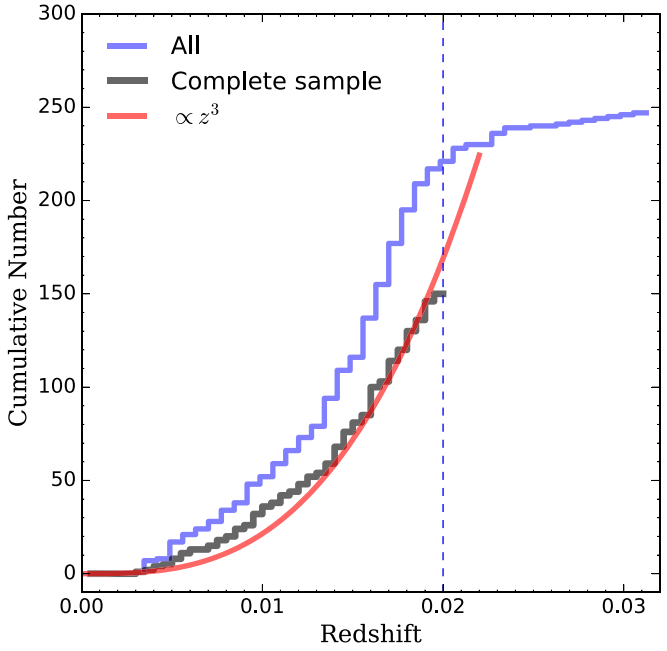

Figure 1. The cumulative redshift distribution of all SNe Ia (blue histogram) in DR1 and those in the complete sample (black histogram) from the CNIa0.02 project. The redshift limit of $z = 0.02$ for the complete sample is indicated with the dashed vertical blue line. An illustrative $N \propto z^3$ is plotted with the red line to indicate a simplified expectation from a volume-limited sample covering the full luminosity range by assuming a linear relation between distance and redshift. The distribution approximately follows the expectation for a volume-limited sample at $z \gtrsim 0.01$, for which peculiar velocities are negligible compared to the Hubble expansion velocity. The apparent excess of SNe with $0.005 \lesssim z \lesssim 0.013$ with respect to the volume-limited expectation is probably contributed by the effects of peculiar velocities at low redshift and/or fluctuations due to small number statistics.

3.2. PSF Photometry and Image Subtraction

We perform point-spread function (PSF) photometry for SNe that have negligible host-galaxy contaminations using DoPHOT (Schechter et al. 1993; Alonso-García et al. 2012). For each image, DoPHOT generates a PSF model automatically and yields magnitudes for point sources.

A large number of targets (102 out of 247 SNe) have significant host-galaxy background fluxes and require image subtraction. To perform image subtraction, the pipeline first matches point sources detected on the science image with those on the template image, and then the science image is astrometrically aligned to the same reference frame of the template image using the matched sources and resampled. The image subtraction is done with the High Order Transform of PSF ANd Template Subtraction package (HOTPANTS; Becker 2015). The FWHMs of the template and resampled science image are used to determine the convolution direction: images with better seeings are convolved with the kernel for subtraction. We configured HOTPANTS to normalize the fluxes measured on all subtracted images to the template's flux scale. To perform photometry for targets after image subtraction, the pipeline first identifies isolated stars with high signal-to-noise ratios on the template image, and these stars are used to build a PSF model for each convolved image. Then PSF photometry is performed at the SN position on the subtracted image and for all the sources on the template image using the *PyRAF daophot* task.

In some cases, host-galaxy flux subtraction is required, but image subtraction is not feasible when too few reference stars are available in the observed field or when template images are not available. If an SN is under such a circumstance and its host galaxy has a smooth profile that can be characterized by an isophote model (e.g., an elliptical galaxy), we devise a method to subtract the host-galaxy flux by incorporating an ellipse isophote modeling of the host galaxy. We adopt the following steps: (1) perform the usual PSF photometry with *PyRAF/daophot* for point sources (including the SN) within the region to be fitted by an isophote model; (2) subtract the point sources from the image, and then use the *isophote/ellipse* task from *PyRAF/stsdas* package to model the host-galaxy flux on the point-source-subtracted image; (3) subtract the best-fit isophote model from the original image and then perform PSF photometry for the stellar objects on the galaxy-flux-subtracted image; (4) steps (2) and (3) are then performed iteratively for three more times. In each iteration, the isophote model for the galaxy and the PSF photometry for the stellar objects are refined. This method has been used for the following targets with corresponding telescope/instruments given in the parentheses: 2017jfw (SMARTS), 2018ast (LCOGT 2m, PO, LT, MDM), ASASSN-18an (SMARTS), ASASSN-18en (SMARTS), 2016fnr (NOT), 2016gfr (NOT), 2016iuh (MDM), ASASSN-16la (MDM), and ASASSN-17fr (du Pont/SITe2K).

3.3. Photometric Calibration

For photometric calibration, we transform our photometry to the standard Johnson magnitudes (BV) in Vega system and SDSS magnitudes (ri) in AB magnitude system, respectively, using the reference stars with available calibrated magnitudes in the field. Since our targets cover the full sky, the preferred sources for reference stars should be an all-sky catalog with homogeneous photometric calibrations. We use the photometric system defined by the Pan-STARRS1 (PS1) survey (Chambers et al. 2016), which has a well-characterized photometric system, with transformations to other standard photometric systems available in Tonry et al. (2012). The PS1 3π Steradian Survey (Chambers et al. 2016) has multiband ($grizy_{P1}$) coverage of the sky with declinations $>-30°$, and we use photometry given in the Pan-STARRS1 DR1 MeanObject database (Flewelling et al. 2020). For the remaining quarter of the sky, we use the ATLAS All-Sky Stellar Reference Catalog (Refcat2), which was assembled from a variety of sources and brought onto the the same photometric system as Pan-STARRS1 (Tonry et al. 2018b). Before being used for photometric calibrations of our targets, the PS1 (or Refcat2) magnitudes of the reference stars in the fields are first converted into Johnson BV and SDSS ri bands adopting the following transformations (Tonry et al. 2012):

$$B_{\rm Johnson} = g_{\rm PS1} + 0.212 + 0.556\,(g_{\rm PS1} - r_{\rm PS1}) + 0.034\,(g_{\rm PS1} - r_{\rm PS1})^2,$$

$$V_{\rm Johnson} = r_{\rm PS1} + 0.005 + 0.462\,(g_{\rm PS1} - r_{\rm PS1}) + 0.013\,(g_{\rm PS1} - r_{\rm PS1})^2,$$

$$r_{\rm SDSS} = r_{\rm PS1} - 0.001 + 0.004\,(g_{\rm PS1} - r_{\rm PS1}) + 0.007(g_{\rm PS1} - r_{\rm PS1})^2,$$

$$i_{\rm SDSS} = i_{\rm PS1} - 0.005 + 0.011(g_{\rm PS1} - r_{\rm PS1}) + 0.010(g_{\rm PS1} - r_{\rm PS1})^2.$$

In practice, we use reference stars brighter than 19 mag in the field. For a target using PSF photometry, our measured magnitudes of the references are matched to standard

magnitudes to derive a zeropoint offset for each image. For a target using image subtractions, the flux scale of the template is calibrated using the references, and then all measured magnitudes are scaled to the same photometric system as the template. The photometric uncertainties are estimated by quadratically combining the photometric errors reported by DoPHOT or *PyRAF daophot* with those of the zeropoint calibrations into the standard systems. The typical uncertainty of our calibrated photometry is $\sim$0.05 mag.

3.4. Swift UVOT Photometry

In this section, we briefly describe how we perform Swift UVOT *bv* photometry, and detailed discussions and results of our full Swift SNe Ia campaign will be given in a future paper. Processed Swift UVOT images are downloaded from the Swift Archive.[44] We follow the same basic photometric procedures as described in Brown et al. (2014). We use the calibration database (CALDB) version released on 2020 December 15, which includes the revised photometric zeropoints (Breeveld et al. 2011) and latest time-dependent detector sensitivity. We follow the Swift UVOT standard photometric calibrations (Poole et al. 2008; Breeveld et al. 2010) to extract the source counts on the science images and the host-galaxy counts on the template images with an aperture with radius of 5″. We subtract the host-galaxy contributions and then convert the source count rates into magnitudes in the UVOT-Vega system.

4. Results

4.1. Light-curve Data

In this section, we present the optical light curves of 247 SNe Ia. Most of them have ASAS-SN *Vg*-band light curves using image subtractions (see Jayasinghe et al. 2018 for descriptions of the ASAS-SN image-subtraction photometry). For 219 SNe, we conducted *BVri* follow-up observations with the LCOGT 1 m and PO telescopes, and the light curves for all of them are included in DR1. *BV* light curves for 24 SNe obtained with SMARTS 1.3 m telescope are included in this data release. We also include *BVri* light curves for several targets obtained from the LCOGT 2 m telescope, LT, DEMONEXT, and A77 as well as relatively late-phase data for a small number of targets from Hiltner, du Pont, and NOT. The light curves are given in Table 3; they are the main result of CNIa0.02 DR1. In Figure 2 we show the multiband light curves up to 80 days past *B*-band peak (or the time of discovery if peak time is not available).

4.2. Light-curve Parameters

As discussed in Section 2, the *V*-band peak magnitude $V_{\rm peak} < 16.5$ is one of the criteria for the complete sample of CNIa0.02. To obtain the *V*-band peak magnitudes of SNe Ia presented in Table 1, we used the SNooPy[45] (Burns et al. 2011) software to fit (using the *"max_model"*) the observed light curves with SNe Ia template light curves. The light curves are shifted in both phase and brightness to find the best match with a set of template light curves characterized by the color-stretch parameter s_{BV}, which is found to be tightly correlated with the peak luminosity across the full range of SN Ia decline rate (Burns et al. 2014). s_{BV}, *B*-band peak time $t_{\rm peak}(B)$, and the peak magnitudes in all bands involved are free parameters. Swift UVOT *bv* data are not included in our fitting, except for two SNe (2017emq and 2017fbj) whose UVOT light curves have the essential coverage missed by other sites. Since the follow-up *V*-band data are generally more precise and have better coverage than ASAS-SN, we only include ASAS-SN *V*-band data in cases where follow-up *V*-band data are unavailable. During the fitting process, $>5\sigma$ outliers from the model were removed iteratively. The best-fit parameters ($t_{\rm peak}(B)$, s_{BV}, $B_{\rm peak}$, $g_{\rm peak}$, $V_{\rm peak}$, $r_{\rm peak}$, and $i_{\rm peak}$) for 232 SNe Ia in CNIa0.02 are given in the *max_model* section of Table 4, and the corresponding best-fit models are displayed in Figure 2.

We also fit the data using SNooPy's *"EBV_model2"*, which can derive host-galaxy extinctions. The *EBV_model2* method fit the light curves with the templates as described below,

$$m_X(\phi) = T_X(\phi, s_{BV}) + M_X(s_{BV}) + \mu + K_{XY} + R_X^{\rm MW} \cdot E(B-V)_{\rm MW} + R_X^{\rm host} \cdot E(B-V)_{\rm host}, \quad (1)$$

where m_X is the observed magnitude in band *X*, $T_X(\phi, s_{BV})$ is the template light curve as a function of rest-frame phase ϕ, and s_{BV}, $M_X(s_{BV})$ is the peak absolute magnitude of the given s_{BV}, μ is the distance modulus in magnitudes, K_{XY} is the cross-band *k*-correction from *Y* band to the observed *X* band, $E(B-V)_{\rm gal}$ and $E(B-V)_{\rm host}$ are galactic and host-galaxy color excess due to extinction, and $R_X^{\rm gal}$ and $R_X^{\rm host}$ are the ratios of total to selective extinction for the Milky Way and the host galaxy, respectively. Among the parameters listed above, $M_X(s_{BV})$, K_{XY}, $E(B-V)_{\rm MW}$, $R_X^{\rm MW}$, $R_X^{\rm host}$ are predetermined and provided by SNooPy, and $t_{\rm peak}(B)$, s_{BV}, $E(B-V)_{\rm host}$, and μ are free parameters in the fitting. $E(B-V)_{\rm MW}$ is obtained from the results of Schlafly & Finkbeiner (2011), and the canonical $R_V^{\rm MW} = 3.1$ is adopted for the Milky Way. SNooPy has different sets of calibration results of the peak luminosity of SNe Ia, and we adopt $R_V^{\rm host} = 1.729$ (corresponding to calibration = 5 in SNooPy), which is the result of calibration by using SNe Ia covering the full range of s_{BV} (Burns et al. 2014). Our data set generally has the best coverage in *BVri*, and light curves in these bands are used in the *EBV_model2* fitting for all objects, except for four objects (2018hkq, 2018htw, 2018kmu, and 2019swh). When the *g*-band light curves provide coverage missed by other bands, they are also used in the fitting. We obtain the best-fit parameters ($t_{\rm peak}(B)$, s_{BV}, $E(B-V)_{\rm host}$, and μ) for 212 SNe Ia, and they are listed in the *EBV_model2* section of Table 4.

We also perform model-independent fitting to the well-covered SN Ia light curves to directly derive parameters including the times and magnitudes of peak brightness and the decline rates in the *B* and *V* bands. The decline rate $\Delta m_{15}(X)$ (Phillips 1993) refers to the magnitude decline within 15 days after peak brightness in a given filter *X*. We measure these parameters directly from the interpolated light curves in *B* and *V* band using a Gaussian process regression method, which has the advantage of allowing for the inclusion of uncertainty information and producing relatively unbiased estimates of interpolated values (see, e.g., Lochner et al. 2016). The results are given in Table 5. Note that the fitting is performed without making host-galaxy extinction corrections, which may affect the derived Δm_{15} for objects with high extinction (Phillips et al. 1999).

[44] https://heasarc.gsfc.nasa.gov/FTP/swift/
[45] https://csp.obs.carnegiescience.edu/data/snpy/snpy

Table 3
Optical Photometry Results

SN	JD	Mag	Mag_err	Filter	Sub[a]	Isophote[b]	Source
2018jky	2,458,456.7064	18.14	0.21	*g*	Y	N	ASAS-SN
2018jky	2,458,457.6502	17.78	0.11	*g*	Y	N	ASAS-SN
2018jky	2,458,458.7521	17.21	0.07	*g*	Y	N	ASAS-SN
2018jky	2,458,459.7366	16.72	0.06	*g*	Y	N	ASAS-SN
2018jky	2,458,461.6346	16.26	0.05	*g*	Y	N	ASAS-SN
2018jky	2,458,462.7428	16.03	0.04	*g*	Y	N	ASAS-SN
2018jky	2,458,463.4105	15.99	0.04	*g*	Y	N	ASAS-SN
2018jky	2,458,459.7223	16.90	0.04	*B*	N	N	LCOGT1m
2018jky	2,458,462.3664	16.01	0.04	*B*	N	N	LCOGT1m
2018jky	2,458,464.3421	15.68	0.06	*B*	N	N	LCOGT1m
2018jky	2,458,464.7235	15.65	0.05	*B*	N	N	LCOGT1m
2018jky	2,458,459.7253	16.68	0.03	*V*	N	N	LCOGT1m
2018jky	2,458,462.3691	15.99	0.03	*V*	N	N	LCOGT1m
2018jky	2,458,464.3448	15.67	0.02	*V*	N	N	LCOGT1m
2018jky	2,458,464.7262	15.62	0.04	*V*	N	N	LCOGT1m
2018jky	2,458,459.7239	16.66	0.03	*r*	N	N	LCOGT1m
2018jky	2,458,462.3678	15.95	0.03	*r*	N	N	LCOGT1m
2018jky	2,458,464.3435	15.64	0.04	*r*	N	N	LCOGT1m
2018jky	2,458,464.7249	15.76	0.06	*r*	N	N	LCOGT1m
2018jky	2,458,459.7209	16.91	0.06	*i*	N	N	LCOGT1m
2018jky	2,458,462.3651	16.15	0.05	*i*	N	N	LCOGT1m
2018jky	2,458,464.3407	15.84	0.08	*i*	N	N	LCOGT1m
2018jky	2,458,464.7222	15.88	0.12	*i*	N	N	LCOGT1m
2018jky	2,458,461.6689	16.26	0.12	*B*	N	N	PO
2018jky	2,458,463.6687	15.76	0.12	*B*	N	N	PO
2018jky	2,458,475.6687	15.90	0.13	*B*	N	N	PO
2018jky	2,458,461.6780	16.14	0.03	*V*	N	N	PO
2018jky	2,458,463.6779	15.77	0.04	*V*	N	N	PO
2018jky	2,458,475.6778	15.49	0.03	*V*	N	N	PO
2018jky	2,458,461.6873	16.11	0.04	*r*	N	N	PO
2018jky	2,458,463.6871	15.72	0.05	*r*	N	N	PO
2018jky	2,458,475.6872	15.54	0.05	*r*	N	N	PO
2018jky	2,458,461.6965	16.23	0.09	*i*	N	N	PO
2018jky	2,458,463.6963	15.86	0.06	*i*	N	N	PO
2018jky	2,458,475.6965	16.10	0.10	*i*	N	N	PO
2018jky	2,458,460.6398	16.57	0.08	*B*	N	N	SMARTS
2018jky	2,458,462.6273	16.02	0.10	*B*	N	N	SMARTS
2018jky	2,458,464.6166	15.68	0.08	*B*	N	N	SMARTS
2018jky	2,458,460.6414	16.45	0.14	*V*	N	N	SMARTS
2018jky	2,458,462.6289	15.92	0.14	*V*	N	N	SMARTS
2018jky	2,458,464.6181	15.81	0.20	*V*	N	N	SMARTS
2018jky	2,458,699.8305	22.14	0.19	*R*	N	N	WFCCD
2018jky	2,458,699.8350	22.42	0.19	*R*	N	N	WFCCD
2018jky	2,458,699.8395	22.17	0.18	*R*	N	N	WFCCD
2018jky	2,458,699.8259	21.44	0.11	*V*	N	N	WFCCD

Notes.
[a] Whether image subtraction is used for photometry.
[b] Whether the isophote model is used to subtract the host-galaxy flux. See Section 3.2 for a detailed description of how the isophote model works for the photometry.
(This table is available in its entirety in machine-readable form.)

Figure 3 shows the histogram of all available direct $\Delta m_{15}(B)$ measurements for CNIa0.02 DR1. The left panel is for the SNe included in CNIa0.02 DR1, and the right panel is for those in the complete sample. Our objects include SNe Ia spanning the full range of $\Delta m_{15}(B)$ of the SN Ia population from $\Delta m_{15}(B) \approx 0.7$ mag to $\Delta m_{15}(B) \approx 2.0$ mag. The complete sample consists of SNe Ia with $z < 0.02$ and $V_{\rm peak} < 16.5$ mag, and due to the peak magnitude limits, our sample is not sensitive to all dim SNe Ia with high $\Delta m_{15}(B)$ values within the volume confined by $z < 0.02$. Further work to quantify the detection efficiency within different $\Delta m_{15}(B)$ bins needs to be carried out to obtain the intrinsic distribution of $\Delta m_{15}(B)$ and other parameters for the SNe Ia population.

5. Summary

CNIa0.02 aims to obtain a homogeneous and unbiased sample of nearby SNe Ia with multiband light curves to study the SNe Ia population. In CNIa0.02 DR1, we present 247 SNe with optical light curves, including 148 SNe in the complete sample. DR1 offers large and homogenous optical photometric data sets to systematically study the SNe Ia population. In this paper, we present the first analysis of our data set by extracting

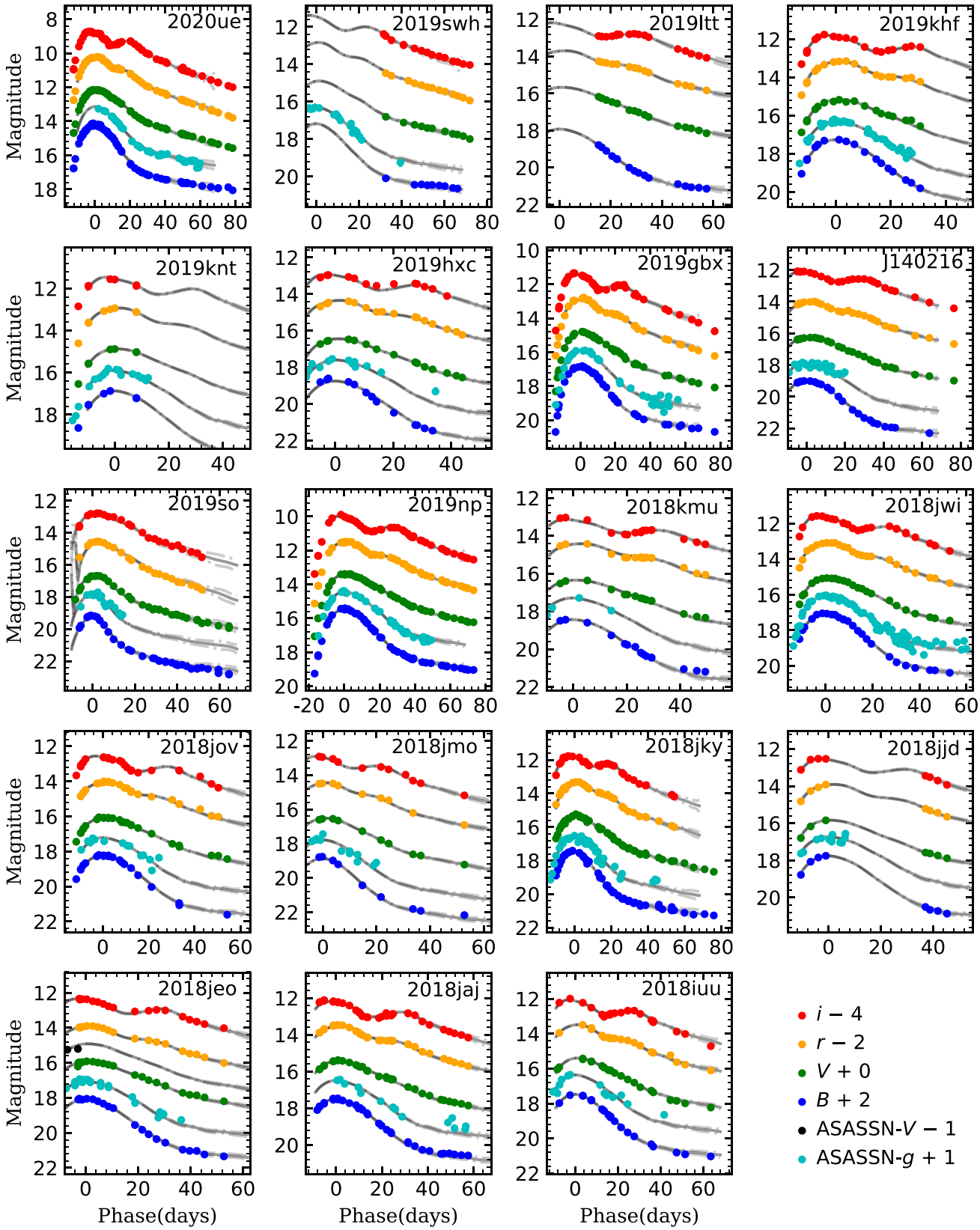

Figure 2. Multiband light curves of SNe Ia in DR1. Here we show the light curves for 19 SNe Ia in DR1 with the most recent discovery time. The black lines correspond to the fitting results using the *max_model* fitting of SNooPy, and the corresponding best-fit parameters are given in Table 4 (see Section 4.2). All phases in days are with respect to the time of *B*-band peak obtained from the *max_model* fitting. The complete figure set contains all all SNe Ia with multiband light curves in reverse chronological order according to the time of discovery.

(The complete figure set (11 images) is available.)

Table 4
Light-curve Parameters from SNooPy Template Fitting

	max_model							*EBV_model2*				
SN[a]	$t_{peak}(B)$	s_{BV}	B_{peak}	g_{peak}	V_{peak}	r_{peak}	i_{peak}	$t_{peak}(B)$	s_{BV}	E $(B-V)_{host}$	μ	Category[c]
	−2,457,000		(mag)	(mag)	(mag)	(mag)	(mag)	−2,457,000		(mag)	(mag)	
ASASSN-15aj	36.22 ± 0.25	0.75 ± 0.04	15.01 ± 0.04	⋯	14.77 ± 0.02	14.77 ± 0.03	15.15 ± 0.03	36.29 ± 0.22	0.74 ± 0.04	0.13 ± 0.04	33.22 ± 0.05	C2
ASASSN-15ak	38.15 ± 0.31	0.95 ± 0.06	14.80 ± 0.08	⋯	14.70 ± 0.01	14.76 ± 0.05	15.29 ± 0.09	38.02 ± 0.14	0.95 ± 0.03	0.09 ± 0.01	33.64 ± 0.04	C2
ASASSN-15db	76.37 ± 0.30	0.86 ± 0.05	⋯	⋯	14.55 ± 0.03	⋯	⋯	⋯	⋯	⋯	⋯	C1
ASASSN-15eb	82.57 ± 0.74	1.02 ± 0.09	15.89 ± 0.06	⋯	15.82 ± 0.05	15.79 ± 0.04	16.35 ± 0.08	82.38 ± 0.75	1.02 ± 0.07	−0.04 ± 0.05	34.65 ± 0.10	C2
2015F	107.60 ± 0.21	0.86 ± 0.02	⋯	⋯	13.31 ± 0.02	⋯	⋯	⋯	⋯	⋯	⋯	C1
2015bp	113.10 ± 0.13	0.71 ± 0.02	⋯	⋯	13.90 ± 0.01	⋯	⋯	⋯	⋯	⋯	⋯	C0
ASASSN-15ga	116.66 ± 0.15	0.45 ± 0.02	15.77 ± 0.05	⋯	15.08 ± 0.03	15.10 ± 0.02	15.28 ± 0.03	116.59 ± 0.18	0.46 ± 0.02	0.14 ± 0.06	32.95 ± 0.05	C0
ASASSN-15go	125.14 ± 0.53	0.60 ± 0.21	16.42 ± 0.13	⋯	16.04 ± 0.09	15.91 ± 0.44	16.38 ± 0.21	125.84 ± 0.69	0.71 ± 0.15	0.12 ± 0.12	34.27 ± 0.24	C2
ASASSN-15hf	137.71 ± 0.16	1.00 ± 0.02	⋯	⋯	14.27 ± 0.02	⋯	⋯	⋯	⋯	⋯	⋯	C1
ASASSN-15hx	152.12 ± 0.04	1.06 ± 0.01	13.33 ± 0.01	⋯	13.37 ± 0.01	13.42 ± 0.01	14.04 ± 0.01	152.04 ± 0.05	1.01 ± 0.01	−0.03 ± 0.01	32.54 ± 0.02	C0
ASASSN-15jo	169.29 ± 0.06	0.58 ± 0.01	15.69 ± 0.01	⋯	15.30 ± 0.02	15.41 ± 0.01	15.79 ± 0.01	169.32 ± 0.11	0.57 ± 0.01	0.01 ± 0.02	33.72 ± 0.02	C0
ASASSN-15kg	182.30 ± 0.77	0.61 ± 0.11	15.48 ± 0.17	⋯	15.16 ± 0.05	⋯	⋯	182.31 ± 0.76	0.61 ± 0.11	0.16 ± 0.21	33.37 ± 0.22	C0
ASASSN-15kp	189.69 ± 0.18	0.98 ± 0.01	15.53 ± 0.01	⋯	15.48 ± 0.01	⋯	⋯	189.69 ± 0.18	0.97 ± 0.01	0.02 ± 0.01	34.45 ± 0.04	C0
ASASSN-15kx	195.91 ± 1.52	1.24 ± 0.24	⋯	⋯	16.14 ± 0.06	⋯	⋯	⋯	⋯	⋯	⋯	C1
ASASSN-15lp	188.29 ± 2.89	1.12 ± 0.15	14.90 ± 0.22	⋯	15.01 ± 0.14	⋯	⋯	188.35 ± 2.38	1.12 ± 0.14	−0.18 ± 0.19	34.50 ± 0.33	C0
J114925[b]	216.48 ± 0.08	0.84 ± 0.01	13.29 ± 0.02	⋯	13.26 ± 0.01	⋯	⋯	216.48 ± 0.08	0.84 ± 0.01	0.01 ± 0.02	32.26 ± 0.04	C0
ASASSN-15mc	217.08 ± 0.74	1.51 ± 0.10	15.55 ± 0.02	⋯	15.10 ± 0.02	⋯	⋯	217.05 ± 0.74	1.49 ± 0.10	0.07 ± 0.18	33.81 ± 0.19	C2
2015aw	225.40 ± 0.44	0.91 ± 0.06	⋯	⋯	15.57 ± 0.04	⋯	⋯	⋯	⋯	⋯	⋯	C1
ASASSN-15ml	210.62 ± 2.84	0.78 ± 0.06	17.51 ± 0.34	⋯	16.83 ± 0.17	⋯	⋯	210.72 ± 2.72	0.77 ± 0.06	0.55 ± 0.16	34.22 ± 0.22	C2
ASASSN-15od	257.22 ± 0.23	0.86 ± 0.04	15.51 ± 0.05	⋯	15.45 ± 0.03	⋯	⋯	257.23 ± 0.23	0.86 ± 0.04	0.06 ± 0.06	34.36 ± 0.07	C0
ASASSN-15oh	256.14 ± 0.71	0.89 ± 0.18	⋯	⋯	16.15 ± 0.06	⋯	⋯	⋯	⋯	⋯	⋯	C1
ASASSN-15ol	259.94 ± 0.45	1.04 ± 0.09	15.93 ± 0.06	⋯	15.77 ± 0.05	⋯	⋯	259.93 ± 0.45	1.04 ± 0.09	0.19 ± 0.09	34.62 ± 0.24	C2
ASASSN-15pl	288.16 ± 0.68	1.10 ± 0.07	15.26 ± 0.11	⋯	15.17 ± 0.04	15.34 ± 0.05	15.93 ± 0.08	288.11 ± 0.72	1.12 ± 0.05	−0.01 ± 0.05	34.48 ± 0.08	C0
ASASSN-15pz	307.87 ± 0.09	1.37 ± 0.01	14.26 ± 0.01	⋯	14.25 ± 0.01	14.45 ± 0.01	14.90 ± 0.01	308.07 ± 0.14	1.34 ± 0.01	−0.13 ± 0.01	33.64 ± 0.02	C4
ASASSN-15qc	300.88 ± 0.17	0.99 ± 0.01	15.93 ± 0.02	⋯	15.56 ± 0.01	15.57 ± 0.01	16.18 ± 0.02	299.37 ± 0.23	1.19 ± 0.02	0.21 ± 0.02	34.47 ± 0.04	C0

Table 4
(Continued)

	max_model							*EBV_model2*				
SN[a]	$t_{peak}(B)$	s_{BV}	B_{peak}	g_{peak}	V_{peak}	r_{peak}	i_{peak}	$t_{peak}(B)$	s_{BV}	E $(B-V)_{host}$	μ	Category[c]
2015ao	308.30 ± 0.15	0.40 ± 0.02	17.52 ± 0.03	⋯	16.90 ± 0.02	16.91 ± 0.03	17.12 ± 0.04	308.27 ± 0.15	0.38 ± 0.02	0.03 ± 0.03	34.69 ± 0.06	C0
2015dc	293.54 ± 2.45	0.98 ± 0.27	15.33 ± 0.22	⋯	15.30 ± 0.24	15.63 ± 0.33	16.07 ± 0.35	296.23 ± 2.08	0.63 ± 0.20	−0.17 ± 0.08	33.97 ± 0.55	C0
ASASSN-15rq	325.25 ± 0.10	1.19 ± 0.02	15.49 ± 0.01	⋯	15.47 ± 0.01	15.60 ± 0.01	16.03 ± 0.02	325.24 ± 0.14	1.14 ± 0.03	0.02 ± 0.02	34.72 ± 0.04	C0
ASASSN-15rw	329.63 ± 0.25	1.13 ± 0.05	15.62 ± 0.03	⋯	15.54 ± 0.03	15.60 ± 0.03	16.07 ± 0.03	329.54 ± 0.25	1.13 ± 0.04	0.00 ± 0.02	34.46 ± 0.05	C0
J213123[b]	336.14 ± 1.30	1.18 ± 0.05	17.35 ± 0.15	⋯	16.80 ± 0.08	16.77 ± 0.05	16.97 ± 0.04	334.37 ± 3.04	1.13 ± 0.09	0.09 ± 0.14	34.85 ± 0.16	C0
ASASSN-15so	347.16 ± 0.38	0.86 ± 0.03	13.96 ± 0.09	⋯	13.86 ± 0.02	13.97 ± 0.06	14.56 ± 0.07	347.36 ± 0.46	0.84 ± 0.03	0.03 ± 0.05	32.84 ± 0.08	C0
2015ar	352.92 ± 0.17	0.73 ± 0.03	15.39 ± 0.02	⋯	15.26 ± 0.01	15.44 ± 0.02	15.91 ± 0.03	352.67 ± 0.24	0.74 ± 0.02	−0.06 ± 0.02	34.14 ± 0.04	C0
J215050[b]	360.06 ± 0.08	0.86 ± 0.01	15.56 ± 0.02	⋯	15.14 ± 0.01	15.08 ± 0.01	15.44 ± 0.02	360.11 ± 0.09	0.85 ± 0.01	0.40 ± 0.02	33.44 ± 0.02	C0
ASASSN-15ti	364.81 ± 0.13	0.80 ± 0.02	16.28 ± 0.02	⋯	16.07 ± 0.02	16.06 ± 0.01	16.46 ± 0.02	364.80 ± 0.12	0.79 ± 0.02	0.07 ± 0.02	34.53 ± 0.03	C0
2015bd	346.56 ± 0.33	1.06 ± 0.03	15.35 ± 0.06	⋯	15.19 ± 0.02	15.23 ± 0.04	15.76 ± 0.04	346.41 ± 0.34	1.07 ± 0.03	0.12 ± 0.03	34.13 ± 0.06	C0
ASASSN-15uh	387.63 ± 0.17	1.22 ± 0.03	15.57 ± 0.03	⋯	15.30 ± 0.03	15.34 ± 0.02	15.77 ± 0.03	387.60 ± 0.16	1.23 ± 0.03	0.08 ± 0.02	34.05 ± 0.04	C0
ASASSN-15ut	392.12 ± 0.36	0.77 ± 0.03	16.85 ± 0.06	⋯	16.37 ± 0.04	16.31 ± 0.03	16.53 ± 0.05	392.42 ± 0.42	0.72 ± 0.05	0.42 ± 0.07	34.39 ± 0.09	C4
2016A	392.57 ± 0.75	0.90 ± 0.16	17.75 ± 0.08	⋯	16.83 ± 0.04	16.64 ± 0.07	17.01 ± 0.09	390.70 ± 1.69	1.19 ± 0.18	0.72 ± 0.13	34.70 ± 0.21	C0
2016F	406.65 ± 0.33	0.97 ± 0.06	⋯	⋯	15.26 ± 0.03	⋯	⋯	⋯	⋯	⋯	⋯	C0
2016adp	406.76 ± 0.21	0.23 ± 0.02	⋯	⋯	17.03 ± 0.08	⋯	⋯	⋯	⋯	⋯	⋯	C1
2016W	419.46 ± 0.48	0.63 ± 0.10	⋯	⋯	16.01 ± 0.03	⋯	⋯	⋯	⋯	⋯	⋯	C1
2016adi	432.67 ± 0.76	0.84 ± 0.02	15.48 ± 0.07	⋯	15.35 ± 0.05	15.43 ± 0.04	15.91 ± 0.07	432.53 ± 0.33	0.84 ± 0.01	0.04 ± 0.02	34.22 ± 0.02	C0
2016adn	428.41 ± 1.06	1.02 ± 0.06	16.26 ± 0.06	⋯	16.12 ± 0.05	16.21 ± 0.04	16.70 ± 0.08	428.28 ± 0.55	1.02 ± 0.04	−0.02 ± 0.02	34.99 ± 0.04	C0
2016asf	465.22 ± 0.27	0.82 ± 0.04	⋯	⋯	15.72 ± 0.02	⋯	⋯	⋯	⋯	⋯	⋯	C0
2016aue	423.35 ± 5.33	0.78 ± 0.22	15.00 ± 0.11	⋯	14.80 ± 0.13	14.93 ± 0.16	15.45 ± 0.20	423.22 ± 1.56	0.73 ± 0.05	−0.07 ± 0.05	33.54 ± 0.13	C0
2016bfu	471.37 ± 0.12	0.46 ± 0.01	16.25 ± 0.02	⋯	15.60 ± 0.01	15.62 ± 0.02	15.78 ± 0.02	471.28 ± 0.15	0.46 ± 0.02	0.14 ± 0.03	33.39 ± 0.05	C0
2016blc	489.88 ± 0.13	1.05 ± 0.01	14.73 ± 0.01	⋯	14.74 ± 0.01	14.90 ± 0.01	15.54 ± 0.01	489.68 ± 0.15	1.07 ± 0.01	−0.07 ± 0.01	34.11 ± 0.02	C0
2016bln	500.34 ± 0.47	1.04 ± 0.07	⋯	⋯	16.01 ± 0.04	⋯	⋯	⋯	⋯	⋯	⋯	C1
2016bry	508.91 ± 0.27	0.79 ± 0.04	⋯	⋯	15.77 ± 0.02	⋯	⋯	⋯	⋯	⋯	⋯	C1
2016bsa	505.97 ± 1.05	0.97 ± 0.10	⋯	⋯	15.99 ± 0.06	⋯	⋯	⋯	⋯	⋯	⋯	C0
2016dxv	510.96 ± 0.82	1.26 ± 0.12	⋯	⋯	16.17 ± 0.03	⋯	⋯	⋯	⋯	⋯	⋯	C0
2016cbx	513.88 ± 0.18	1.00 ± 0.03	16.67 ± 0.03	⋯	16.54 ± 0.03	16.61 ± 0.02	17.28 ± 0.03	513.63 ± 0.25	1.10 ± 0.05	0.08 ± 0.02	35.71 ± 0.05	C0
2016ccz	538.96 ± 0.33	0.85 ± 0.04	15.29 ± 0.14	⋯	15.43 ± 0.02	15.29 ± 0.08	15.82 ± 0.10	538.72 ± 0.36	0.87 ± 0.04	0.20 ± 0.11	34.12 ± 0.19	C0
2016cmn	537.30 ± 0.54	1.04 ± 0.08	⋯	⋯	16.02 ± 0.05	⋯	⋯	⋯	⋯	⋯	⋯	C0
2016coj	549.08 ± 0.07	0.90 ± 0.01	⋯	⋯	13.01 ± 0.01	⋯	⋯	⋯	⋯	⋯	⋯	C1
2016cqz	552.80 ± 0.32	0.85 ± 0.04	15.15 ± 0.07	⋯	14.91 ± 0.03	14.89 ± 0.06	15.37 ± 0.12	552.74 ± 0.30	0.85 ± 0.04	0.16 ± 0.07	33.43 ± 0.08	C0
2016cvn	556.58 ± 1.33	0.79 ± 0.13	⋯	⋯	16.38 ± 0.09	15.95 ± 0.17	16.23 ± 0.17	556.55 ± 1.32	0.87 ± 0.09	0.87 ± 0.17	33.75 ± 0.28	C2
2016cyl	560.27 ± 2.36	0.96 ± 0.23	17.00 ± 0.51	⋯	16.53 ± 0.16	16.10 ± 0.09	15.92 ± 0.19	559.69 ± 3.60	0.88 ± 0.21	0.49 ± 0.41	33.43 ± 0.43	C0
2016daj	592.48 ± 0.19	1.00 ± 0.03	16.62 ± 0.03	⋯	16.52 ± 0.02	16.63 ± 0.02	17.18 ± 0.03	592.28 ± 0.21	1.02 ± 0.03	−0.03 ± 0.02	35.55 ± 0.04	C0
2016eiy	608.76 ± 0.17	0.95 ± 0.04	14.61 ± 0.08	⋯	14.23 ± 0.02	14.24 ± 0.06	14.76 ± 0.12	608.50 ± 0.21	0.94 ± 0.03	0.25 ± 0.05	32.65 ± 0.08	C0
2016ekg	610.29 ± 0.05	0.97 ± 0.01	15.09 ± 0.01	⋯	15.07 ± 0.01	15.20 ± 0.01	15.77 ± 0.01	610.29 ± 0.05	0.98 ± 0.01	0.01 ± 0.01	34.27 ± 0.01	C0
2016ekt	603.56 ± 0.09	1.03 ± 0.01	14.78 ± 0.01	⋯	14.71 ± 0.01	14.79 ± 0.01	15.42 ± 0.01	603.34 ± 0.11	1.06 ± 0.01	0.04 ± 0.01	33.90 ± 0.02	C0
2016euj	619.57 ± 0.09	0.84 ± 0.01	15.40 ± 0.02	⋯	15.36 ± 0.01	15.51 ± 0.01	16.05 ± 0.02	619.58 ± 0.09	0.83 ± 0.01	−0.04 ± 0.02	34.49 ± 0.02	C0
2016fej	637.33 ± 0.04	1.02 ± 0.01	13.97 ± 0.01	⋯	13.91 ± 0.01	14.07 ± 0.01	14.68 ± 0.01	637.48 ± 0.05	1.01 ± 0.01	−0.01 ± 0.01	33.13 ± 0.01	C0
2016fff	630.45 ± 0.07	0.70 ± 0.01	15.06 ± 0.01	⋯	14.93 ± 0.01	14.96 ± 0.01	15.43 ± 0.01	630.47 ± 0.07	0.70 ± 0.01	0.04 ± 0.01	33.61 ± 0.02	C0

Table 4
(Continued)

	max_model							*EBV_model2*				
SN[a]	$t_{peak}(B)$	s_{BV}	B_{peak}	g_{peak}	V_{peak}	r_{peak}	i_{peak}	$t_{peak}(B)$	s_{BV}	E $(B-V)_{host}$	μ	Category[c]
2016fnr	640.70 ± 0.85	0.84 ± 0.02	15.24 ± 0.07	⋯	15.03 ± 0.04	15.13 ± 0.03	15.56 ± 0.04	640.16 ± 0.91	0.85 ± 0.02	0.10 ± 0.05	33.83 ± 0.06	C0
2016fob	631.71 ± 0.46	1.06 ± 0.04	16.38 ± 0.08	⋯	16.10 ± 0.02	16.19 ± 0.04	16.61 ± 0.07	631.64 ± 0.51	1.05 ± 0.03	0.02 ± 0.02	34.80 ± 0.04	C0
2016gfk	645.83 ± 0.36	0.86 ± 0.03	17.36 ± 0.07	⋯	16.78 ± 0.02	16.56 ± 0.04	16.75 ± 0.07	645.85 ± 0.37	0.86 ± 0.02	0.68 ± 0.02	34.49 ± 0.03	C0
2016gfr	657.25 ± 0.14	1.06 ± 0.02	15.41 ± 0.03	⋯	15.28 ± 0.03	15.37 ± 0.02	15.90 ± 0.02	657.18 ± 0.15	1.08 ± 0.03	−0.0 ± 0.02	34.27 ± 0.04	C0
2016hsc	666.79 ± 0.23	1.03 ± 0.03	15.18 ± 0.08	⋯	15.06 ± 0.02	15.11 ± 0.05	15.67 ± 0.08	666.67 ± 0.22	1.03 ± 0.02	0.05 ± 0.02	34.00 ± 0.05	C0
2016gou	666.47 ± 0.74	0.99 ± 0.03	16.11 ± 0.06	⋯	15.84 ± 0.05	15.86 ± 0.03	16.22 ± 0.07	666.66 ± 0.30	0.97 ± 0.01	0.20 ± 0.01	34.38 ± 0.02	C0
2016gsb	672.68 ± 0.08	0.99 ± 0.01	14.59 ± 0.01	⋯	14.42 ± 0.01	14.50 ± 0.02	15.13 ± 0.01	672.28 ± 0.11	1.18 ± 0.02	0.05 ± 0.02	33.61 ± 0.03	C0
2016gsn	671.65 ± 0.07	1.03 ± 0.01	15.29 ± 0.01	⋯	15.09 ± 0.01	15.18 ± 0.01	15.64 ± 0.01	671.56 ± 0.09	1.04 ± 0.01	−0.01 ± 0.01	33.88 ± 0.02	C0
2016gtr	669.12 ± 0.27	1.10 ± 0.04	15.66 ± 0.02	⋯	15.59 ± 0.01	15.70 ± 0.02	16.34 ± 0.03	669.00 ± 0.26	1.12 ± 0.04	−0.01 ± 0.02	34.82 ± 0.05	C0
2016gwl	627.62 ± 0.39	1.07 ± 0.02	14.25 ± 0.02	⋯	14.23 ± 0.02	14.42 ± 0.03	15.01 ± 0.03	626.69 ± 0.45	1.19 ± 0.01	−0.18 ± 0.02	33.70 ± 0.03	C3
2016gxp	685.94 ± 0.19	1.22 ± 0.02	15.21 ± 0.02	⋯	14.85 ± 0.01	14.80 ± 0.01	15.07 ± 0.02	686.09 ± 0.06	1.21 ± 0.02	0.29 ± 0.02	33.23 ± 0.03	C4
2016hht	683.31 ± 0.66	0.92 ± 0.02	15.61 ± 0.06	⋯	15.59 ± 0.04	15.67 ± 0.03	16.26 ± 0.07	683.27 ± 0.19	0.92 ± 0.01	0.00 ± 0.01	34.67 ± 0.02	C0
2016iil	684.41 ± 0.89	0.92 ± 0.04	16.80 ± 0.07	⋯	16.62 ± 0.05	16.68 ± 0.03	17.24 ± 0.07	683.90 ± 0.55	0.95 ± 0.03	0.10 ± 0.02	35.50 ± 0.03	C0
2016hmo	676.77 ± 0.46	1.10 ± 0.05	17.80 ± 0.05	⋯	16.85 ± 0.03	16.60 ± 0.04	16.70 ± 0.04	676.57 ± 0.50	1.09 ± 0.05	0.91 ± 0.04	34.29 ± 0.08	C0
2016hli	697.01 ± 0.09	0.70 ± 0.01	17.48 ± 0.02	⋯	16.78 ± 0.01	16.58 ± 0.01	16.64 ± 0.01	696.95 ± 0.12	0.69 ± 0.01	0.19 ± 0.02	33.91 ± 0.02	C0
2016hnk	692.09 ± 0.31	0.49 ± 0.02	19.02 ± 0.09	⋯	17.55 ± 0.03	17.35 ± 0.03	17.58 ± 0.03	693.24 ± 0.98	1.02 ± 0.10	1.08 ± 0.06	34.95 ± 0.11	C4
2016hpw	703.63 ± 0.11	1.01 ± 0.02	16.08 ± 0.02	⋯	15.96 ± 0.01	16.02 ± 0.01	16.60 ± 0.02	703.57 ± 0.12	1.01 ± 0.02	0.07 ± 0.01	34.92 ± 0.02	C0
2016hvl	710.60 ± 0.17	1.19 ± 0.02	16.06 ± 0.02	⋯	15.45 ± 0.02	15.40 ± 0.02	15.67 ± 0.03	710.51 ± 0.20	1.18 ± 0.02	0.16 ± 0.03	33.36 ± 0.05	C0
2016huh	699.91 ± 0.20	0.78 ± 0.01	17.24 ± 0.02	⋯	16.82 ± 0.01	16.70 ± 0.01	16.99 ± 0.02	699.94 ± 0.19	0.78 ± 0.01	0.27 ± 0.02	34.79 ± 0.02	C0
2016igr	726.33 ± 0.19	1.01 ± 0.01	15.39 ± 0.02	⋯	15.30 ± 0.02	15.45 ± 0.01	16.07 ± 0.01	726.04 ± 0.23	1.03 ± 0.02	0.00 ± 0.01	34.55 ± 0.03	C0
2016ins	722.99 ± 0.31	0.83 ± 0.02	16.89 ± 0.03	⋯	16.58 ± 0.02	16.55 ± 0.02	17.00 ± 0.03	722.94 ± 0.32	0.83 ± 0.02	0.26 ± 0.02	35.06 ± 0.04	C0
2016ipf	728.33 ± 0.26	0.83 ± 0.01	16.78 ± 0.02	⋯	16.70 ± 0.02	16.75 ± 0.02	17.28 ± 0.02	728.31 ± 0.26	0.83 ± 0.01	0.06 ± 0.02	35.59 ± 0.03	C0
2016itd	733.77 ± 1.21	0.99 ± 0.03	15.65 ± 0.10	⋯	15.42 ± 0.08	15.50 ± 0.08	16.12 ± 0.11	733.05 ± 0.80	1.00 ± 0.02	0.15 ± 0.03	34.37 ± 0.08	C0
2016ito	721.55 ± 0.55	1.23 ± 0.02	15.67 ± 0.03	⋯	15.64 ± 0.02	15.84 ± 0.02	16.39 ± 0.03	721.70 ± 0.49	1.22 ± 0.02	−0.11 ± 0.02	35.03 ± 0.03	C0
2016iuh	738.04 ± 0.65	0.68 ± 0.03	15.59 ± 0.07	⋯	15.40 ± 0.04	15.49 ± 0.03	15.87 ± 0.07	738.09 ± 0.25	0.67 ± 0.02	0.02 ± 0.04	34.09 ± 0.04	C0
2016jae	751.28 ± 0.19	0.53 ± 0.01	17.40 ± 0.03	⋯	16.79 ± 0.01	16.80 ± 0.01	17.15 ± 0.02	750.36 ± 0.30	0.57 ± 0.02	0.18 ± 0.03	34.90 ± 0.03	C0
2016jab	749.91 ± 0.21	1.08 ± 0.02	16.10 ± 0.01	⋯	15.95 ± 0.01	16.01 ± 0.01	16.54 ± 0.01	749.71 ± 0.21	1.09 ± 0.02	−0.02 ± 0.01	34.85 ± 0.02	C0
2017ae	769.49 ± 1.57	1.42 ± 0.25	⋯	⋯	16.41 ± 0.05	⋯	⋯	⋯	⋯	⋯	⋯	C1
2017jl	784.79 ± 0.10	1.08 ± 0.02	15.05 ± 0.01	⋯	14.94 ± 0.01	15.03 ± 0.01	15.52 ± 0.02	784.78 ± 0.11	1.07 ± 0.02	0.06 ± 0.01	33.93 ± 0.03	C0
2017yv	795.62 ± 0.12	1.00 ± 0.01	15.85 ± 0.02	⋯	15.59 ± 0.02	15.62 ± 0.02	16.15 ± 0.02	795.55 ± 0.15	1.02 ± 0.02	0.16 ± 0.01	34.40 ± 0.03	C0
2017atv	801.11 ± 0.89	0.80 ± 0.03	17.16 ± 0.08	⋯	16.59 ± 0.03	16.52 ± 0.04	16.85 ± 0.08	800.74 ± 0.53	0.82 ± 0.02	0.20 ± 0.03	34.52 ± 0.04	C0
2017aut	792.85 ± 0.94	1.13 ± 0.06	17.63 ± 0.08	⋯	17.10 ± 0.05	16.91 ± 0.05	⋯	792.84 ± 0.48	1.13 ± 0.04	0.50 ± 0.05	35.09 ± 0.09	C0
2017awk	808.37 ± 0.16	0.93 ± 0.01	16.07 ± 0.02	⋯	15.74 ± 0.01	15.77 ± 0.01	16.27 ± 0.02	808.14 ± 0.20	0.94 ± 0.01	0.20 ± 0.01	34.35 ± 0.03	C0
2017azw	817.03 ± 0.10	1.09 ± 0.02	15.00 ± 0.02	⋯	14.98 ± 0.01	15.14 ± 0.01	15.77 ± 0.01	817.00 ± 0.11	1.09 ± 0.02	−0.09 ± 0.01	34.31 ± 0.03	C0
2017bkc	811.96 ± 0.28	1.02 ± 0.02	17.21 ± 0.02	⋯	16.62 ± 0.02	16.53 ± 0.02	16.84 ± 0.02	810.50 ± 0.37	1.18 ± 0.03	0.13 ± 0.03	34.62 ± 0.04	C0
2017cav	821.33 ± 0.27	1.00 ± 0.03	16.58 ± 0.05	⋯	16.31 ± 0.01	16.36 ± 0.03	16.79 ± 0.06	820.91 ± 0.32	1.02 ± 0.02	0.02 ± 0.01	34.91 ± 0.02	C0
2017bzc	826.54 ± 0.28	1.12 ± 0.02	12.39 ± 0.02	⋯	12.29 ± 0.01	12.47 ± 0.02	13.06 ± 0.03	825.97 ± 0.42	1.11 ± 0.03	0.01 ± 0.02	31.56 ± 0.04	C3
2017cbr	834.22 ± 0.16	0.91 ± 0.01	15.98 ± 0.01	⋯	15.75 ± 0.01	15.74 ± 0.01	16.17 ± 0.01	834.22 ± 0.16	0.90 ± 0.01	0.23 ± 0.01	34.34 ± 0.02	C0
2017cbv	840.66 ± 0.05	1.19 ± 0.01	11.77 ± 0.01	⋯	11.70 ± 0.01	11.78 ± 0.01	12.23 ± 0.01	840.79 ± 0.06	1.08 ± 0.01	−0.02 ± 0.01	30.56 ± 0.02	C0
2017cfd	844.03 ± 0.06	0.93 ± 0.01	14.94 ± 0.01	⋯	14.78 ± 0.01	14.82 ± 0.01	15.34 ± 0.01	844.04 ± 0.06	0.93 ± 0.01	0.16 ± 0.01	33.63 ± 0.02	C0
2017ckq	851.31 ± 0.05	0.96 ± 0.01	14.38 ± 0.01	⋯	14.33 ± 0.01	14.42 ± 0.01	14.93 ± 0.01	851.24 ± 0.07	0.95 ± 0.01	0.02 ± 0.01	33.31 ± 0.01	C0
2017cjr	847.36 ± 0.08	0.91 ± 0.01	15.08 ± 0.01	⋯	15.06 ± 0.01	15.11 ± 0.01	15.62 ± 0.02	847.34 ± 0.08	0.91 ± 0.01	0.02 ± 0.01	34.00 ± 0.02	C0
2017cts	856.80 ± 0.13	0.95 ± 0.01	15.81 ± 0.02	⋯	15.72 ± 0.01	15.81 ± 0.01	16.35 ± 0.01	856.77 ± 0.13	0.94 ± 0.01	0.07 ± 0.01	34.73 ± 0.02	C0
2017kdz	846.93 ± 0.50	0.53 ± 0.06	17.03 ± 0.11	⋯	16.49 ± 0.06	16.46 ± 0.07	16.61 ± 0.12	846.66 ± 0.50	0.54 ± 0.06	0.08 ± 0.05	34.24 ± 0.22	C0
2017cze	857.02 ± 0.21	0.53 ± 0.02	16.08 ± 0.03	⋯	15.77 ± 0.02	15.86 ± 0.02	16.25 ± 0.03	856.85 ± 0.39	0.51 ± 0.04	−0.16 ± 0.07	34.25 ± 0.06	C0
2017cyy	870.87 ± 0.05	0.98 ± 0.01	14.95 ± 0.01	⋯	14.74 ± 0.01	14.77 ± 0.01	15.25 ± 0.01	870.85 ± 0.07	0.98 ± 0.01	−0.01 ± 0.01	33.38 ± 0.02	C0

Table 4
(Continued)

	max_model							*EBV_model2*				
SN[a]	$t_{peak}(B)$	s_{BV}	B_{peak}	g_{peak}	V_{peak}	r_{peak}	i_{peak}	$t_{peak}(B)$	s_{BV}	E $(B-V)_{host}$	μ	Category[c]
2017daf	860.77 ± 0.42	0.77 ± 0.02	15.89 ± 0.03	⋯	15.79 ± 0.02	15.86 ± 0.02	16.40 ± 0.03	860.56 ± 0.39	0.78 ± 0.02	0.03 ± 0.02	34.68 ± 0.03	C0
2017dei	869.26 ± 0.15	0.70 ± 0.01	16.72 ± 0.02	⋯	16.38 ± 0.02	16.35 ± 0.01	16.74 ± 0.02	869.23 ± 0.15	0.71 ± 0.01	0.17 ± 0.02	34.67 ± 0.02	C0
2017dhr	870.46 ± 0.69	1.10 ± 0.08	17.58 ± 0.12	⋯	16.20 ± 0.03	15.67 ± 0.06	15.52 ± 0.09	870.53 ± 0.59	1.08 ± 0.05	1.47 ± 0.04	32.51 ± 0.08	C0
2017dit	881.50 ± 0.12	0.88 ± 0.01	15.98 ± 0.02	⋯	15.85 ± 0.02	15.85 ± 0.02	16.53 ± 0.02	881.56 ± 0.17	0.88 ± 0.02	0.10 ± 0.02	34.77 ± 0.04	C0
2017dps	882.44 ± 0.09	0.75 ± 0.01	14.85 ± 0.01	⋯	14.77 ± 0.01	14.87 ± 0.01	15.38 ± 0.01	882.42 ± 0.09	0.75 ± 0.01	−0.05 ± 0.01	33.65 ± 0.02	C0
2017drh	891.00 ± 0.10	0.88 ± 0.01	17.10 ± 0.02	⋯	15.71 ± 0.02	15.13 ± 0.01	14.93 ± 0.02	890.95 ± 0.10	0.88 ± 0.01	1.46 ± 0.02	31.79 ± 0.03	C0
2017dzs	860.51 ± 6.07	0.93 ± 0.24	15.38 ± 0.15	⋯	15.33 ± 0.18	15.53 ± 0.25	16.10 ± 0.28	855.40 ± 6.20	1.18 ± 0.22	−0.17 ± 0.17	34.93 ± 0.42	C3
2017eck	899.86 ± 0.28	1.14 ± 0.03	16.43 ± 0.02	⋯	16.20 ± 0.01	16.23 ± 0.01	16.70 ± 0.01	899.61 ± 0.19	1.18 ± 0.02	−0.0 ± 0.02	34.95 ± 0.03	C0
2017ebm	887.23 ± 1.23	0.39 ± 0.05	18.38 ± 0.15	⋯	17.42 ± 0.10	17.44 ± 0.07	17.44 ± 0.10	886.84 ± 1.28	0.41 ± 0.04	0.24 ± 0.08	34.79 ± 0.09	C0
2017edu	856.31 ± 1.47	0.77 ± 0.45	⋯	⋯	16.87 ± 0.18	⋯	⋯	⋯	⋯	⋯	⋯	C1
2017egb	906.48 ± 0.11	0.80 ± 0.01	15.79 ± 0.02	⋯	15.68 ± 0.01	15.70 ± 0.01	16.14 ± 0.02	906.50 ± 0.11	0.80 ± 0.01	0.09 ± 0.02	34.37 ± 0.02	C0
2017ejb	911.40 ± 0.07	0.47 ± 0.01	15.88 ± 0.02	⋯	15.37 ± 0.01	15.32 ± 0.01	15.57 ± 0.02	911.39 ± 0.09	0.47 ± 0.01	0.05 ± 0.02	33.18 ± 0.03	C0
2017ejw	912.17 ± 0.11	0.85 ± 0.01	15.54 ± 0.02	⋯	15.53 ± 0.01	15.63 ± 0.01	16.19 ± 0.02	912.16 ± 0.11	0.84 ± 0.01	−0.03 ± 0.01	34.59 ± 0.02	C0
2017ekr	913.88 ± 0.14	0.83 ± 0.01	16.10 ± 0.03	⋯	15.95 ± 0.02	15.98 ± 0.02	16.52 ± 0.02	913.83 ± 0.14	0.83 ± 0.01	0.02 ± 0.02	34.73 ± 0.03	C0
2017emq	917.27 ± 0.08	0.85 ± 0.01	14.39 ± 0.01	⋯	14.13 ± 0.01	14.14 ± 0.02	14.68 ± 0.02	917.35 ± 0.11	0.84 ± 0.02	0.23 ± 0.02	32.78 ± 0.04	C0
2017enx	918.42 ± 0.33	0.70 ± 0.02	14.09 ± 0.03	⋯	13.82 ± 0.02	13.80 ± 0.02	14.16 ± 0.02	918.33 ± 0.29	0.70 ± 0.02	0.01 ± 0.03	32.08 ± 0.03	C0
2017erv	924.79 ± 0.25	1.13 ± 0.04	16.02 ± 0.03	⋯	15.69 ± 0.02	15.74 ± 0.03	16.33 ± 0.02	923.72 ± 0.39	1.26 ± 0.03	0.01 ± 0.03	34.67 ± 0.04	C0
2017erp	935.24 ± 0.08	1.03 ± 0.01	13.77 ± 0.01	⋯	13.49 ± 0.01	13.51 ± 0.01	14.00 ± 0.04	935.17 ± 0.09	1.03 ± 0.01	0.19 ± 0.01	32.16 ± 0.02	C0
2017ezd	941.78 ± 0.11	0.89 ± 0.01	15.83 ± 0.02	⋯	15.73 ± 0.02	15.76 ± 0.02	16.13 ± 0.02	941.87 ± 0.16	0.88 ± 0.02	0.13 ± 0.03	34.34 ± 0.04	C0
2017evn	935.14 ± 0.14	1.08 ± 0.03	15.46 ± 0.02	⋯	15.34 ± 0.02	15.48 ± 0.02	16.09 ± 0.03	935.25 ± 0.16	1.09 ± 0.03	0.04 ± 0.02	34.55 ± 0.05	C0
2017exo	936.88 ± 0.11	1.10 ± 0.02	16.70 ± 0.01	⋯	16.25 ± 0.01	16.18 ± 0.01	16.60 ± 0.01	936.80 ± 0.13	1.11 ± 0.02	0.13 ± 0.01	34.49 ± 0.03	C0
2017fbj	944.46 ± 0.19	0.91 ± 0.03	16.20 ± 0.03	⋯	15.92 ± 0.03	16.00 ± 0.05	16.57 ± 0.07	944.44 ± 0.24	0.91 ± 0.03	0.07 ± 0.03	34.53 ± 0.10	C0
2017ffv	956.99 ± 0.09	0.94 ± 0.01	15.58 ± 0.02	⋯	15.23 ± 0.02	15.21 ± 0.01	15.67 ± 0.03	956.96 ± 0.10	0.94 ± 0.01	0.29 ± 0.02	33.72 ± 0.03	C0
2017fgc	961.00 ± 0.15	1.08 ± 0.01	13.84 ± 0.01	14.11 ± 0.04	13.57 ± 0.01	13.63 ± 0.01	14.26 ± 0.01	959.97 ± 0.12	1.19 ± 0.02	0.15 ± 0.02	32.57 ± 0.03	C0
2017fvl	971.65 ± 0.84	0.88 ± 0.04	16.49 ± 0.06	⋯	15.99 ± 0.04	15.87 ± 0.04	16.17 ± 0.07	971.26 ± 0.47	0.88 ± 0.03	0.07 ± 0.02	33.73 ± 0.03	C0
2017fzy	979.69 ± 0.12	0.61 ± 0.01	16.42 ± 0.02	⋯	15.89 ± 0.01	15.84 ± 0.01	16.14 ± 0.02	979.53 ± 0.18	0.62 ± 0.02	0.20 ± 0.03	33.83 ± 0.03	C0
2017fzw	988.89 ± 0.06	0.62 ± 0.01	14.24 ± 0.01	⋯	13.78 ± 0.01	13.74 ± 0.01	14.22 ± 0.02	988.95 ± 0.08	0.60 ± 0.01	0.19 ± 0.02	31.95 ± 0.03	C0
2017gah	985.66 ± 0.13	0.62 ± 0.01	15.00 ± 0.01	15.07 ± 0.05	14.56 ± 0.01	14.48 ± 0.01	14.89 ± 0.02	985.66 ± 0.07	0.63 ± 0.01	0.23 ± 0.02	32.69 ± 0.02	C0
2017ghu	984.92 ± 0.65	0.93 ± 0.02	17.79 ± 0.07	⋯	16.99 ± 0.05	16.74 ± 0.05	17.04 ± 0.06	982.61 ± 1.00	1.18 ± 0.05	0.15 ± 0.05	34.68 ± 0.07	C0
2017gjn	1004.38 ± 0.19	0.99 ± 0.01	15.17 ± 0.01	15.17 ± 0.03	15.05 ± 0.01	15.14 ± 0.01	15.63 ± 0.01	1004.28 ± 0.12	0.99 ± 0.01	−0.03 ± 0.01	33.91 ± 0.02	C0
2017glq	1016.13 ± 0.06	0.91 ± 0.01	14.32 ± 0.01	14.39 ± 0.01	14.25 ± 0.01	14.34 ± 0.01	14.82 ± 0.01	1016.00 ± 0.05	0.92 ± 0.01	0.06 ± 0.01	33.21 ± 0.01	C0
2017glx	1009.96 ± 0.61	1.09 ± 0.02	14.70 ± 0.02	14.85 ± 0.04	14.51 ± 0.01	14.56 ± 0.02	15.05 ± 0.03	1009.92 ± 0.12	1.09 ± 0.02	0.09 ± 0.01	33.34 ± 0.03	C0
2017grw	1017.93 ± 0.11	0.75 ± 0.01	15.53 ± 0.02	⋯	15.46 ± 0.01	15.47 ± 0.01	15.95 ± 0.02	1017.94 ± 0.12	0.76 ± 0.01	0.03 ± 0.02	34.20 ± 0.02	C0
2017guu	1026.69 ± 0.36	1.13 ± 0.07	17.03 ± 0.09	17.16 ± 0.06	16.60 ± 0.03	16.60 ± 0.06	17.02 ± 0.05	1024.83 ± 1.24	1.26 ± 0.05	−0.38 ± 0.06	34.93 ± 0.09	C0
2017gxq	1029.69 ± 0.22	1.00 ± 0.02	14.11 ± 0.06	14.36 ± 0.10	14.05 ± 0.04	14.20 ± 0.03	14.72 ± 0.06	1029.72 ± 0.20	0.99 ± 0.01	0.05 ± 0.01	33.19 ± 0.02	C0
2017gup	1021.58 ± 1.61	1.42 ± 0.09	17.31 ± 0.10	17.76 ± 0.11	16.86 ± 0.07	16.90 ± 0.05	17.13 ± 0.08	1021.57 ± 1.50	1.43 ± 0.06	−0.21 ± 0.09	35.17 ± 0.07	C0
2017guh	1022.37 ± 0.16	0.87 ± 0.01	15.23 ± 0.03	15.27 ± 0.03	15.12 ± 0.02	15.18 ± 0.02	15.65 ± 0.03	1022.11 ± 0.23	0.89 ± 0.02	0.13 ± 0.02	33.96 ± 0.04	C0
2017haf	1034.64 ± 0.12	0.92 ± 0.01	15.48 ± 0.01	15.55 ± 0.02	15.34 ± 0.01	15.40 ± 0.01	16.01 ± 0.02	1034.50 ± 0.15	0.92 ± 0.01	0.09 ± 0.01	34.28 ± 0.02	C0
2017hgz	1044.80 ± 0.10	0.82 ± 0.01	15.26 ± 0.02	15.31 ± 0.02	15.13 ± 0.01	15.17 ± 0.01	15.66 ± 0.02	1044.76 ± 0.12	0.83 ± 0.01	0.11 ± 0.02	33.92 ± 0.02	C0
2017hjw	1056.23 ± 0.07	1.02 ± 0.01	16.25 ± 0.01	16.26 ± 0.02	15.90 ± 0.01	15.87 ± 0.01	16.32 ± 0.01	1056.15 ± 0.08	1.03 ± 0.01	0.23 ± 0.01	34.40 ± 0.02	C0
2017hjy	1056.16 ± 0.12	0.96 ± 0.01	15.59 ± 0.02	15.72 ± 0.02	15.40 ± 0.01	15.45 ± 0.01	16.01 ± 0.02	1056.19 ± 0.14	0.97 ± 0.01	0.11 ± 0.01	34.24 ± 0.03	C0
2017hle	1050.64 ± 0.11	0.39 ± 0.01	17.89 ± 0.02	17.63 ± 0.04	16.97 ± 0.02	16.86 ± 0.02	16.96 ± 0.02	1050.55 ± 0.15	0.36 ± 0.01	0.20 ± 0.03	34.21 ± 0.05	C0
2017hoq	1061.86 ± 0.13	1.06 ± 0.02	16.04 ± 0.02	16.10 ± 0.01	15.93 ± 0.01	16.05 ± 0.02	16.70 ± 0.02	1061.55 ± 0.28	1.09 ± 0.03	−0.03 ± 0.02	35.15 ± 0.04	C0
2017hou	1056.19 ± 0.22	1.07 ± 0.03	18.23 ± 0.02	18.00 ± 0.07	17.46 ± 0.01	17.21 ± 0.01	17.46 ± 0.02	1056.06 ± 0.27	1.12 ± 0.03	0.69 ± 0.02	35.11 ± 0.04	C0
2017hpa	1066.76 ± 0.09	1.01 ± 0.01	15.60 ± 0.02	15.61 ± 0.05	15.37 ± 0.01	15.38 ± 0.01	15.85 ± 0.02	1066.73 ± 0.08	1.01 ± 0.01	0.09 ± 0.01	33.99 ± 0.02	C0
2017igf	1085.38 ± 0.51	0.57 ± 0.01	14.89 ± 0.01	14.67 ± 0.04	14.59 ± 0.01	14.50 ± 0.01	14.87 ± 0.01	1085.40 ± 0.06	0.58 ± 0.01	0.11 ± 0.02	32.76 ± 0.02	C0

Table 4
(Continued)

	max_model							*EBV_model2*				
SN[a]	$t_{peak}(B)$	s_{BV}	B_{peak}	g_{peak}	V_{peak}	r_{peak}	i_{peak}	$t_{peak}(B)$	s_{BV}	E $(B-V)_{host}$	μ	Category[c]
2017iji	1082.15 ± 0.81	0.92 ± 0.01	15.19 ± 0.02	15.29 ± 0.05	14.93 ± 0.02	15.02 ± 0.02	15.57 ± 0.03	1078.97 ± 0.46	1.10 ± 0.03	0.14 ± 0.02	34.00 ± 0.04	C0
2017isj	1094.31 ± 0.17	1.07 ± 0.02	15.88 ± 0.02	16.21 ± 0.03	15.63 ± 0.01	15.77 ± 0.02	16.39 ± 0.02	1092.62 ± 0.39	1.19 ± 0.02	0.01 ± 0.02	34.79 ± 0.04	C0
2017isq	1048.68 ± 1.01	1.19 ± 0.02	13.92 ± 0.03	14.44 ± 0.04	13.75 ± 0.03	13.80 ± 0.03	14.40 ± 0.07	1047.89 ± 0.97	1.47 ± 0.03	−0.40 ± 0.04	33.61 ± 0.04	C3
2017izu	1116.78 ± 0.30	0.91 ± 0.02	15.05 ± 0.06	15.11 ± 0.02	14.84 ± 0.05	14.89 ± 0.04	15.40 ± 0.08	1116.20 ± 0.27	0.94 ± 0.01	0.14 ± 0.01	33.58 ± 0.02	C0
2017iyb	1118.01 ± 0.09	0.82 ± 0.01	14.95 ± 0.01	14.96 ± 0.01	14.77 ± 0.01	14.85 ± 0.01	15.43 ± 0.02	1117.44 ± 0.15	0.86 ± 0.01	0.12 ± 0.01	33.63 ± 0.02	C0
2017iyw	1107.88 ± 0.13	0.92 ± 0.01	15.74 ± 0.02	15.73 ± 0.02	15.60 ± 0.01	15.64 ± 0.01	16.16 ± 0.01	1107.99 ± 0.17	0.91 ± 0.01	0.14 ± 0.01	34.46 ± 0.02	C0
2017jav	1118.42 ± 0.53	0.64 ± 0.01	16.02 ± 0.01	15.87 ± 0.10	15.80 ± 0.01	15.86 ± 0.01	16.22 ± 0.01	1118.34 ± 0.08	0.64 ± 0.01	0.01 ± 0.02	34.30 ± 0.02	C0
2017jdx	1119.57 ± 0.16	0.95 ± 0.01	15.95 ± 0.02	15.92 ± 0.02	15.81 ± 0.01	15.98 ± 0.02	16.53 ± 0.02	1119.30 ± 0.25	0.97 ± 0.02	0.05 ± 0.02	34.89 ± 0.04	C0
2018gl	1138.94 ± 0.04	0.64 ± 0.01	16.32 ± 0.01	16.39 ± 0.02	16.14 ± 0.01	16.23 ± 0.01	16.60 ± 0.01	1138.95 ± 0.04	0.64 ± 0.01	−0.01 ± 0.01	34.73 ± 0.01	C0
2018gv	1150.38 ± 0.04	1.04 ± 0.01	12.92 ± 0.01	…	12.89 ± 0.01	13.01 ± 0.01	13.58 ± 0.01	1150.37 ± 0.04	1.04 ± 0.01	−0.01 ± 0.01	32.07 ± 0.01	C0
2018kp	1160.40 ± 0.08	0.95 ± 0.01	16.73 ± 0.02	16.55 ± 0.02	16.05 ± 0.01	15.84 ± 0.01	16.18 ± 0.01	1160.42 ± 0.10	0.94 ± 0.01	0.68 ± 0.01	33.90 ± 0.02	C0
2018pv	1164.77 ± 0.05	0.51 ± 0.01	13.28 ± 0.02	12.99 ± 0.01	12.65 ± 0.02	12.55 ± 0.02	12.90 ± 0.02	1164.58 ± 0.15	0.52 ± 0.02	0.26 ± 0.04	30.49 ± 0.05	C0
2018pc	1165.23 ± 0.05	0.85 ± 0.01	15.44 ± 0.02	15.34 ± 0.01	15.05 ± 0.01	14.98 ± 0.01	15.28 ± 0.01	1165.22 ± 0.06	0.86 ± 0.01	0.44 ± 0.01	33.31 ± 0.02	C0
2018oh	1163.33 ± 0.05	1.01 ± 0.01	14.31 ± 0.01	14.43 ± 0.01	14.31 ± 0.01	14.46 ± 0.01	15.02 ± 0.01	1163.24 ± 0.05	1.03 ± 0.01	−0.03 ± 0.01	33.57 ± 0.01	C0
2018vw	1178.03 ± 0.12	1.13 ± 0.02	15.39 ± 0.01	15.48 ± 0.02	15.42 ± 0.01	15.64 ± 0.02	16.27 ± 0.02	1178.14 ± 0.13	1.13 ± 0.02	−0.11 ± 0.01	34.93 ± 0.03	C0
2018xx	1184.91 ± 0.07	0.80 ± 0.01	14.51 ± 0.02	14.58 ± 0.01	14.43 ± 0.02	14.50 ± 0.02	15.00 ± 0.02	1184.83 ± 0.06	0.81 ± 0.01	−0.03 ± 0.01	33.25 ± 0.02	C0
2018yu	1195.24 ± 0.04	0.98 ± 0.01	14.02 ± 0.01	14.06 ± 0.01	13.95 ± 0.01	14.05 ± 0.02	14.50 ± 0.01	1195.06 ± 0.05	0.99 ± 0.01	−0.02 ± 0.01	32.85 ± 0.01	C0
2018zz	1190.72 ± 0.07	0.65 ± 0.01	15.15 ± 0.02	14.99 ± 0.01	14.95 ± 0.01	14.98 ± 0.01	15.39 ± 0.02	1190.83 ± 0.08	0.64 ± 0.01	−0.0 ± 0.02	33.44 ± 0.02	C0
2018apo	1223.02 ± 0.14	1.09 ± 0.03	15.52 ± 0.03	15.54 ± 0.01	15.27 ± 0.03	15.34 ± 0.03	15.75 ± 0.03	1223.08 ± 0.15	1.20 ± 0.03	0.12 ± 0.02	34.11 ± 0.04	C0
2018aoz	1222.91 ± 0.03	0.83 ± 0.01	12.90 ± 0.01	12.93 ± 0.01	12.87 ± 0.01	12.97 ± 0.01	13.55 ± 0.02	1222.94 ± 0.05	0.82 ± 0.01	−0.09 ± 0.01	31.87 ± 0.02	C0
2018aqi	1223.06 ± 0.11	0.78 ± 0.01	15.77 ± 0.03	15.72 ± 0.02	15.53 ± 0.02	15.57 ± 0.02	16.08 ± 0.04	1223.06 ± 0.12	0.80 ± 0.01	0.12 ± 0.02	34.17 ± 0.03	C0
2018ast	1214.52 ± 0.75	0.38 ± 0.02	17.36 ± 0.08	17.17 ± 0.07	16.33 ± 0.06	16.43 ± 0.05	16.41 ± 0.07	1214.82 ± 0.53	0.40 ± 0.02	0.21 ± 0.04	34.00 ± 0.06	C0
2018aye	1243.85 ± 0.01	1.06 ± 0.01	15.76 ± 0.01	15.90 ± 0.01	15.72 ± 0.01	15.88 ± 0.01	16.49 ± 0.01	1243.74 ± 0.09	1.07 ± 0.01	−0.04 ± 0.01	35.03 ± 0.02	C0
2018big	1265.40 ± 0.08	1.11 ± 0.02	15.98 ± 0.01	15.95 ± 0.02	15.79 ± 0.01	15.83 ± 0.01	16.39 ± 0.01	1265.28 ± 0.09	1.14 ± 0.02	0.15 ± 0.01	34.77 ± 0.02	C0
2018brz	1259.95 ± 0.36	1.08 ± 0.06	16.50 ± 0.05	16.37 ± 0.04	16.14 ± 0.07	16.14 ± 0.05	16.60 ± 0.09	1257.68 ± 0.98	1.26 ± 0.04	0.03 ± 0.05	34.98 ± 0.05	C0
2018bta	1267.66 ± 0.32	0.95 ± 0.01	15.79 ± 0.02	16.13 ± 0.13	15.43 ± 0.02	15.39 ± 0.02	15.72 ± 0.02	1267.55 ± 0.29	0.94 ± 0.02	0.30 ± 0.02	33.69 ± 0.04	C0
2018cnj	1277.96 ± 0.75	0.90 ± 0.02	17.78 ± 0.07	17.46 ± 0.14	17.16 ± 0.05	16.85 ± 0.03	16.93 ± 0.06	1277.95 ± 0.32	0.90 ± 0.01	0.45 ± 0.02	34.30 ± 0.02	C0
2018chl	1272.67 ± 0.98	0.25 ± 0.03	18.01 ± 0.16	17.36 ± 0.11	17.06 ± 0.09	17.12 ± 0.04	17.14 ± 0.08	1273.49 ± 0.64	0.27 ± 0.04	−0.01 ± 0.16	34.31 ± 0.07	C0
2018cqj	1294.53 ± 0.28	0.62 ± 0.05	16.54 ± 0.07	16.53 ± 0.05	16.16 ± 0.05	16.13 ± 0.04	16.56 ± 0.09	1294.22 ± 0.37	0.66 ± 0.03	0.20 ± 0.05	34.42 ± 0.04	C0
2018cqw	1301.01 ± 0.04	0.96 ± 0.01	14.57 ± 0.01	14.56 ± 0.01	14.40 ± 0.01	14.46 ± 0.01	14.96 ± 0.01	1301.00 ± 0.04	0.96 ± 0.01	0.03 ± 0.01	33.21 ± 0.01	C0
2018ctv	1294.41 ± 0.14	0.44 ± 0.01	17.45 ± 0.02	17.06 ± 0.05	16.67 ± 0.02	16.68 ± 0.02	16.85 ± 0.02	1294.31 ± 0.18	0.44 ± 0.02	0.20 ± 0.03	34.34 ± 0.04	C0
2018cuh	1305.29 ± 0.08	0.93 ± 0.01	15.06 ± 0.01	15.12 ± 0.01	15.03 ± 0.01	15.13 ± 0.01	15.71 ± 0.02	1305.24 ± 0.11	0.93 ± 0.01	−0.04 ± 0.01	34.09 ± 0.02	C0
2018cuw	1305.15 ± 2.29	1.35 ± 0.24	…	16.54 ± 0.08	16.55 ± 0.06	…	…	…	…	…	…	C1
2018dda	1313.75 ± 0.14	1.01 ± 0.02	15.59 ± 0.03	15.73 ± 0.02	15.22 ± 0.02	15.30 ± 0.02	15.71 ± 0.03	1313.03 ± 0.17	1.07 ± 0.02	0.27 ± 0.02	34.00 ± 0.03	C0
2018eay	1328.67 ± 0.11	1.17 ± 0.02	17.51 ± 0.01	17.11 ± 0.09	16.67 ± 0.01	16.51 ± 0.01	16.62 ± 0.01	1328.72 ± 0.15	1.13 ± 0.02	0.80 ± 0.02	34.34 ± 0.03	C0
2018ebk	1330.24 ± 0.07	0.91 ± 0.01	16.92 ± 0.01	16.36 ± 0.03	16.26 ± 0.01	16.08 ± 0.01	16.32 ± 0.01	1330.25 ± 0.05	0.90 ± 0.01	0.25 ± 0.01	33.79 ± 0.01	C0
2018enc	1345.05 ± 0.12	1.11 ± 0.03	16.07 ± 0.02	16.04 ± 0.03	15.95 ± 0.02	16.05 ± 0.02	16.67 ± 0.02	1344.89 ± 0.15	1.14 ± 0.03	−0.05 ± 0.02	35.08 ± 0.04	C0
2018eov	1341.00 ± 0.18	1.19 ± 0.02	15.68 ± 0.02	16.00 ± 0.03	15.42 ± 0.02	15.47 ± 0.02	15.93 ± 0.02	1340.97 ± 0.19	1.19 ± 0.02	0.01 ± 0.02	34.16 ± 0.03	C0
2018eqq	1339.71 ± 0.19	1.06 ± 0.01	15.49 ± 0.02	15.58 ± 0.03	15.30 ± 0.01	15.40 ± 0.01	15.94 ± 0.01	1339.48 ± 0.23	1.08 ± 0.02	−0.0 ± 0.01	34.26 ± 0.02	C0
2018feb	1363.01 ± 0.04	0.96 ± 0.01	15.31 ± 0.01	15.39 ± 0.01	15.21 ± 0.01	15.28 ± 0.01	15.82 ± 0.01	1363.02 ± 0.04	0.96 ± 0.01	0.07 ± 0.01	34.16 ± 0.01	C0
2018fhw	1357.95 ± 0.08	0.52 ± 0.01	16.70 ± 0.01	16.68 ± 0.06	16.36 ± 0.01	16.31 ± 0.01	16.65 ± 0.01	1357.93 ± 0.08	0.51 ± 0.01	0.04 ± 0.02	34.50 ± 0.02	C0
2018fop	1366.21 ± 0.23	1.06 ± 0.02	15.61 ± 0.03	15.73 ± 0.02	15.54 ± 0.02	15.65 ± 0.02	16.28 ± 0.03	1365.77 ± 0.05	1.13 ± 0.02	−0.04 ± 0.02	34.79 ± 0.03	C0
2018fpm	1356.36 ± 0.32	0.95 ± 0.03	17.81 ± 0.09	17.02 ± 0.04	16.40 ± 0.05	15.91 ± 0.04	15.83 ± 0.07	1355.18 ± 0.36	0.96 ± 0.01	1.41 ± 0.02	32.88 ± 0.03	C0
2018fnq	1372.94 ± 0.18	1.10 ± 0.03	15.78 ± 0.03	15.88 ± 0.02	15.68 ± 0.02	15.80 ± 0.02	16.31 ± 0.03	1373.62 ± 0.19	1.08 ± 0.02	0.07 ± 0.01	34.77 ± 0.03	C0
2018fuk	1377.41 ± 0.13	0.92 ± 0.01	15.91 ± 0.01	15.92 ± 0.02	15.71 ± 0.01	15.72 ± 0.01	16.23 ± 0.02	1377.39 ± 0.14	0.92 ± 0.01	0.13 ± 0.01	34.40 ± 0.02	C0
2018ghb	1382.68 ± 0.12	0.62 ± 0.01	14.83 ± 0.02	14.72 ± 0.02	14.44 ± 0.02	14.46 ± 0.02	14.81 ± 0.02	1382.69 ± 0.11	0.65 ± 0.01	0.09 ± 0.01	32.64 ± 0.02	C0

Table 4
(Continued)

	max_model							*EBV_model2*				
SN[a]	$t_{\rm peak}(B)$	s_{BV}	$B_{\rm peak}$	$g_{\rm peak}$	$V_{\rm peak}$	$r_{\rm peak}$	$i_{\rm peak}$	$t_{\rm peak}(B)$	s_{BV}	E $(B-V)_{\rm host}$	μ	Category[c]
2018htw	1416.60 ± 0.53	0.89 ± 0.04	16.03 ± 0.26	16.05 ± 0.04	15.85 ± 0.04	15.76 ± 0.19	16.35 ± 0.13	1416.38 ± 0.55	0.88 ± 0.03	0.20 ± 0.06	34.29 ± 0.17	C3
2018hib	1415.33 ± 0.07	0.89 ± 0.01	15.27 ± 0.01	15.31 ± 0.01	15.19 ± 0.01	15.26 ± 0.01	15.67 ± 0.02	1415.31 ± 0.12	0.90 ± 0.01	0.12 ± 0.01	34.09 ± 0.03	C0
2018hkq	1414.24 ± 0.39	0.91 ± 0.03	15.67 ± 0.08	15.56 ± 0.03	15.36 ± 0.06	15.40 ± 0.06	16.26 ± 0.09	1412.89 ± 0.59	1.14 ± 0.12	0.02 ± 0.08	34.82 ± 0.18	C0
2018hme	1413.61 ± 0.41	0.77 ± 0.03	15.90 ± 0.09	15.85 ± 0.02	15.52 ± 0.05	15.57 ± 0.04	15.99 ± 0.09	1413.54 ± 0.81	0.76 ± 0.02	0.13 ± 0.03	34.00 ± 0.05	C0
2018htt	1439.63 ± 0.08	0.73 ± 0.01	14.01 ± 0.02	13.98 ± 0.01	13.96 ± 0.02	14.10 ± 0.02	14.62 ± 0.02	1439.28 ± 0.14	0.73 ± 0.01	−0.10 ± 0.03	32.96 ± 0.03	C0
2018hrt	1431.88 ± 0.24	0.88 ± 0.01	18.20 ± 0.07	17.87 ± 0.09	17.28 ± 0.02	16.88 ± 0.02	16.98 ± 0.02	1431.81 ± 0.24	0.88 ± 0.01	0.88 ± 0.03	34.27 ± 0.04	C0
2018hsa	1432.18 ± 0.12	0.97 ± 0.01	15.82 ± 0.02	15.79 ± 0.01	15.60 ± 0.01	15.63 ± 0.02	16.06 ± 0.03	1432.17 ± 0.22	0.97 ± 0.02	0.23 ± 0.01	34.30 ± 0.03	C0
2018ilu	1450.35 ± 0.16	1.09 ± 0.02	15.48 ± 0.01	15.46 ± 0.01	15.35 ± 0.01	15.48 ± 0.01	16.10 ± 0.01	1449.71 ± 0.18	1.13 ± 0.02	−0.01 ± 0.01	34.56 ± 0.02	C0
2018imd	1405.57 ± 0.89	1.19 ± 0.05	13.84 ± 0.05	⋯	13.91 ± 0.05	14.61 ± 0.05	14.52 ± 0.11	1405.00 ± 0.00	0.90 ± 0.07	−0.07 ± 0.04	32.82 ± 0.24	C3
2018isq	1449.62 ± 0.57	0.42 ± 0.01	16.93 ± 0.02	16.53 ± 0.07	15.94 ± 0.01	15.84 ± 0.02	15.97 ± 0.02	1449.80 ± 0.17	0.39 ± 0.02	0.16 ± 0.04	33.02 ± 0.04	C0
2018iuu	1459.32 ± 0.09	0.94 ± 0.01	15.50 ± 0.01	15.40 ± 0.02	15.39 ± 0.01	15.53 ± 0.01	16.12 ± 0.02	1459.14 ± 0.11	0.95 ± 0.01	0.05 ± 0.01	34.52 ± 0.02	C0
2018jaj	1463.13 ± 0.55	1.07 ± 0.01	15.53 ± 0.01	15.53 ± 0.04	15.44 ± 0.01	15.56 ± 0.01	16.26 ± 0.01	1463.05 ± 0.12	1.09 ± 0.02	0.01 ± 0.01	34.73 ± 0.03	C0
2018jeo	1455.03 ± 0.15	1.04 ± 0.01	16.13 ± 0.01	16.10 ± 0.01	15.91 ± 0.01	15.95 ± 0.01	16.41 ± 0.01	1454.86 ± 0.15	1.05 ± 0.01	0.04 ± 0.01	34.60 ± 0.02	C0
2018jjd	1470.29 ± 0.15	1.15 ± 0.03	15.79 ± 0.03	15.78 ± 0.02	15.84 ± 0.02	15.97 ± 0.02	16.59 ± 0.02	1470.34 ± 0.11	1.14 ± 0.02	−0.09 ± 0.01	35.24 ± 0.02	C0
2018jky	1469.66 ± 0.05	0.71 ± 0.01	15.47 ± 0.02	15.57 ± 0.01	15.33 ± 0.01	15.38 ± 0.01	15.80 ± 0.02	1469.72 ± 0.04	0.71 ± 0.01	0.03 ± 0.01	34.00 ± 0.02	C0
2018jmo	1474.05 ± 0.03	0.78 ± 0.01	16.89 ± 0.02	16.83 ± 0.04	16.51 ± 0.02	16.51 ± 0.01	16.97 ± 0.02	1473.58 ± 0.35	0.79 ± 0.02	0.19 ± 0.02	34.91 ± 0.03	C0
2018jov	1475.38 ± 0.05	1.00 ± 0.01	16.26 ± 0.01	16.26 ± 0.03	16.06 ± 0.01	16.09 ± 0.01	16.62 ± 0.01	1475.39 ± 0.06	1.01 ± 0.01	0.17 ± 0.01	34.88 ± 0.02	C0
2018jwi	1479.57 ± 0.07	0.93 ± 0.01	15.07 ± 0.01	15.11 ± 0.01	15.02 ± 0.01	15.09 ± 0.01	15.59 ± 0.02	1479.60 ± 0.07	0.94 ± 0.01	0.03 ± 0.01	33.99 ± 0.01	C0
2018kmu	1481.73 ± 0.29	1.27 ± 0.02	16.46 ± 0.03	16.34 ± 0.03	16.34 ± 0.02	16.47 ± 0.02	17.18 ± 0.02	1481.36 ± 0.41	1.29 ± 0.03	−0.10 ± 0.02	35.78 ± 0.04	C0
2019np	1510.61 ± 0.03	0.99 ± 0.01	13.48 ± 0.01	13.45 ± 0.01	13.38 ± 0.01	13.49 ± 0.01	14.00 ± 0.01	1510.47 ± 0.05	1.00 ± 0.01	0.10 ± 0.01	32.44 ± 0.01	C0
2019so	1507.35 ± 0.07	0.41 ± 0.01	17.24 ± 0.02	16.80 ± 0.03	16.66 ± 0.01	16.63 ± 0.01	16.84 ± 0.03	1507.24 ± 0.08	0.43 ± 0.01	−0.01 ± 0.02	34.36 ± 0.03	C0
J140216[b]	1512.90 ± 0.15	1.21 ± 0.01	17.01 ± 0.01	16.90 ± 0.02	16.23 ± 0.01	16.05 ± 0.01	16.09 ± 0.01	1513.20 ± 0.15	1.13 ± 0.02	0.41 ± 0.01	33.52 ± 0.03	C0
2019gbx	1647.78 ± 0.05	0.83 ± 0.01	14.83 ± 0.01	14.92 ± 0.01	14.82 ± 0.01	14.94 ± 0.01	15.47 ± 0.01	1647.85 ± 0.05	0.82 ± 0.01	−0.07 ± 0.01	33.88 ± 0.02	C0
2019hxc	1663.67 ± 0.26	1.00 ± 0.02	16.77 ± 0.03	16.63 ± 0.04	16.44 ± 0.03	16.37 ± 0.02	16.95 ± 0.03	1662.40 ± 0.28	1.19 ± 0.03	0.26 ± 0.03	35.17 ± 0.05	C0
2019knt	1683.81 ± 0.12	1.07 ± 0.03	14.90 ± 0.03	14.93 ± 0.02	14.87 ± 0.02	14.97 ± 0.02	15.51 ± 0.03	1683.30 ± 0.06	1.14 ± 0.01	−0.02 ± 0.01	34.04 ± 0.02	C0
2019khf	1680.76 ± 0.11	1.00 ± 0.01	15.29 ± 0.02	15.32 ± 0.01	15.15 ± 0.02	15.19 ± 0.02	15.84 ± 0.03	1680.89 ± 0.12	1.02 ± 0.02	0.04 ± 0.02	34.12 ± 0.04	C0
2019ltt	1687.43 ± 0.24	1.16 ± 0.01	15.93 ± 0.02	⋯	15.66 ± 0.01	15.77 ± 0.01	16.25 ± 0.02	1687.59 ± 0.31	1.14 ± 0.02	0.02 ± 0.02	34.48 ± 0.03	C0
2019swh	1745.65 ± 0.25	0.87 ± 0.02	15.15 ± 0.05	15.33 ± 0.02	14.86 ± 0.04	14.87 ± 0.04	15.40 ± 0.06	1745.45 ± 0.32	0.89 ± 0.03	0.21 ± 0.04	33.19 ± 0.13	C0
2020ue	1873.75 ± 0.49	0.75 ± 0.01	12.21 ± 0.01	12.15 ± 0.03	12.18 ± 0.01	12.28 ± 0.01	12.75 ± 0.01	1873.73 ± 0.03	0.73 ± 0.01	−0.06 ± 0.01	31.09 ± 0.01	C0

Notes.

C0: Good data coverage and fitting results.

C1: Only ASAS-SN *V*-band data are available. SNooPy *EBV_model2* fitting is not feasible due to lack of multicolor coverage to derive host extinction. *max_model* fitting has been performed, yielding reasonable results of the peak times and magnitudes, although the derived s_{BV} should be used with caution.

C2: Only a small number ($\lesssim$3) of epochs with available multiband data. Some of the SNe only have multiband light curves close to the *B*-band peak, which makes it challenging to derive the decline rate (or the light-curve width). Similarly with C1, *max_model* fitting gives credible results of peak times and magnitudes, while the s_{BV} parameters should be used with caution. *EBV_model2* fitting is performed for these targets, but the fitting results have large uncertainties owing to inadequate coverage.

C3: The first available multiband data point obtained $\gtrsim$30 d after the estimated *B*-band peak. The light-curve parameters from both *max_model* and *EBV_model2* should be used with caution.

C4: Decent light-curve coverage, but poorly fit by SNooPy templates. Therefore, the best-fit parameters, especially those from *EBV_model2*, should not be trusted.

[a] The SN name adopts the IAU name when available, otherwise the survey name. All the IAU and survey names are available in Table 1.

[b] These names are used for brevity, the same as in Table 1.

[c] As explained below, the SNe are categorized into different groups according to their data coverage in terms of both wavelength and phase, and how well they are fitted by the template light curves.

(This table is available in machine-readable form.)

Table 5
Light-curve Parameters from Gaussian Process Fitting

SN[a]	$t_{\max}(B)$ −2,457,000	$B_{\rm peak}$ (mag)	$\Delta m_{15}(B)$ (mag)	$t_{\max}(V)$ −2,457,000	$V_{\rm peak}$ (mag)	$\Delta m_{15}(V)$ (mag)
ASASSN-15aj	⋯	⋯	⋯	37.9 ± 0.5	14.76 ± 0.02	0.93 ± 0.07
ASASSN-15db	⋯	⋯	⋯	77.0 ± 0.3	14.51 ± 0.02	0.83 ± 0.06
2015F	⋯	⋯	⋯	108.4 ± 0.6	13.33 ± 0.02	0.74 ± 0.04
2015bp	⋯	⋯	⋯	112.7 ± 0.3	13.90 ± 0.01	0.82 ± 0.03
ASASSN-15hf	⋯	⋯	⋯	138.9 ± 0.5	14.26 ± 0.02	0.68 ± 0.05
ASASSN-15hx	151.5 ± 0.2	13.29 ± 0.01	⋯	153.1 ± 0.5	13.37 ± 0.01	0.63 ± 0.04
ASASSN-15jo	169.0 ± 0.7	15.69 ± 0.02	1.87 ± 0.09	⋯	⋯	⋯
ASASSN-15kp	188.5 ± 1.2	15.52 ± 0.03	0.90 ± 0.13	188.9 ± 1.7	15.53 ± 0.05	0.51 ± 0.09
ASASSN-15pl	⋯	⋯	⋯	290.5 ± 0.9	15.16 ± 0.03	0.73 ± 0.06
ASASSN-15pz	307.2 ± 0.6	14.24 ± 0.02	0.67 ± 0.06	307.2 ± 0.6	14.26 ± 0.01	0.39 ± 0.04
ASASSN-15qc	299.4 ± 0.7	15.86 ± 0.02	1.01 ± 0.08	303.4 ± 0.5	15.60 ± 0.01	0.72 ± 0.03
2015ao	307.4 ± 0.6	17.52 ± 0.03	1.84 ± 0.16	310.2 ± 0.2	16.87 ± 0.02	1.49 ± 0.06
ASASSN-15rq	324.9 ± 0.3	15.45 ± 0.01	0.93 ± 0.05	326.1 ± 0.4	15.46 ± 0.01	0.61 ± 0.04
ASASSN-15rw	330.7 ± 0.8	15.65 ± 0.05	1.00 ± 0.14	332.0 ± 0.9	15.59 ± 0.04	0.62 ± 0.08
2015ar	351.1 ± 1.2	15.45 ± 0.04	1.25 ± 0.16	354.3 ± 0.6	15.28 ± 0.03	0.93 ± 0.07
PSN J21505094-7020289	360.4 ± 0.5	15.56 ± 0.03	1.39 ± 0.07	362.1 ± 0.4	15.17 ± 0.02	0.81 ± 0.03
ASASSN-15ti	365.2 ± 0.8	16.26 ± 0.06	1.53 ± 0.12	⋯	⋯	⋯
2015bd	⋯	⋯	⋯	348.5 ± 0.7	15.19 ± 0.02	0.65 ± 0.05
ASASSN-15uh	387.0 ± 1.4	15.57 ± 0.07	0.85 ± 0.19	389.3 ± 1.4	15.24 ± 0.06	0.57 ± 0.16
ASASSN-15ut	⋯	⋯	⋯	392.4 ± 0.5	16.32 ± 0.03	1.03 ± 0.17
2016bfu	471.0 ± 0.4	16.21 ± 0.03	1.91 ± 0.09	473.1 ± 0.4	15.63 ± 0.03	1.24 ± 0.04
2016blc	490.1 ± 0.9	14.71 ± 0.03	0.96 ± 0.10	491.0 ± 0.8	14.74 ± 0.03	0.64 ± 0.06
2016bln	⋯	⋯	⋯	502.0 ± 0.8	16.01 ± 0.04	0.67 ± 0.08
2016cbx	513.4 ± 1.3	16.69 ± 0.06	0.92 ± 0.19	516.1 ± 1.0	16.52 ± 0.06	0.74 ± 0.10
2016ccz	⋯	⋯	⋯	540.5 ± 0.5	15.44 ± 0.03	0.79 ± 0.07
2016coj	⋯	⋯	⋯	549.7 ± 0.3	13.01 ± 0.01	0.70 ± 0.02
2016daj	593.1 ± 1.0	16.58 ± 0.07	1.12 ± 0.14	593.6 ± 1.6	16.57 ± 0.05	0.67 ± 0.13
2016ekg	610.3 ± 0.3	15.03 ± 0.03	1.12 ± 0.07	611.3 ± 0.5	15.07 ± 0.02	0.66 ± 0.05
2016ekt	602.0 ± 1.2	14.77 ± 0.02	0.81 ± 0.11	605.0 ± 0.2	14.72 ± 0.01	0.66 ± 0.02
2016euj	619.7 ± 0.3	15.35 ± 0.02	1.39 ± 0.05	620.5 ± 0.3	15.33 ± 0.01	0.82 ± 0.03
2016fej	636.1 ± 0.4	13.90 ± 0.02	0.93 ± 0.06	638.0 ± 0.5	13.93 ± 0.02	0.62 ± 0.04
2016fff	630.3 ± 0.3	15.03 ± 0.02	1.77 ± 0.06	632.1 ± 0.3	14.90 ± 0.02	0.98 ± 0.05
2016fob	⋯	⋯	⋯	633.5 ± 1.3	16.15 ± 0.02	0.62 ± 0.07
2016gfk	⋯	⋯	⋯	646.9 ± 0.9	16.77 ± 0.03	0.84 ± 0.08
2016gsb	672.1 ± 0.5	14.52 ± 0.03	1.13 ± 0.08	674.4 ± 0.6	14.45 ± 0.03	0.66 ± 0.06
2016gsn	672.3 ± 0.5	15.25 ± 0.02	1.09 ± 0.06	672.9 ± 0.3	15.08 ± 0.01	0.68 ± 0.03
2016gtr	667.1 ± 1.4	15.61 ± 0.02	0.89 ± 0.12	670.8 ± 0.6	15.58 ± 0.02	0.69 ± 0.06
2016gxp	685.7 ± 0.6	15.10 ± 0.02	1.07 ± 0.07	688.5 ± 0.8	14.87 ± 0.02	0.61 ± 0.06
2016hli	696.3 ± 0.5	17.47 ± 0.03	1.58 ± 0.08	698.0 ± 0.7	16.82 ± 0.03	0.87 ± 0.06
2016hpw	703.4 ± 0.3	16.02 ± 0.02	1.04 ± 0.04	705.3 ± 0.3	15.97 ± 0.01	0.70 ± 0.03
2016hvl	710.9 ± 0.6	15.95 ± 0.04	1.17 ± 0.07	714.0 ± 0.9	15.49 ± 0.03	0.67 ± 0.05
2016huh	⋯	⋯	⋯	700.4 ± 1.0	16.86 ± 0.03	0.78 ± 0.09
2016igr	726.9 ± 0.4	15.31 ± 0.02	1.16 ± 0.05	728.1 ± 0.5	15.32 ± 0.02	0.69 ± 0.04
2016ins	724.1 ± 0.8	16.89 ± 0.03	1.50 ± 0.23	725.4 ± 0.9	16.58 ± 0.02	0.89 ± 0.09
2016ipf	728.0 ± 0.5	16.76 ± 0.02	1.35 ± 0.08	727.9 ± 1.2	16.74 ± 0.03	0.65 ± 0.08
2016jab	749.5 ± 0.8	16.06 ± 0.02	0.93 ± 0.08	751.5 ± 0.5	15.97 ± 0.02	0.64 ± 0.04
2017jl	784.9 ± 0.3	15.01 ± 0.02	0.99 ± 0.06	786.6 ± 0.4	14.94 ± 0.02	0.63 ± 0.06
2017yv	795.7 ± 0.6	15.74 ± 0.04	1.15 ± 0.09	797.2 ± 0.6	15.59 ± 0.04	0.72 ± 0.07
2017awk	808.4 ± 0.5	16.03 ± 0.02	1.22 ± 0.06	810.5 ± 0.6	15.79 ± 0.02	0.73 ± 0.05
2017azw	817.4 ± 0.5	14.99 ± 0.02	0.94 ± 0.07	817.7 ± 0.4	14.95 ± 0.02	0.65 ± 0.04
2017bkc	⋯	⋯	⋯	813.3 ± 1.0	16.66 ± 0.02	0.57 ± 0.08
2017cav	⋯	⋯	⋯	820.2 ± 1.6	16.32 ± 0.02	0.53 ± 0.09
2017cbr	834.7 ± 0.4	15.96 ± 0.02	1.31 ± 0.07	836.1 ± 0.6	15.78 ± 0.02	0.77 ± 0.06
2017cbv	840.8 ± 0.4	11.73 ± 0.02	0.97 ± 0.05	842.4 ± 0.6	11.68 ± 0.02	0.59 ± 0.04
2017cfd	844.1 ± 0.2	14.89 ± 0.02	1.18 ± 0.05	845.1 ± 0.3	14.77 ± 0.03	0.74 ± 0.05
2017ckq	851.6 ± 0.4	14.34 ± 0.01	1.16 ± 0.05	852.9 ± 0.4	14.35 ± 0.01	0.72 ± 0.03
2017cjr	846.9 ± 0.3	15.04 ± 0.02	1.22 ± 0.04	848.6 ± 0.4	15.08 ± 0.02	0.71 ± 0.04
2017cts	858.0 ± 0.5	15.79 ± 0.04	1.35 ± 0.06	859.4 ± 0.7	15.79 ± 0.02	0.73 ± 0.05
2017cze	⋯	⋯	⋯	859.0 ± 0.5	15.83 ± 0.02	1.02 ± 0.05
2017cyy	870.1 ± 0.4	14.84 ± 0.03	1.09 ± 0.07	871.4 ± 0.6	14.74 ± 0.03	0.60 ± 0.06
2017dei	868.7 ± 0.7	16.69 ± 0.03	1.71 ± 0.12	871.3 ± 0.6	16.43 ± 0.02	1.01 ± 0.07
2017dit	881.4 ± 0.3	15.90 ± 0.02	1.43 ± 0.07	883.4 ± 0.4	15.88 ± 0.02	0.79 ± 0.08
2017dps	882.4 ± 0.3	14.81 ± 0.03	1.64 ± 0.05	884.1 ± 0.5	14.81 ± 0.03	0.84 ± 0.05

Table 5
(Continued)

SN[a]	$t_{max}(B)$ −2,457,000	B_{peak} (mag)	$\Delta m_{15}(B)$ (mag)	$t_{max}(V)$ −2,457,000	V_{peak} (mag)	$\Delta m_{15}(V)$ (mag)
2017drh	891.5 ± 0.4	17.11 ± 0.03	1.33 ± 0.07	892.5 ± 0.4	15.76 ± 0.03	0.76 ± 0.05
2017egb	906.5 ± 0.3	15.72 ± 0.03	1.62 ± 0.07	907.8 ± 0.4	15.68 ± 0.01	0.84 ± 0.04
2017ejb	911.0 ± 0.1	15.83 ± 0.02	2.04 ± 0.04	913.2 ± 0.2	15.38 ± 0.01	1.30 ± 0.03
2017ejw	912.5 ± 0.3	15.51 ± 0.03	1.45 ± 0.06	913.7 ± 0.3	15.55 ± 0.03	0.86 ± 0.05
2017ekr	914.5 ± 1.6	16.15 ± 0.07	1.43 ± 0.40	915.9 ± 1.7	15.99 ± 0.06	0.95 ± 0.34
2017emq	917.5 ± 0.3	14.41 ± 0.02	1.36 ± 0.05	919.9 ± 0.5	14.17 ± 0.02	0.73 ± 0.05
2017enx	917.4 ± 1.4	14.05 ± 0.05	1.67 ± 0.19	920.1 ± 1.5	13.83 ± 0.05	0.93 ± 0.18
2017erv	923.8 ± 0.7	15.89 ± 0.02	1.04 ± 0.09	927.2 ± 0.5	15.67 ± 0.02	0.72 ± 0.04
2017erp	934.7 ± 1.7	13.69 ± 0.04	1.03 ± 0.21	936.7 ± 1.6	13.52 ± 0.03	0.65 ± 0.10
2017ezd	942.1 ± 0.4	15.79 ± 0.02	1.35 ± 0.07	942.5 ± 0.4	15.73 ± 0.02	0.78 ± 0.04
2017evn	936.1 ± 1.4	15.40 ± 0.05	1.02 ± 0.16	936.9 ± 1.1	15.34 ± 0.02	0.67 ± 0.09
2017exo	937.4 ± 0.8	16.70 ± 0.03	0.96 ± 0.09	938.8 ± 0.6	16.24 ± 0.03	0.69 ± 0.04
2017fbj	944.6 ± 0.5	16.22 ± 0.03	1.18 ± 0.09	947.6 ± 0.6	15.95 ± 0.04	0.71 ± 0.08
2017ffv	956.1 ± 1.2	15.49 ± 0.07	1.13 ± 0.14	957.7 ± 1.1	15.22 ± 0.04	0.73 ± 0.08
2017fgc	958.8 ± 0.2	13.76 ± 0.01	1.02 ± 0.03	963.1 ± 0.5	13.55 ± 0.01	0.72 ± 0.02
2017fzy	978.7 ± 0.9	16.32 ± 0.02	1.84 ± 0.14	983.2 ± 1.4	15.97 ± 0.02	1.08 ± 0.11
2017fzw	987.8 ± 0.2	14.21 ± 0.02	1.71 ± 0.03	990.1 ± 0.4	13.85 ± 0.02	0.88 ± 0.05
2017gah	984.9 ± 0.2	15.03 ± 0.03	1.72 ± 0.06	987.4 ± 0.3	14.57 ± 0.02	0.98 ± 0.05
2017gjn	1004.6 ± 0.3	15.14 ± 0.01	1.05 ± 0.03	1005.1 ± 0.4	15.06 ± 0.01	0.65 ± 0.03
2017glq	1016.2 ± 0.3	14.29 ± 0.01	1.23 ± 0.04	1016.8 ± 0.4	14.28 ± 0.01	0.68 ± 0.04
2017glx	1009.8 ± 0.6	14.69 ± 0.03	0.89 ± 0.07	1012.2 ± 0.7	14.53 ± 0.02	0.71 ± 0.04
2017grw	1017.5 ± 0.4	15.59 ± 0.02	1.51 ± 0.06	1019.0 ± 0.4	15.51 ± 0.02	0.80 ± 0.04
2017guh	1022.0 ± 0.6	15.20 ± 0.03	1.36 ± 0.12	1024.2 ± 0.5	15.18 ± 0.01	0.74 ± 0.04
2017haf	1034.8 ± 0.2	15.46 ± 0.01	1.19 ± 0.03	1035.8 ± 0.3	15.35 ± 0.01	0.75 ± 0.02
2017hgz	1044.3 ± 0.3	15.21 ± 0.01	1.46 ± 0.05	1046.1 ± 0.4	15.18 ± 0.02	0.77 ± 0.04
2017hjw	1056.0 ± 0.3	16.21 ± 0.02	0.97 ± 0.03	1057.0 ± 0.3	15.90 ± 0.01	0.63 ± 0.03
2017hjy	1056.2 ± 0.3	15.54 ± 0.02	1.21 ± 0.05	1057.7 ± 0.4	15.45 ± 0.01	0.66 ± 0.03
2017hle	1049.3 ± 0.5	17.93 ± 0.01	1.70 ± 0.07	1053.1 ± 0.2	16.99 ± 0.02	1.37 ± 0.03
2017hoq	1061.2 ± 1.3	16.03 ± 0.04	0.89 ± 0.12	1063.8 ± 0.6	15.95 ± 0.02	0.70 ± 0.04
2017hou	1056.5 ± 0.9	18.22 ± 0.02	0.94 ± 0.10	1057.5 ± 0.5	17.47 ± 0.02	0.64 ± 0.06
2017hpa	1065.8 ± 0.5	15.51 ± 0.02	1.05 ± 0.06	1068.7 ± 0.5	15.39 ± 0.01	0.72 ± 0.03
2017igf	1085.0 ± 0.2	14.87 ± 0.02	1.87 ± 0.05	1086.4 ± 0.2	14.59 ± 0.01	1.05 ± 0.03
2017iji	1081.7 ± 0.9	15.16 ± 0.02	1.26 ± 0.10	1084.0 ± 0.8	15.02 ± 0.02	0.74 ± 0.06
2017isj	1092.9 ± 1.3	15.81 ± 0.03	0.99 ± 0.16	1096.7 ± 0.5	15.59 ± 0.04	0.74 ± 0.05
2017iyb	1117.4 ± 0.6	14.91 ± 0.01	1.42 ± 0.08	1119.7 ± 0.4	14.82 ± 0.02	0.82 ± 0.04
2017iyw	…	…	…	1109.1 ± 1.2	15.62 ± 0.02	0.76 ± 0.08
2017jav	1118.1 ± 0.2	15.98 ± 0.03	1.81 ± 0.04	1119.3 ± 0.3	15.80 ± 0.01	0.96 ± 0.03
2017jdx	1119.0 ± 0.4	15.93 ± 0.02	1.07 ± 0.05	1120.1 ± 0.4	15.86 ± 0.01	0.60 ± 0.03
2018gl	1138.8 ± 0.1	16.31 ± 0.00	1.83 ± 0.02	1140.3 ± 0.1	16.14 ± 0.00	1.08 ± 0.01
2018gv	1149.6 ± 0.7	12.91 ± 0.03	0.84 ± 0.08	1151.1 ± 0.6	12.89 ± 0.02	0.62 ± 0.05
2018kp	1159.3 ± 0.3	16.62 ± 0.02	1.22 ± 0.05	1161.6 ± 0.4	16.09 ± 0.01	0.66 ± 0.03
2018pv	1163.9 ± 0.4	13.27 ± 0.03	1.85 ± 0.08	1166.8 ± 0.2	12.68 ± 0.03	1.18 ± 0.06
2018pc	1165.3 ± 0.4	15.42 ± 0.02	1.41 ± 0.08	1166.5 ± 0.4	15.08 ± 0.01	0.77 ± 0.04
2018oh	1163.2 ± 0.3	14.29 ± 0.01	0.99 ± 0.04	1163.8 ± 0.3	14.29 ± 0.01	0.65 ± 0.03
2018vw	1177.9 ± 0.5	15.37 ± 0.03	0.92 ± 0.07	1179.4 ± 0.6	15.44 ± 0.02	0.62 ± 0.04
2018xx	1183.9 ± 0.3	14.46 ± 0.02	1.37 ± 0.05	1185.1 ± 0.4	14.43 ± 0.02	0.79 ± 0.06
2018yu	1194.7 ± 0.4	13.98 ± 0.02	1.03 ± 0.06	1195.8 ± 0.4	13.94 ± 0.01	0.67 ± 0.04
2018zz	1190.7 ± 0.2	15.10 ± 0.02	1.91 ± 0.03	1192.4 ± 0.2	14.96 ± 0.01	1.03 ± 0.03
2018apo	1223.6 ± 0.7	15.50 ± 0.03	0.93 ± 0.09	1226.2 ± 0.7	15.26 ± 0.03	0.62 ± 0.08
2018aoz	1222.6 ± 0.3	12.84 ± 0.03	1.33 ± 0.07	1223.1 ± 0.3	12.84 ± 0.02	0.79 ± 0.04
2018aqi	1223.1 ± 0.3	15.81 ± 0.03	1.48 ± 0.06	1225.4 ± 0.3	15.58 ± 0.02	0.85 ± 0.04
2018aye	1243.9 ± 0.5	15.70 ± 0.02	1.04 ± 0.06	1244.7 ± 0.4	15.67 ± 0.02	0.71 ± 0.03
2018big	1264.5 ± 0.4	15.91 ± 0.01	0.98 ± 0.05	1266.1 ± 0.5	15.80 ± 0.01	0.60 ± 0.04
2018bta	…	…	…	1269.2 ± 0.7	15.47 ± 0.03	0.73 ± 0.08
2018cqw	1300.7 ± 0.4	14.56 ± 0.01	0.99 ± 0.05	1301.6 ± 0.4	14.45 ± 0.01	0.62 ± 0.03
2018ctv	1294.3 ± 0.6	17.42 ± 0.03	2.00 ± 0.07	1296.5 ± 0.7	16.70 ± 0.03	1.36 ± 0.06
2018cuh	1305.5 ± 0.4	15.02 ± 0.03	1.20 ± 0.08	1306.3 ± 0.3	15.03 ± 0.02	0.67 ± 0.05
2018dda	1313.7 ± 0.9	15.62 ± 0.04	0.98 ± 0.11	1315.6 ± 0.8	15.29 ± 0.03	0.67 ± 0.06
2018eay	1328.5 ± 0.5	17.48 ± 0.02	0.94 ± 0.07	1330.6 ± 0.8	16.69 ± 0.02	0.63 ± 0.05
2018ebk	1330.2 ± 0.4	16.88 ± 0.03	1.26 ± 0.05	1332.1 ± 0.4	16.32 ± 0.02	0.73 ± 0.03
2018enc	1345.5 ± 1.3	16.10 ± 0.04	0.89 ± 0.13	1346.5 ± 1.3	15.94 ± 0.03	0.66 ± 0.09
2018eov	1342.4 ± 0.9	15.65 ± 0.03	1.04 ± 0.12	1343.7 ± 0.6	15.42 ± 0.02	0.65 ± 0.05
2018eqq	…	…	…	1341.3 ± 1.0	15.30 ± 0.02	0.68 ± 0.05

Table 5
(Continued)

SN[a]	$t_{max}(B)$ −2,457,000	B_{peak} (mag)	$\Delta m_{15}(B)$ (mag)	$t_{max}(V)$ −2,457,000	V_{peak} (mag)	$\Delta m_{15}(V)$ (mag)
2018feb	1362.4 ± 0.3	15.26 ± 0.02	1.11 ± 0.05	1363.5 ± 0.4	15.24 ± 0.01	0.60 ± 0.03
2018fhw	1357.5 ± 0.2	16.67 ± 0.02	1.98 ± 0.04	1360.3 ± 0.3	16.37 ± 0.02	1.22 ± 0.04
2018fop	…	…	…	1366.7 ± 1.2	15.57 ± 0.03	0.55 ± 0.08
2018fnq	1374.6 ± 0.6	15.77 ± 0.03	1.06 ± 0.07	1375.0 ± 0.7	15.69 ± 0.02	0.65 ± 0.05
2018fuk	1377.1 ± 0.4	15.87 ± 0.01	1.20 ± 0.06	1378.9 ± 0.4	15.75 ± 0.02	0.68 ± 0.04
2018ghb	1381.0 ± 0.9	14.81 ± 0.05	1.59 ± 0.12	1384.4 ± 0.7	14.53 ± 0.03	0.97 ± 0.07
2018hib	1415.1 ± 0.3	15.25 ± 0.02	1.27 ± 0.05	1416.2 ± 0.4	15.22 ± 0.01	0.74 ± 0.03
2018htt	1438.6 ± 0.2	13.91 ± 0.03	1.59 ± 0.04	1439.5 ± 0.3	13.91 ± 0.03	0.85 ± 0.04
2018hrt	…	…	…	1433.8 ± 0.5	17.32 ± 0.02	0.82 ± 0.06
2018hsa	1432.3 ± 0.4	15.78 ± 0.02	1.14 ± 0.07	1434.6 ± 0.8	15.65 ± 0.02	0.69 ± 0.06
2018ilu	1449.7 ± 1.0	15.42 ± 0.02	0.93 ± 0.09	1451.9 ± 0.6	15.36 ± 0.01	0.62 ± 0.04
2018isq	1448.8 ± 0.4	16.89 ± 0.02	1.95 ± 0.08	1451.8 ± 0.2	16.00 ± 0.01	1.30 ± 0.04
2018iuu	1459.8 ± 0.3	15.48 ± 0.02	1.21 ± 0.04	1462.0 ± 0.7	15.46 ± 0.02	0.74 ± 0.04
2018jaj	1463.4 ± 0.4	15.52 ± 0.01	0.99 ± 0.04	1464.6 ± 0.4	15.41 ± 0.01	0.70 ± 0.03
2018jeo	1454.7 ± 1.0	16.07 ± 0.02	1.04 ± 0.11	1456.5 ± 0.5	15.94 ± 0.01	0.61 ± 0.05
2018jky	1469.0 ± 0.2	15.39 ± 0.03	1.69 ± 0.06	1470.2 ± 0.3	15.31 ± 0.02	0.89 ± 0.04
2018jmo	…	…	…	1475.7 ± 0.9	16.53 ± 0.04	0.91 ± 0.09
2018jov	1475.2 ± 0.4	16.21 ± 0.02	1.10 ± 0.05	1476.3 ± 0.5	16.06 ± 0.01	0.64 ± 0.04
2018jwi	1479.1 ± 0.3	15.04 ± 0.02	1.10 ± 0.04	1480.4 ± 0.4	15.04 ± 0.02	0.69 ± 0.04
2018kmu	1480.9 ± 1.4	16.42 ± 0.06	0.88 ± 0.18	1483.5 ± 1.8	16.30 ± 0.07	0.69 ± 0.12
2019np	1509.6 ± 0.5	13.42 ± 0.02	1.00 ± 0.05	1510.9 ± 0.7	13.39 ± 0.02	0.63 ± 0.04
2019so	1507.2 ± 0.2	17.21 ± 0.02	1.96 ± 0.04	1509.2 ± 0.2	16.67 ± 0.02	1.36 ± 0.04
PSN J140216.0-533228.8	1513.0 ± 0.9	17.01 ± 0.03	0.85 ± 0.10	1515.2 ± 0.8	16.26 ± 0.02	0.59 ± 0.06
2019gbx	1647.0 ± 0.3	14.80 ± 0.03	1.24 ± 0.06	1647.8 ± 0.4	14.78 ± 0.02	0.80 ± 0.04
2019hxc	1663.4 ± 0.9	16.60 ± 0.05	1.31 ± 0.15	1665.7 ± 1.5	16.44 ± 0.04	0.73 ± 0.08
2019khf	1680.3 ± 0.4	15.19 ± 0.03	1.12 ± 0.06	1681.8 ± 0.6	15.20 ± 0.03	0.63 ± 0.05
2020ue	1873.5 ± 0.2	12.22 ± 0.01	1.51 ± 0.04	1874.1 ± 0.3	12.16 ± 0.01	0.86 ± 0.03

Note.
[a] The SN name adopts the IAU name when available, otherwise the survey name. All the IAU and survey names are available in Table 1.

(This table is available in machine-readable form.)

parameters such as $\Delta m_{15}(B)$. We plan to publish near-UV, near-IR, and late-phase photometric data in the future. Our multiband light curves also allow us to derive host-galaxy extinction and luminosity, and in a forthcoming publication, we plan to make a completeness correction and study the SN Ia luminosity function. CNIa0.02 provides a large and homogeneous data set to infer the intrinsic distribution properties of SNe Ia in the local universe to help answer basic questions regarding SN Ia progenitor systems and explosion mechanisms.

We thank Eric Peng and the anonymous referee for helpful suggestions. We acknowledge the Telescope Access Program (TAP) funded by the NAOC, CAS and the Special Fund for Astronomy from the Ministry of Finance. We acknowledge SUPA2019A (PI: M.D. Stritzinger) via OPTICON. C.S.K., K. Z.S., and B.J.S. are supported by NSF grants AST-1515927, AST-1814440, and AST-1908570. M.D.S. acknowledges funding from the Villum Fonden (project numbers 13261 and 28021). M.D.S. is supported by a project grant (8021-00170B) from the Independent Research Fund Denmark. A.V.F.'s supernova group is grateful for financial assistance from the Christopher R. Redlich Fund, the TABASGO Foundation, and the Miller Institute for Basic Research in Science (U.C. Berkeley). A major upgrade of the Kast spectrograph on the Shane 3 m telescope at Lick Observatory was made possible through generous gifts from William and Marina Kast as well as the Heising-Simons Foundation. Research at Lick Observatory is partially supported by a generous gift from Google. We thank the staffs of the various observatories at which data were obtained for their excellent assistance. J.L.P. is provided in part by FONDECYT through the grant 1191038 and by the Ministry of Economy, Development, and Tourism's Millennium Science Initiative through grant IC120009, awarded to The Millennium Institute of Astrophysics, MAS. M.F. acknowledges the support of a Royal Society—Science Foundation Ireland University Research Fellowship. B.J.S. is also supported by NSF grants AST-1920392 and AST-1911074. M.G. is supported by the Polish NCN MAESTRO grant 2014/14/A/ST9/00121. Polish participation in SALT is funded by grant no. MNiSW DIR/WK/2016/07. S.M.H. is supported by the Natural Science Foundation of Shandong province (No. JQ201702), and the Young Scholars Program of Shandong University (No. 20820162003). Support for T.W.-S. H. was provided by NASA through the NASA Hubble Fellowship grant No. HST-HF2-51458.001-A awarded by the Space Telescope Science Institute, which is operated by the Association of Universities for Research in Astronomy, Inc., for NASA, under contract NAS5-26555. We thank the Swift PI Brad Cenko, the Observation Duty Scientists, and the science planners for approving and executing our Swift/UVOT SNe Ia campaign.

Software: Astropy (Astropy Collaboration et al. 2018), PyRAF (Science Software Branch at STScI 2012), FITSH (Pál 2012), ccdproc (Craig et al. 2017), HOTPANTS (Becker 2015), DoPHOT (Schechter et al. 1993; Alonso-García et al. 2012).

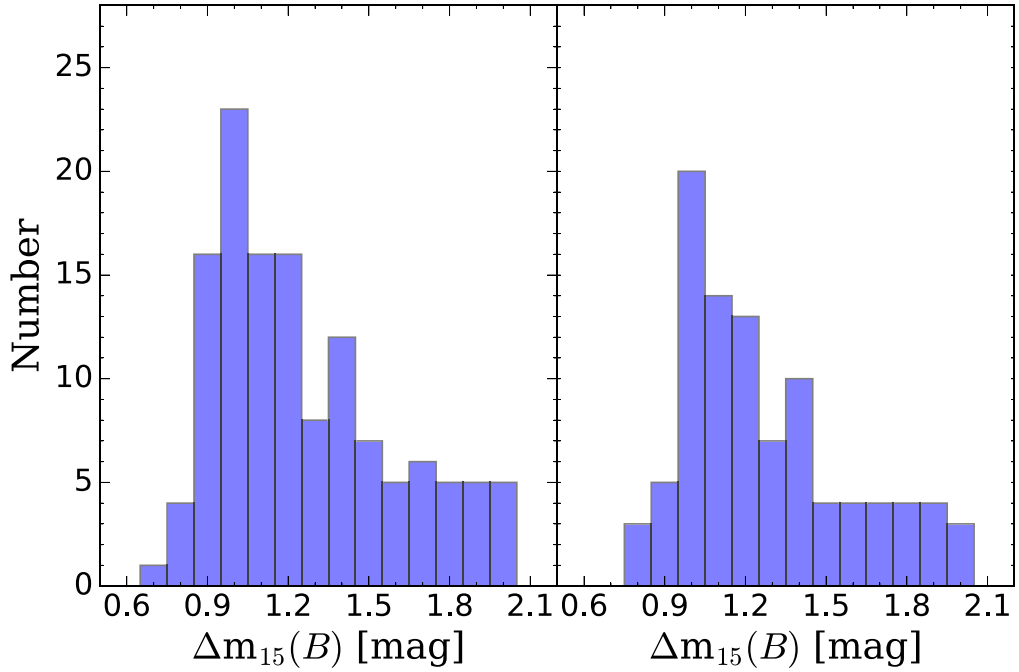

Figure 3. Distribution of all available direct $\Delta m_{15}(B)$ measurements for 129 SNe Ia in DR1 (left panel) and 95 SNe Ia in the complete sample (right panel).

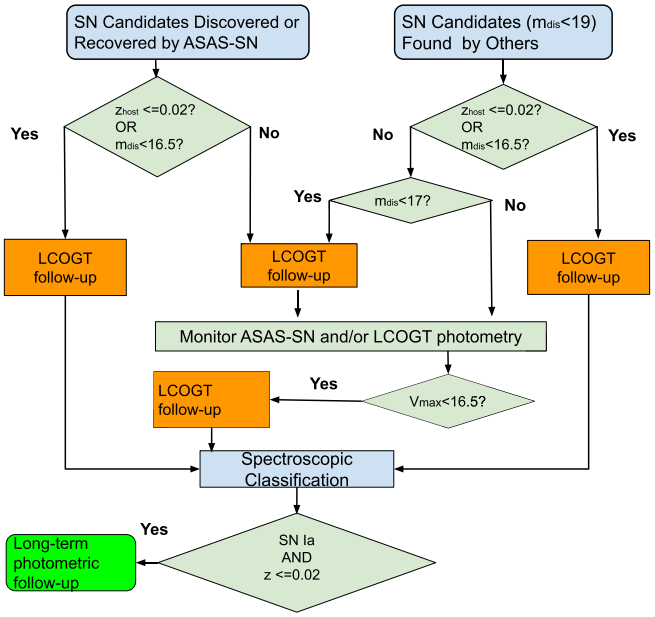

Figure 4. Observing protocol for the CNIa0.02 complete sample.

Appendix A
Observing Protocol

Figure 4 illustrates the protocol in our observing procedures when collecting our complete sample in the period between 2016 October and 2019 January. We scan the ASAS-SN transient page,[46] the Astronomer's Telegram,[47] the Transient Name Server,[48] and the Bright Supernova webpage[49] on a daily basis, and record all bright transients with discovery magnitudes of $m_{\rm dis} < 19$. To obtain early follow-up data for SNe Ia in the sample, we start observations before classification for all potential targets according to the strategy in Figure 4. Meanwhile, we coordinate all available spectroscopic resources to classify the potential targets. Note that the primary aim of our complete sample is to include all spectroscopic subclasses (e.g., 1991bg-like, 1991T-like) that belong to the SNe Ia population. We made follow-up observations of some SNe Ia-like objects (e.g., SNe Iax) that are known to deviate from the WLR of SNe Ia, and they do not belong to the complete sample. For SNe without archival host redshifts, we followed-up those with SN redshifts of $z_{\rm SN} \lesssim 0.025$ if they have $V_{\rm peak} < 16.5$. The selection of limit on $z_{\rm SN}$ is based on the knowledge that the typical uncertainties of SN redshifts from spectroscopic classification are $\lesssim$0.005. SuperNova IDentification (SNID; Blondin & Tonry 2007) is one of the commonly used tool for SNe classification. Stahl et al. (2020) investigated the SNID-determined redshifts by comparing them to the corresponding host-galaxy redshifts and found a standard deviation of 0.0039 for the difference between $z_{\rm SN}$ and $z_{\rm host}$.

Appendix B
Follow-up Instruments

We used 1 m telescopes from the Las Cumbres Observatory Global Telescope network (LCOGT; Brown et al. 2013), which operates a number of robotic telescopes distributed at four sites (Siding Spring in Australia, Sutherland in South Africa, Cerro Tololo in Chile, and McDonald Observatory in USA) covering both hemispheres. Each 1 m telescope is equipped with either a "Sinistro" or an SBIG STX-16803 camera.[50] The Bessel *BV* and SDSS *ri* filters are available on all telescopes, which were the main ones used for our optical observation. We also obtained some images using the 2 m or 0.4 m telescopes, and we plan to make these data available in the future.

[46] http://www.astronomy.ohio-state.edu/~assassin/transients.html
[47] http://www.astronomerstelegram.org/
[48] https://wis-tns.weizmann.ac.il/
[49] http://www.rochesterastronomy.org/snimages/
[50] https://lco.global/observatory/instruments/

Table 6
Instrument Specifications

Imager	Format (pixels)	Binning (pixels)	Pixel Scale (arcsec pixel^{-1})	Field of View (arcmin × arcmin)	Read Noise (e^-)	Gain (e^-/ADU)
SBIG STX-16803	4096 × 4096	2 × 2	0.464	15.8 × 15.8	13.5	1.5
Sinistro	4096 × 4096	1 × 1	0.389	26.5 × 26.5	7–8	1.0
Apogee Alta U230	2048 × 2048[a]	1 × 1	0.77	13.1 × 13.1	2.9	12.4
Apogee Alta U47	1024 × 1024	1 × 1	0.67	11.4 × 11.4	2.22	11.2
ANDICAM CCD	2048 × 2048	2 × 2	0.371	∼6 × 6	6.5	2.3

Note.
[a] The central 1024 × 1024 pixels were used.

We used two 24 inch CDK24 telescopes operated by the Post Observatory (PO) mainly for following-up northern objects. One is located at the Sierra Remote Observatories (SRO[51]; CA, USA) and the other at Post Observatory Mayhill (NM, USA). We used two types of cameras: an Apogee Alta U230 camera and an Apogee Alta U47 camera. Both cameras are back-illuminated, with similar quantum efficiency >90% over a broad region. The U230 camera was used by default at both sites. The telescope at SRO used the U230 for almost all images, and the Mayhill site had the U47 camera for a long period of time when the U230 camera was unavailable because its damaged shutter was being repaired. Astrodon Photometrics *BV*[52] and Sloan *ri*[53] filters were used.

The 1.3 m telescope of the Small and Moderate Aperture Research Telescope System (SMARTS; Subasavage et al. 2010) is located at Cerro Tololo Inter-American Observatory (CTIO). It is equipped with A Novel Dual Imaging CAMera (ANDICAM; DePoy et al. 2003). The optical CCD for ANDICAM is a Fairchild 447 2048 × 2048 pixel CCD. The IR Array for the ANDICAM is a Rockwell 1024x1024 HgCdTe "Hawaii" Array with 18 μm pixels. SMARTS/ANDICAM is equipped with standard KPNO-recipe Johnson-Kron-Cousins *BVRI* filters and standard CIT/CTIO *JHK* filters. SNe were observed in *BVRI* and *JH*-bands with ANDICAM. In this data release, we publish *BV* data. The *RI* and *JH* data taken by ANDICAM will be published in a future data release.

The instruments described above are the primary ones used for DR1. Their instrument specifications are listed in Table 6. The filter set used for observations in DR1 is compared to Landolt *BV* (Landolt 1992) and the SDSS *ri* (Fukugita et al. 1996) standard bandpasses in Figure 5.

DEdicated MONitor of EXotransits and Transients (DEMONEXT; Villanueva et al. 2018) is a 0.5 m PlaneWave CDK20 f/6.8 Corrected Dall-Kirkham Astrograph telescope at Winer Observatory in Sonoita, Arizona. DEMONEXT has a 2048 × 2048 pixel FLI Proline CCD3041 camera, with a 30′ × 30′ field of view (FOV) and a pixel scale of 0.″9 pixel^{-1}. DEMONEXT has a full suite of Bessel *BVRI* and SDSS *griz* filters. *BVri* data for four SNe (2016hli, 2016gou, 2016gxp, and 2017isq) are included in DR1. We also include photometry for three SNe (2017ghu, 2017hle, and 2018ast) obtained with the Liverpool Telescope (LT) IO:O instrument in DR1. IO:O is the optical-imaging component of the IO (Infrared-Optical) suite of instruments. It is equipped with a 4096 × 4112 pixel e2V CCD 231–84, with a 10′ × 10′ FoV and a pixel scale of ∼0.″3 pixel^{-1} with 2 × 2 binning. The 1 m telescope at WeiHai Observatory of Shandong University (WHO; Hu et al. 2014) was used to obtain *BVri* images for ASASSN-15uh. It has a back-illuminated PIXIS 2048B CCD camera at the Cassegrain focus, providing a 12′ × 12′ FoV and a pixel scale of 0.″35 pixel^{-1}. The 0.41 m f/3.3 reflector telescope at A77 observatory (Dauban, 04150 Banon, France) was used to obtain some *BV* images for 2015ar. The telescope is equipped with an ST8XME CCD, and its pixel scale is 1.″4 pixel^{-1}.

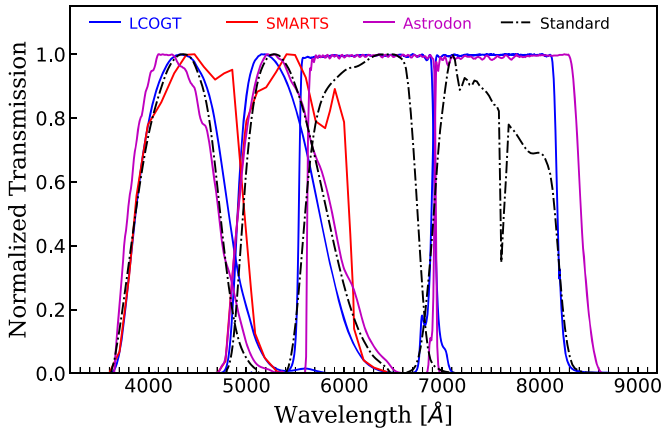

Figure 5. The filter bandpasses used to obtain the majority of data released in this paper (solid lines). The standard Landolt *BV* and SDSS *ri* bandpasses (dashed lines) are shown for comparison.

We used instruments mounted on the du Pont 2.5 m telescope, the 2.4 m Hiltner telescope and the 2.56 m Nordic Optical Telescope (NOT) to image a number of SNe. We used two cameras mounted on du Pont. One is called "CCD", which is a direct-imaging camera with a 2048 × 2048 pixel SITe2K CCD with plate scale of 0.″259 pixel^{-1} and an FoV of 8.′85 × 8.′85. The other is the WF4K CCD for the Wide Field Reimaging CCD Camera (WFCCD), which has a 4064 × 4064 pixel CCD with a plate scale of 0.″484 pixel^{-1} and an FoV of 25′ in diameter. For Hiltner, we used Ohio State Multi-Object Spectrograph (OSMOS), which is a wide-field imager and multi-object spectrograph. For our imaging observation, a 4096 × 4096 pixel STA0500A CCD was used, which has a scale of 0.″273 pixel^{-1} and an FoV with 20′ in diameter. On NOT, we used the Alhambra Faint Object Spectrograph and Camera (ALFOSC), which has both spectroscopic and imaging capabilities. The ALFOSC imaging was performed using a CCD231-42-g-F61 back-illuminated CCD with an FoV of 6.′4 × 6.′4 and a plate scale of 0.″2138 pixel^{-1} in the imaging mode.

[51] https://www.sierra-remote.com/
[52] https://astrodon.com/products/astrodon-photometrics-uvbri-filters/
[53] https://astrodon.com/products/astrodon-photometrics-sloan-filters/

Appendix C
Sample Completeness

Our targets are selected according to the detections of the ASAS-SN survey, so the sample completeness depends on the ASAS-SN detection efficiency, that is, the fraction of the occurred SNe that are detected by ASAS-SN. Holoien et al. (2019) compiled a sample of all SNe detected by ASAS-SN between 2014 May 01 and 2017 December 31, and they found that the integral completeness (i.e., the cumulative detection efficiency) of this total sample is $95 \pm 3\%$ at $m_{\rm peak} = 16.5$ by comparing with Euclidean predictions. That sample included SNe found before the implementation of a machine-learning algorithm at the end of 2014, which substantially increased the detection efficiency (see Figure 4 of Holoien et al. 2019). During the collection of our complete sample (i.e., 2015 September 17 to 2019 January 31), the ASAS-SN survey had several upgrades, including the operation of the Cassius unit in the summer of 2015 and the further expansions of three new units (Leavitt, Paczynski, and Payne-Gaposchkin) in late 2017, which increased the limiting magnitude from ∼17 to ∼18.5. Therefore, there are good reasons to believe that during our complete sample collection, the cumulative detection efficiency of ASAS-SN was at least 95%, and probably greater, at $m_{\rm peak} = 16.5$ mag.

We also conduct external checks with the concurrent detections by ZTF to verify our selection criteria. ZTF conducts a wide-field survey of the northern sky at a limiting magnitude of ∼20.5 (Kulkarni 2016), and the Bright Transient Survey (BTS) project of ZTF aims to construct a magnitude-limited complete sample of transients with spectroscopic classifications down to $m < 18.5$ (Fremling et al. 2020; Perley et al. 2020). The public start time of the BTS survey was 2018 June 1, so there were an overlapping period of 8 months (from 2018 June 01 to 2019 January 31) with our complete sample. We first check whether all SNe Ia with peak magnitudes bright than 16.5 in BTS are included in our complete sample. Using the ZTF Bright Transient Survey Sample Explorer[54], we queried all transients with a classification of "SN Ia" that peaked between 2018 June 01 and 2019 January 31 with peakmag < 16.5 and $z \leqslant 0.02$ and obtained a list of 14 objects. Among them, 2018dzy has a redshift $z_{\rm SN} = 0.02$ based on ZTF SN classification spectrum, while its host galaxy (UGC 11873) is at $z = 0.024760$ according to NED and was thus excluded from the CNIa0.02 complete sample. All others were included in CNIa0.02 and were followed-up by us. Our spectroscopic observations of the host galaxies show that four of them (2018fop, 2018htw, 2018jmo, and 2018kmu) have host-galaxy redshifts $z_{\rm host} > 0.02$. And all the other 9 SNe Ia (2018eay, 2018feb, 2018htt, 2018hkq, 2018iuu, 2018jaj, 2018jky, 2018jov, and 2019np) are included in the CNIa0.02 complete sample. In addition, we also queried all targets with a classification as "Candidate transients" with *peakmag* < 16.5 that were found between 2017 September 3 to 2019 December 31, and obtained 117 ZTF transients with peak magnitude brighter than 16.5. Among them, AT 2019ump (ZTF19acqnmjo) is likely a false positive (i.e., it has a high probability of being a "bogus" according to AleRCE ZTF Explorer[55]), and all the other 116 ZTF transient candidates were detected by ASAS-SN. Our cross-examinations support that our sample is ∼100% complete down to 16.5 mag.

[54] https://sites.astro.caltech.edu/ztf/bts/explorer.php
[55] https://alerce.online/object/ZTF19acqnmjo

Appendix D
Exclusion of Peculiar Ia-like Objects

The complete sample of CNIa0.02 includes all spectroscopic subclasses of SNe Ia that are known to follow the width-luminosity relation (WLR) of SNe Ia (see Phillips & Burns 2017 for a recent review of WLR). These include the luminous Ia-91T subclass and low-luminosity Ia-91bg subclass that are sometimes reported as "Ia-pec" in classification reports due to historical reasons, but recent studies firmly show that they follow the WLR (Phillips & Burns 2017; Burns et al. 2018), so they are included in our complete sample. During the collection of our complete sample, we analyze the spectra using SNID (Blondin & Tonry 2007) to screen peculiar SNe and also combine photometric properties when necessary to check whether an SN is truly peculiar according to our definition. Below we summarize peculiar SNe that are excluded from our complete sample.

ASASSN-15us was classified as SN Ia with the best match to SN 2006bt, which is shown to be a peculiar SN Ia (Foley et al. 2010). Moreover, the late-time spectra of ASASSN-15us show significant peculiarities compared to normal SNe Ia, and we plan to present the detailed analysis of this SN in the future.

ASASSN-15ut was first classified as SN Ia-91T (Firth et al. 2016), but a later classification based on new spectroscopic observation reported that this is a peculiar object, challenging to tell whether it is a peculiar Ia or Type-Ib/c SN (Milisavljevic et al. 2016). Holoien et al. (2017b) classified ASASSN-15ut as a Type-Ib/c SN. We measure the peak time in *i* and *B* band for ASASSN-15ut and obtain the time of *i*-band primary maximum relative to the *B* band of $t_{\rm max}^{i-B} \gtrsim 8$ days, which is outside the range for the SNe Ia population (Ashall et al. 2020).

ASASSN-15pz is an overly luminous SN belonging to the "2009dc-like SN Ia-pec" group (Chen et al. 2019). There is a large peak luminosity diversity within the group, and they generally do not follow the WLR.

2016gxp was reported to match premaximum spectra of SN 2007 well, as well as young 91T-like SN Ia (Reynolds et al. 2016). It lacks a secondary maximum in the *i*-band light curve and has $t_{\rm max}^{i-B} = 3.4 \pm 1.1$ days, which does not favor the 91T-like SN Ia classification (Ashall et al. 2020). We plan to present the detailed analysis of 2016gxp in the future.

2017gbb is a Type Iax (02cx-like) SN (Lyman et al. 2017), which does not belong to the SN Ia population.

ORCID iDs

Ping Chen https://orcid.org/0000-0003-0853-6427
Subo Dong https://orcid.org/0000-0002-1027-0990
C. S. Kochanek https://orcid.org/0000-0001-6017-2961
M. D. Stritzinger https://orcid.org/0000-0002-5571-1833
J. L. Prieto https://orcid.org/0000-0003-0943-0026
Juna A. Kollmeier https://orcid.org/0000-0001-9852-1610
N. Elias-Rosa https://orcid.org/0000-0002-1381-9125
Boaz Katz https://orcid.org/0000-0003-0584-2920
Lina Tomasella https://orcid.org/0000-0002-3697-2616
S. Bose https://orcid.org/0000-0003-3529-3854
Chris Ashall https://orcid.org/0000-0002-5221-7557
D. Bersier https://orcid.org/0000-0001-7485-3020
Thomas G. Brink https://orcid.org/0000-0001-5955-2502

P. Brown https://orcid.org/0000-0001-6272-5507
Enrico Cappellaro https://orcid.org/0000-0001-5008-8619
Morgan Fraser https://orcid.org/0000-0003-2191-1674
Mariusz Gromadzki https://orcid.org/0000-0002-1650-1518
Thomas W.-S. Holoien https://orcid.org/0000-0001-9206-3460
Shaoming Hu https://orcid.org/0000-0003-3217-7794
P. Lundqvist https://orcid.org/0000-0002-3664-8082
P. A. Milne https://orcid.org/0000-0002-0370-157X
Nidia Morrell https://orcid.org/0000-0003-2535-3091
J. A. Muñoz https://orcid.org/0000-0001-9833-2959
Robert Mutel https://orcid.org/0000-0003-1511-6279
A. Pastorello https://orcid.org/0000-0002-7259-4624
Simon Prentice https://orcid.org/0000-0003-0486-6242
B. J. Shappee https://orcid.org/0000-0003-4631-1149
Todd A. Thompson https://orcid.org/0000-0003-2377-9574
Steven Villanueva https://orcid.org/0000-0001-6213-8804
WeiKang Zheng https://orcid.org/0000-0002-2636-6508

References

Alonso-García, J., Mateo, M., Sen, B., et al. 2012, AJ, 143, 70
Ashall, C., Lu, J., Burns, C., et al. 2020, ApJL, 895, L3
Astropy Collaboration, Price-Whelan, A. M., Sipőcz, B. M., et al. 2018, AJ, 156, 123
Ashall, C., Mazzali, P., Sasdelli, M., & Prentice, S. J. 2016, MNRAS, 460, 3529
Becker, A. 2015, HOTPANTS: High Order Transform of PSF ANd Template Subtraction, Astrophysics Source Code Library, ascl:1504.004
Blondin, S., & Tonry, J. L. 2007, ApJ, 666, 1024
Branch, D., Chau Dang, L., & Baron, E. 2009, PASP, 121, 238
Branch, D., & Miller, D. L. 1993, ApJL, 405, L5
Breeveld, A. A., Curran, P. A., Hoversten, E. A., et al. 2010, MNRAS, 406, 1687
Breeveld, A. A., Landsman, W., Holland, S. T., et al. 2011, in AIP Conf. Proc. 1358, Gamma Ray Bursts 2010, ed. J. E. McEnery, J. L. Racusin, & N. Gehrels (Melville, NY: AIP), 373
Brown, P. J., Breeveld, A. A., Holland, S., Kuin, P., & Pritchard, T. 2014, Ap&SS, 354, 89
Brown, T. M., Baliber, N., Bianco, F. B., et al. 2013, PASP, 125, 1031
Bulla, M., Miller, A. A., Yao, Y., et al. 2020, ApJ, 902, 48
Burns, C. R., Parent, E., Phillips, M. M., et al. 2018, ApJ, 869, 56
Burns, C. R., Stritzinger, M., Phillips, M. M., et al. 2011, AJ, 141, 19
Burns, C. R., Stritzinger, M., Phillips, M. M., et al. 2014, ApJ, 789, 32
Chambers, K. C., Magnier, E. A., Metcalfe, N., et al. 2016, arXiv:1612.05560
Chen, P., Dong, S., Brimacombe, J., et al. 2018, ATel, 11762, 1
Chen, P., Dong, S., Katz, B., et al. 2019, ApJ, 880, 35
Contreras, C., Hamuy, M., Phillips, M. M., et al. 2010, AJ, 139, 519
Craig, M., Crawford, S., Seifert, M., et al. 2017, astropy/ccdproc: v1.3.0.post1, Zenodo, doi:10.5281/zenodo.1069648
DePoy, D. L., Atwood, B., Belville, S. R., et al. 2003, Proc. SPIE, 4841, 827
Dhawan, S., Leibundgut, B., Spyromilio, J., & Blondin, S. 2017, A&A, 602, A118
Dong, S., Katz, B., Kollmeier, J. A., et al. 2018, MNRAS, 479, L70
Drake, A. J., Djorgovski, S. G., Mahabal, A., et al. 2009, ApJ, 696, 870
Eweis, Y., Jha, S. W., Camacho, Y., et al. 2018, ATel, 11980, 1
Firth, R., Frohmaier, C., Dimitriadis, G., et al. 2016, ATel, 8495, 1
Flewelling, H. A., Magnier, E. A., Chambers, K. C., et al. 2020, ApJS, 251, 7
Foley, R. J., Narayan, G., Challis, P. J., et al. 2010, ApJ, 708, 1748
Foley, R. J., Scolnic, D., Rest, A., et al. 2018, MNRAS, 475, 193
Fremling, C., Miller, A. A., Sharma, Y., et al. 2020, ApJ, 895, 32
Fukugita, M., Ichikawa, T., Gunn, J. E., et al. 1996, AJ, 111, 1748
Ganeshalingam, M., Li, W., Filippenko, A. V., et al. 2010, ApJS, 190, 418
Gehrels, N., Chincarini, G., Giommi, P., et al. 2004, ApJ, 611, 1005
Gorbovskoy, E. S., Lipunov, V. M., Kornilov, V. G., et al. 2013, ARep, 57, 233
Hakobyan, A. A., Barkhudaryan, L. V., Karapetyan, A. G., et al. 2020, MNRAS, 499, 1424
Hamuy, M., Phillips, M. M., Suntzeff, N. B., et al. 1996, AJ, 112, 2391
Hicken, M., Challis, P., Jha, S., et al. 2009, ApJ, 700, 331
Hicken, M., Challis, P., Kirshner, R. P., et al. 2012, ApJS, 200, 12
Hodgkin, S. T., Harrison, D. L., Breedt, E., et al. 2021, A&A, 652, A76
Holoien, T. W. S., Brown, J. S., Stanek, K. Z., et al. 2017b, MNRAS, 467, 1098
Holoien, T. W. S., Brown, J. S., Stanek, K. Z., et al. 2017c, MNRAS, 471, 4966
Holoien, T. W. S., Brown, J. S., Vallely, P. J., et al. 2019, MNRAS, 484, 1899
Holoien, T. W. S., Stanek, K. Z., Kochanek, C. S., et al. 2017a, MNRAS, 464, 2672
Hu, S.-M., Han, S.-H., Guo, D.-F., & Du, J.-J. 2014, RAA, 14, 719
Huber, M., Carter Chambers, K., Flewelling, H., et al. 2015, IAU General Assembly, 29, 2258303
Jayasinghe, T., Kochanek, C. S., Stanek, K. Z., et al. 2018, MNRAS, 477, 3145
Jha, S., Kirshner, R. P., Challis, P., et al. 2006, AJ, 131, 527
Kochanek, C. S., Shappee, B. J., Stanek, K. Z., et al. 2017, PASP, 129, 104502
Krisciunas, K., Contreras, C., Burns, C. R., et al. 2017, AJ, 154, 211
Kulkarni, S. R. 2016, AAS Meeting, 227, 314.01
Landolt, A. U. 1992, AJ, 104, 340
Law, N. M., Kulkarni, S. R., Dekany, R. G., et al. 2009, PASP, 121, 1395
Leaman, J., Li, W., Chornock, R., & Filippenko, A. V. 2011, MNRAS, 412, 1419
Li, W., Chornock, R., Leaman, J., et al. 2011a, MNRAS, 412, 1473
Li, W., Leaman, J., Chornock, R., et al. 2011b, MNRAS, 412, 1441
Lochner, M., McEwen, J. D., Peiris, H. V., Lahav, O., & Winter, M. K. 2016, ApJS, 225, 31
Lyman, J., Homan, D., Leloudas, G., & Yaron, O. 2017, Transient Name Server Classification Report, 2017-893, 1
Maoz, D., Mannucci, F., & Nelemans, G. 2014, ARA&A, 52, 107
Milisavljevic, D., Parrent, J., Patnaude, D., Kamble, A., & Margutti, R. 2016, ATel, 8497, 1
Milne, P. A., Brown, P. J., Roming, P. W. A., Bufano, F., & Gehrels, N. 2013, ApJ, 779, 23
Moral-Pombo, D., Panizo-Espinar, G., Sanchez-Sierras, J., et al. 2018, ATel, 12313, 1
Nugent, P., Phillips, M., Baron, E., Branch, D., & Hauschildt, P. 1995, ApJL, 455, L147
Pál, A. 2012, MNRAS, 421, 1825
Perley, D. A., Fremling, C., Sollerman, J., et al. 2020, ApJ, 904, 35
Phillips, M. M. 1993, ApJL, 413, L105
Phillips, M. M. 2012, PASA, 29, 434
Phillips, M. M., & Burns, C. R. 2017, in Handbook of Supernovae, ed. A. W. Alsabti & P. Murdin (Cham: Springer), 2543
Phillips, M. M., Lira, P., Suntzeff, N. B., et al. 1999, AJ, 118, 1766
Poole, T. S., Breeveld, A. A., Page, M. J., et al. 2008, MNRAS, 383, 627
Reynolds, T., Dong, S., Fraser, M., et al. 2016, ATel, 9645, 1
Riess, A. G., Kirshner, R. P., Schmidt, B. P., et al. 1999, AJ, 117, 707
Roming, P. W. A., Kennedy, T. E., Mason, K. O., et al. 2005, SSRv, 120, 95
Schechter, P. L., Mateo, M., & Saha, A. 1993, PASP, 105, 1342
Schlafly, E. F., & Finkbeiner, D. P. 2011, ApJ, 737, 103
Schmidt, M. 1968, ApJ, 151, 393
Science Software Branch at STScI 2012, PyRAF: Python Alternative for IRAF, Astrophysics Source Code Library, ascl:1207.011
Shappee, B. J., Prieto, J. L., Grupe, D., et al. 2014, ApJ, 788, 48
Stahl, B. E., Zheng, W., de Jaeger, T., et al. 2019, MNRAS, 490, 3882
Stahl, B. E., Zheng, W., de Jaeger, T., et al. 2020, MNRAS, 492, 4325
Stritzinger, M. D., Phillips, M. M., Boldt, L. N., et al. 2011, AJ, 142, 156
Stritzinger, M. D., Shappee, B. J., Piro, A. L., et al. 2018, ApJL, 864, L35
Struble, M. F., & Rood, H. J. 1999, ApJS, 125, 35
Subasavage, J. P., Bailyn, C. D., Smith, R. C., et al. 2010, Proc. SPIE, 7737, 77371C
Tonry, J. L. 2011, PASP, 123, 58
Tonry, J. L., Denneau, L., Flewelling, H., et al. 2018b, ApJ, 867, 105
Tonry, J. L., Denneau, L., Heinze, A. N., et al. 2018a, PASP, 130, 064505
Tonry, J. L., Stubbs, C. W., Lykke, K. R., et al. 2012, ApJ, 750, 99
van Dokkum, P. G. 2001, PASP, 113, 1420
Villanueva, S. J., Gaudi, B. S., Pogge, R. W., et al. 2018, PASP, 130, 015001
Wyrzykowski, Ł., Kostrzewa-Rutkowska, Z., Kozłowski, S., et al. 2014, AcA, 64, 197